UNIVERSITY OF CALIFORNIA
RIVERSIDE

Low-Cost Strategies for Accurate Free Energy Prediction of Organic Molecular Crystals

A Dissertation submitted in partial satisfaction
of the requirements for the degree of

Doctor of Philosophy

in

Chemistry

by

Cameron J. Cook

December 2022

Dissertation Committee:

Dr. Gregory Beran, Chairperson
Dr. Christopher Bardeen
Dr. Chia-en Chang

The Dissertation of Cameron J. Cook is approved:

Committee Chairperson

University of California, Riverside

Acknowledgments

I would like to thank my advisor Greg Beran for his constant support and guidance throughout my PhD. He provided the academic freedom and mentorship necessary for me to learn and explore the world of computational crystal structure prediction. I would like to thank my lab mates Joshua Thompson, Cody Perry, Dr. Jessica McKinley, Dr. Watit Sontising, and Dr. Dominique Nocito; our positive group environment both in and out of the lab made graduate school an incredible experience. I would like to give special thanks to my dear friends and colleagues Dr. Pablo Unzueta, Dr. Chandler Greenwell, and Dr. Brandon Lui. Each one of our lunches and happy hour outings made life in lab a little easier. Finally, I'd like to thank my friends and family for their limitless support, love, and patience as I pursued my studies. Mom, Dad, and Drew – you were always there for me even when I couldn't return the favor. Jack and Sam, our Saturday Dungeons and Dragons sessions spanning the better part of these past four years made the weekend something to look forward to. Brad, our backpacking trips provided that mental "reset" when things just got a little too difficult. Brandon, our football Sundays are second to none even though the Broncos can't seem to get it right. And Delaney, my loving fiancé, without you none of this would have been possible. I'm beyond excited to see what's next for us.

To Craig Cook, Maureen Cook, Andrew Cook, and Delaney Sipprelle.

ABSTRACT OF THE DISSERTATION

Low-Cost Strategies for Accurate Free Energy Prediction of Organic Molecular Crystals

by

Cameron J. Cook

Doctor of Philosophy, Graduate Program in Chemistry
University of California, Riverside, December 2022
Dr. Gregory Beran, Chairperson

Consistent, accurate *in silico* characterization of organic molecular crystals would greatly benefit the discovery of new materials. This thesis presents several strategies that have been developed for assessment of thermodynamic stability, quantifying finite temperature effects, and prediction of mechanical properties for organic molecular crystals.

Finite temperature contributions to crystal stability are approximated using hybrid semi-empirical and first principles density functional theory for lattice dynamics. This model approximates the phonon density of states using a composite density functional tight binding (DFTB) and density functional theory (DFT). This composite method is applied to oxalyl dihydrazide (ODH) polymorphs and is able to correctly rank the five crystals in relative thermodynamic stability. Absolute values of the thermodynamic state functions are predicted within 1 kJ/mol of their pure DFT values. The combined DFT/DFTB phonon densities of state (pDOS) result in similar accuracy compared to conventional DFT but require far less computational effort.

The thermal expansion of resorcinol, naphthalene, BTBT, and pentacene are also predicted using the DFT/DFTB pDOS along with the quasiharmonic approximation (QHA). The solid state phase diagram for the polymorphic α- and β-resorcinol forms was evaluated, with a predicted transition temperature of 368 K at ambient pressure, in excellent agreement with the literature.

Finally, crystal structure prediction (CSP) was performed for 9-methyl anthracene (9MA), a photomechanical crystal. These crystals undergo a photochemical reaction in the solid state, causing abrupt changes in crystal structure ultimately converting light energy to mechanical work. CSP was used to identify potential polymorphs of the reactant and product 9MA as well as their energetic relationships. The predicted product crystals were verified experimentally. Theoretical work densities for 9MA, 9-*tert*-butyl anthracene ester, and 9-carboxylic acid anthracene were also predicted to be on the order of $\sim 10^7$ J/m^3, making these types of systems incredibly promising for photoactuators.

Contents

List of Figures

List of Tables

Chapter 1

Introduction

Molecules in crystalline form can arrange in a variety of different ways, an effect known as polymorphism. Polymorphism in organic molecular crystals has proven to be a significant factor in the systematic, rational design of these materials. Desired properties in several applications, whether it be solubility for pharmaceuticals, mobility of charge carriers for semiconductors, or π-stacking motifs for photoactuators, depend intrinsically on the packing pattern of the constituent molecules. While in some cases polymorphism is viewed as an obstacle in crystal engineering, it can also be exploited to tune the properties of a material.

Polymorphism has impacted the pharmaceutical industry for decades; a crucial step in drug development involves the experimental screening of polymorphs, a process that can be time-intensive and hard to perform exhaustively. Perhaps the most infamous (and expensive) consequence of undetected polymorphism was the case of ritonavir. It was found that the form crystallized in the lab initially (Form I) was thermodynamically

meta-stable, causing an eventual transition into its "true" most stable polymorph (Form II) after it had been released. This new form had much lower solubility which hindered bioavailability. Form II, being much more stable, rapidly became the only form isolated during manufacturing. This ultimately led to a year-long recall of the drug before kinetic control was established to ensure no Form II was present. This cost the manufacturers an estimated $250 million in lost sales.[15,16] Even more: a study conducted by van de Streek and Neumann predicts that an additional 15 to 45% of current small molecule drugs on the market still exist in a meta-stable form rather than their true energetic minimum.[17]

Issues such as these fueled the desire to develop methods for systematically determining a molecule's crystal structure that could complement experimental polymorph screening. These efforts can be expensive, and an exhaustive screen is difficult to guarantee. A purely computational approach could aid in molecular crystal design, but would have to be conducted with little to no crystallographic information available initially. If a reliable physical model were attainable that could predict how constituent molecules arrange in the crystal, using nothing but the molecular structure, it could help anticipate problematic forms or, conversely, provide a road map to targeting other forms with more desirable properties. The development and application of such crystal structure prediction models for computational screening of polymorphs using atomistic simulations has become a boon for crystal engineering.

Crystal structure prediction (CSP) has matured in applications to several areas of research. CSP was used to identify novel low-density organic molecular crystals for gas storage,[18] and it has shown promise in identifying high-mobility organic semiconducting

crystals.[19,20] It has also been used for insightful polymorph screening in the drug galunisertib, a treatment of metastatic malignancies.[21] The drug has ten known experimental polymorphs, each of which was identified using CSP, as well as additional predicted low energy forms yet to be isolated experimentally.[22]

A priori determination of crystal polymorphism using chemical intuition alone is unlikely, and a complete characterization of all potential forms a molecule can pack in is intractable. Modern CSP approaches operate in this gap, where we ask ourselves: Given some fraction of the possible arrangements in a crystal this molecule can adopt, what is the likelihood that several are viable?

With the considerable increase of computational power over the last decade, this problem became more tractable and, by some accounts, essentially solved.[23,24] Where we were until recently limited to small, conformationally simple organic molecules, we can now often predict crystal structures of more complicated and chemically interesting molecules with relative confidence, albeit with significant computational effort.

An ideal CSP approach aims to predict the most stable polymorph out of all possible forms given only a chemical diagram of its constituent molecules. Schematically one would:

1. Choose a molecular geometry

2. Generate a crystallographic unit cell

3. Evaluate the free energy, G

Performing these three steps in their entirety (i.e. predicting *all* potential configurations and their free energies) yields the complete crystal landscape. The lowest energy

configuration is taken to be the thermodynamic minimum, and higher energy forms are meta-stable polymorphs. While conceptually straightforward, evaluation of the free energy G for all potential configurations is difficult. Accurate evaluation of free energy for a single configuration can be computationally demanding, molecular flexibility adds an exponential complexity to the configuration space.

This thesis aims to clearly define these problems and to introduce alternative methods for free energy determination as well as perform additional applications for molecular crystal structure prediction. These methods are then applied in later chapters to address thermal expansion in small organic molecular crystals, quantify expansion-dependent charge carrier mobility parameters in organic semiconducting crystals, and determining mechanical properties of solid-solid photochemical reactions using CSP.

1.1 Crystal Structure Prediction: Current Applications and Limitations

1.1.1 Free Energy Prediction

Even with the increases in algorithm efficiency and computational power, a fully robust CSP approach remains elusive; the most successful applications require a balance between accuracy and computational cost. A valuable benchmark for these approaches, as well as an overview for the evolution of CSP over a span of 15 years, is outlined in the various organic crystal structure prediction blind tests arranged by the Cambridge Crystallographic Data Center (CCDC).[25–30] A seventh blind test has also recently concluded and a formal report is pending. These arranged blind tests offer significant insight on how participants

in the field are approaching CSP, what strategies are successful, and where some strategies falter. Generally a CSP problem can be broken down into two equally important parts: searching the vast potential energy landscape for likely forms, and computing the energetic rankings of the predicted forms. A thorough structure search is necessary for providing candidates to the final ranking, and accurate rankings are imperative for predicting potential experimental polymorphs. This thesis focuses primarily on providing additional tools for energy ranking.

Where the initial searching procedure has become increasingly elegant, final energetic ranking of potential forms has largely been limited to progress in predicting zero temperature electronic energies. This is due to the difficulty of including accurate thermodynamic contributions to a crystal's free energy. A molecular crystal is in its thermodynamic ground state when its Gibbs free energy is minimized with respect to all atomic positions and crystallographic unit cell parameters:

$$G(T, P, V) = U_{el} + F_{vib}(T) + PV \tag{1.1}$$

where U_{el} is the electronic energy, $F_{vib}(T)$ is the Helmholtz vibrational free energy, and PV are pressure-volume contributions. An ideal workflow for the evaluation of Equation 1.1 can be found in Figure 1.1. Typical quantum chemical algorithms perform this minimization by solving for the electronic energy U_{el} at 0 K and moving the atomic positions until the energy reaches a local minimum on a high-dimensional potential energy surface. Crystal polymorphism is a manifestation of the large amount of local minima on the free energy surface.

$$G(\boldsymbol{x}) \approx U_{el}(\boldsymbol{x}) \tag{1.2}$$

$$U_{el}(\boldsymbol{x}) = U_{el}(\boldsymbol{x_0}) + g_0^T \Delta \boldsymbol{x} + \frac{1}{2} \Delta \boldsymbol{x}^T \boldsymbol{H_0} \Delta \boldsymbol{x} \tag{1.3}$$

Most modern CSP approaches frequently exploit the approximation presented in Equation 1.2, where $\boldsymbol{x}$ is a set of atomic positions. This allows for a relatively straightforward structure optimization to approximate the free energy, shown in Equation 1.3, where $\boldsymbol{g_0}^T$ and $\boldsymbol{H_0}$ are the gradient and Hessian, respectively.[31] The approximation can sometimes hold because $F_{vib}(T)$ and PV provide only a small percentage of the total energy at ambient pressure and temperature conditions, equating to only a few kJ/mol. Additionally, polymorph ranking is assigned by taking the relative energy between two forms where enthalpic and entropic contributions can effectively cancel out. However it is also true that polymorphs of a given crystal often differ by only a few kJ/mol, implying the potential necessity for finite temperature contributions introduced by $F_{vib}(T)$. This was shown to be the case in a study by Nyman and Day in 2015 where the energetics of 508 polymorphic organic molecular crystals were thoroughly studied.[32] It was found that 95% of these polymorphs had relative 0K lattice energies (U_{el}) within 7.2 kJ/mol of one another. Further, 9% of these polymorphs were found to re-order at room temperature after the inclusion of finite temperature effects. This implies that an approximation of Gibbs free energy using only the electronic lattice energies of the crystal, as is commonplace for CSP, yields the incorrect minimum energy structure at typical experimental conditions nearly one tenth of the time.

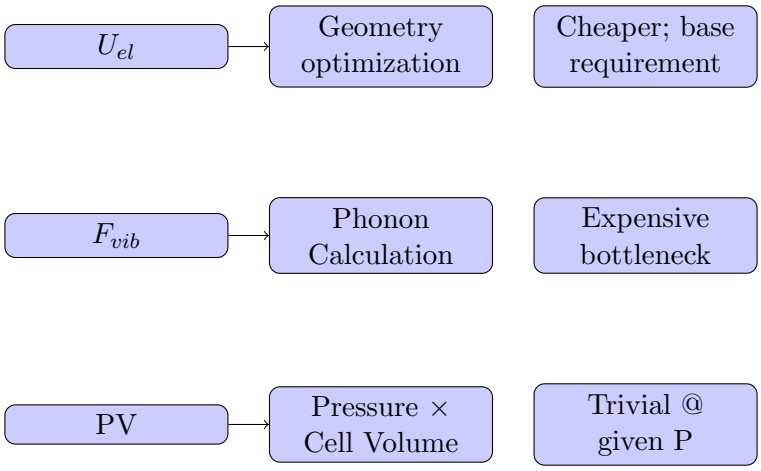

Figure 1.1: Schematic outline of the requirements for crystal free energy assignment.

With this information it can be difficult to understand why polymorph ranking in CSP has essentially remained a lattice energy minimization procedure rather than fully implementing finite temperature effects. This has a particularly simple explanation: The computational cost of including thermodynamic effects at real temperatures is prohibitively expensive for the high-throughput nature of crystal structure prediction. Practical evaluation of $F_{vib}(T)$ requires lattice dynamics, which are considerably more costly than the baseline crystal potential. To this end, we offer a low-cost method for evaluating the phonon density of states (pDOS) necessary for these calculations. The method, as well as further details regarding pDOS calculations for molecular crystals, are presented Sections 2.1 and 2.2. Additional applications of this method are introduced in Sections 2.3 - 2.4.

1.1.2 Applying CSP to Photomechanical Materials

The recent maturity of CSP also introduces potential for application to fields of chemistry outside of pharmaceuticals. One field of particular interest is that of smart materials, where molecular crystals are becoming increasingly prevalent.[33–36] These mate-

rials undergo physical changes when exposed to external stimuli such as heat, light, force, or chemical environment, and experience a wide variety of movement including twisting, bending, walking, etc. They have shown promise for applications in actuators, molecular machines, optical sensors, and smart switches.[37–39] Smart materials derived from molecular crystals, as opposed to polymers or elastomers, offer a unique advantage due to the well-defined crystal structure and large elastic moduli. Smart materials that use light to react constituent organic molecules in crystals, or simply "photomechanical crystals", will be the primary focus in this work.

Photomechanical crystals are of particular interest because of their unique ability to directly convert light energy to mechanical work. While the behavior of these crystals after interacting with light is well studied, a detailed understanding of the underlying structural transformations is lacking. This is largely a result of technical hurdles for experimental characterization techniques; crystal-to-crystal reactions in photomechanical systems yielding a large enough product for single crystal analysis often accumulate internal strain as the reaction progresses, fracturing the material.[40,41] While chemical theory literature does exist for these systems, it is largely focused on the energetics of the photochemical reaction itself or serves as a supplement for experimental techniques when determining crystal structure.[42–44] A CSP-based approach using molecular information alone to glean crystallographic details from the photomechanical process could aid in further device design.

CSP provides an avenue for *in silico* design that would be invaluable to crystal engineering for photomechanical systems. This thesis introduces, to our knowledge, the first example of CSP applied to photomechanical systems. Accurate CSP for photomechanical

crystals could quickly identify potential product crystals for the photochemical reaction as well as characterize the mechanical evolution of the reactant crystal. A detailed outline of the CSP procedure used for the study of photomechanical crystals is found in Section 2.5 and 2.6, and the concepts behind the photochemical reaction and the benefits of predictive atomistic modelling of photomechanical crystals are outlined in 2.7.

1.2 Outline of the Dissertation

The remainder of this thesis introduces several tools developed for easing the computational load of organic molecular crystal structure prediction. Later chapters demonstrate some successful applications of these tools for several physical quantities including thermal expansion, highly accurate polymorph ranking, charge carrier mobility parameters, and photomechanical crystal work output. Chapter 2 serves as a brief technical outline for these methods as well as the computational details for the electronic structure calculations used throughout.

Normal mode eigenvector matching, referred to simply as "mode-matching" is a method used for cheaper phonon densities of state which is a crucial component in evaluating free energy at real temperatures. Mode-matching introduces a way for up-scaling cheap phonon densities of states to closely match those of explicit evaluation with higher levels of theory, resulting in cost savings of an order of magnitude with little additional error. This is outlined in some detail in section 2.1, and further in Chapter 3. Thermodynamic properties of small organic molecular crystals can be accurately reproduced using this method compared to explicit evaluation with density functional theory.

More efficient evaluation of the pDOS allowed us to look at thermodynamic properties of organic molecular crystals more readily. Using mode-matching, we predicted the thermodynamic properties of α- and β-resorcinol as a function of temperature. Coupling mode-matching with the quasiharmonic approximation (detailed in section 2.3) results in an affordable approach to predicting expensive thermodynamic quantities like thermal expansion and solid-state phase diagrams. Quantitative accuracy for temperature dependent unit cell parameters and phase transitions for the two polymorphs was achieved, demonstrated further in Chapter 4.

Chapter 5 contains the application of the methods mentioned above to predict thermal expansion in organic semiconducting crystals (OSCs). Carrier mobility in OSCs is an important qualifier for device viability, which the intermolecular transfer integral is a parameter for. This investigation determined that coupling mode-matching with thermal expansion via the quasiharmonic approximation is sufficient for crystals outside of pharmaceuticals, where intermolecular interactions like hydrogen bonding are less prevalent. Charge transfer integrals at thermally expanded geometries were then computed, providing an important parameter for carrier mobility as a function of temperature.

Finally, crystal structure prediction was used for the first time to solve for photomechanical product crystal structures *in silico.* 9-methylanthracene undergoes a photochemical [4+4] reaction when excited at 370 nm, abruptly dimerizing cofacial monomer pairs and generating internal strain in single crystals. This causes the crystals to abruptly fracture, making characterization of the solid state reacted dimer (SSRD) difficult. Chapter 6 uses CSP to identify this form as well as others on the crystal energy landscape. A topochem-

ical reaction algorithm forming the SSRD from the monomer crystal is also introduced. Lattice deformations from the reactant crystal to the product are used to determine the magnitude of anisotropic work, a useful parameter in designing functional photoswitches. This approach was also used for two additional anthracene derivatives, 9-carboxylic acid antrhacene and 9-*tert*-butyl anthracene ester.

Chapter 2

Technical Concepts and Computational Details

This chapter serves as a technical overview for the methods developed and applied in later chapters. Sections 2.1 - 2.3 introduce strategies for inclusion of finite temperature effects in polymorph free energy ranking. Section 2.4 outlines the technique used for determining intermolecular charge transfer integrals used in predicting carrier mobility in organic semiconducting crystals. Finally, sections 2.5 - 2.7 introduce a crystal structure prediction procedure for photomechanical crystals and the quantification of potential work output following the photochemical reaction. Computational details for electronic structure calculations are found in section 2.8.

2.1 Lattice Dynamics

Neglect of the $F_{vib}(T)$ term from Equation 1.1, while often an acceptable approximation, is also attributed to the computational complexity of its determination. Introducing vibrational free energy into the Gibbs free energy expression in the requires information on the vibrational density of states. Vibrational calculations within the harmonic approximation involve atomic displacements and the evaluation of resulting forces forming the Hessian matrix, whose size grows as $3N$, where N is the number of atoms, for gas-phase calculations. This issue is further exacerbated in the solid state where atomic displacements of the atoms exert forces on neighboring molecules, and the center of mass translation of the molecules themselves enact forces on neighbors creating "soft modes". In the solid state, F_{vib} can be derived from statistical mechanics:

$$F_{vib}(T) = 3nN_A k_B T \int_0^\infty \ln\left[2\sinh\left(\frac{\hbar\omega}{2k_B T}\right)\right] g(\omega) d\omega \tag{2.1}$$

where n is the number of atoms in the unit cell, N_A is Avogadro's number, $g(\omega)$ is the phonon density of states (pDOS) as a function of frequency ω, $\hbar$ is Planck's constant, k_B is the Boltzman constant, and T is temperature.[45]

Within the harmonic approximation, the crystal potential can be approximated via the second term of the Taylor expansion of overall potential with respect to atomic displacements,

$$U = U_0 + \sum_{l,\alpha} U_\alpha^l u_\alpha^l + \frac{1}{2}\sum_{l,l',\alpha,\beta} U_{\alpha\beta}^{ll'} u_\alpha^l u_\beta^{l'} + \cdots \tag{2.2}$$

$$U_{\alpha\beta}^{ll'} = \frac{\partial^2 U}{\partial u_\alpha^l \partial u_\beta^{l'}} \tag{2.3}$$

where U is crystal potential and u_α^l is the displacement of atom l in direction α. U_α^l represents the nuclear gradient of the potential with respect to the displacement of atom l, which equals zero when the structure has been optimized to a stationary point. $U_{\alpha\beta}^{ll'}$ is the matrix of force constants describing the forces felt by atom l in the central unit cell after the displacement of atom l'. Mass weighting and transforming the coordinates into reciprocal space yields the dynamical matrix $D_{\alpha\beta}$, which can be diagonalized according to:

$$\omega^2 u_\alpha = \sum_\beta D_{\alpha\beta} u_\beta \quad \text{where} \quad D_{\alpha\beta} = \frac{1}{\sqrt{m_l m_{l'}}} \sum_n U_{\alpha,\beta}^{l,l'} \exp(-i\mathbf{k} \cdot \mathbf{r}_n) \tag{2.4}$$

This dynamical matrix equation relates atomic displacement, force response, and resulting vibrational frequencies ω. The normal mode eigenvectors u_α are normalized vectors describing the collective movement of the atoms that result in the frequency of that mode.

Constructing the dynamical matrix for a molecular crystal involves $3N$ individual atomic displacements (which can often be reduced by symmetry) and $3N * M$ force evaluations, where M is the number of points needed to fit the harmonic potential. Further, in order to capture long-range forces, one must look beyond the unit cell and consider the effects of displacement on periodic images. This method, often referred to as the "supercell method", results in potentially several hundred force calculations for a single pDOS.

Here, a new method is introduced for evaluating the converged pDOS without the need for the most computationally expensive quantum chemical calculations on the expanded supercell. This involves evaluating Equation 2.4 with a reference quantum chemical

method i.e. plane wave density functional theory, at $k = 0$, and evaluating the full supercell with a cheaper method, i.e. density functional tight binding (DFTB). Both strategies will be outlined in greater detail in Section 2.8. These will produce frequency eigenvalues and normalized eigenvectors for each method at the Γ-point (where $k = 0$). The normal mode Γ-point eigenvectors represent the movement of the atoms resulting in the corresponding normal vibration ω. These vectors can be mapped onto one another, and their associated frequencies can be shifted, such that the full pDOS of the "cheap" method can be upscaled to that of density functional theory:

$$\omega_i^{final}(\mathbf{k}) \approx \omega_i^{DFTB}(\mathbf{k}) + \left(\omega_i^{DFT}(\mathbf{\Gamma}) - \omega_i^{DFTB}(\mathbf{\Gamma})\right) \tag{2.5}$$

The shifted pDOS $\omega_i^{final}(\mathbf{k})$ can then be introduced into 2.1 and a new vibrational contribution to $G(T, P, V)$ can be evaluated. The performance and viability of this method is detailed further in Chapter 3.

2.2 Acoustic Phonons

While DFTB allows for fast evaluation of optical mode phonon dispersion, the lowest-frequency acoustic modes associated with lattice vibrations converge poorly. These phonon modes are important to capture as they are readily populated even at ambient temperatures, and are significant contributors to finite temperature effects like thermal expansion. Therefore it is necessary to evaluate these separately. This is possible using the theory of elasticity:

$$T = C_{ijkl}E \tag{2.6}$$

where T and E are the stress and strain tensors respectively, and C_{ijkl} is the fourth-rank elastic constant tensor describing stress-strain relationships. The phase velocity surface can be solved in terms of the 3×3 Christoffel matrices given by

$$\Gamma_{ik} = \sum_{jl} \hat{n}_j C_{ijkl} \hat{n}_l \tag{2.7}$$

where $\hat{n}_j$ is a direction cosine.[46,47] The eigenvalues of this matrix yields the acoustic sound velocity ν.

$$\det |\Gamma_{ik} - \rho\nu^2 \delta_{ik}| = 0 \tag{2.8}$$

Acoustic sound velocity can be related to vibrational frequency using the Debye model, where the maximum Debye frequency is evaluated as

$$\omega_D = \frac{2\nu|k_{zb}|}{\pi} \tag{2.9}$$

The maximum Debye frequency defines the frequency of an acoustic vibration at the Brillouin zone boundary, k_{zb}. For inclusion in the shifted pDOS from Equation (2.5), the acoustic phonon dispersion between the zone center and k_{zb} is extrapolated sinusodally

$$\omega = \omega_D \sin\left(\frac{k}{k_{zb}}\frac{\pi}{2}\right) \tag{2.10}$$

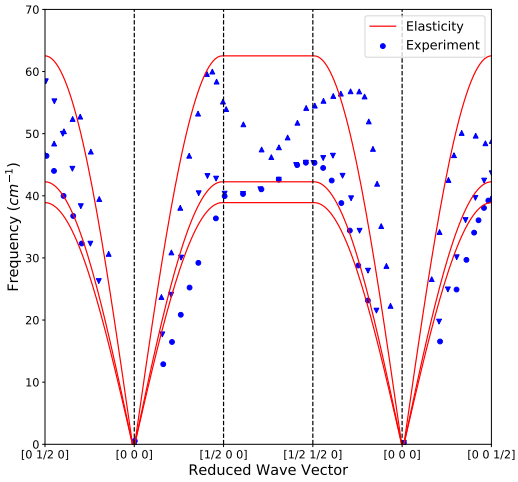

Figure 2.1: Comparison of acoustic phonon dispersion evaluated via DFT elastic constants vs. experimental acoustic in crystalline naphthalene at 6 K.

The ammended acoustic modes are replaced in the final pDOS, which is then integrated and included into the overall Gibbs free energy. Treatment of the acoustic phonons was verified for crystalline naphthalene in Figure 2.1. This approach introduces minimal additional computational effort while providing a more well-converged pDOS.

2.3 Thermal Expansion

Static phonon calculations employ the harmonic approximation for simplicity, which does not account for thermal expansion. Since all quantum chemical methods used in this work are performed at 0K, this leads to a systematic under-estimation of crystallographic cell volumes. Finite temperature thermodynamic contributions to crystal free energy can also be significant enough to cause changes in relative stability of polymorphs. Here, thermal expansion is evaluated implicitly using the quasi-harmonic approximation.

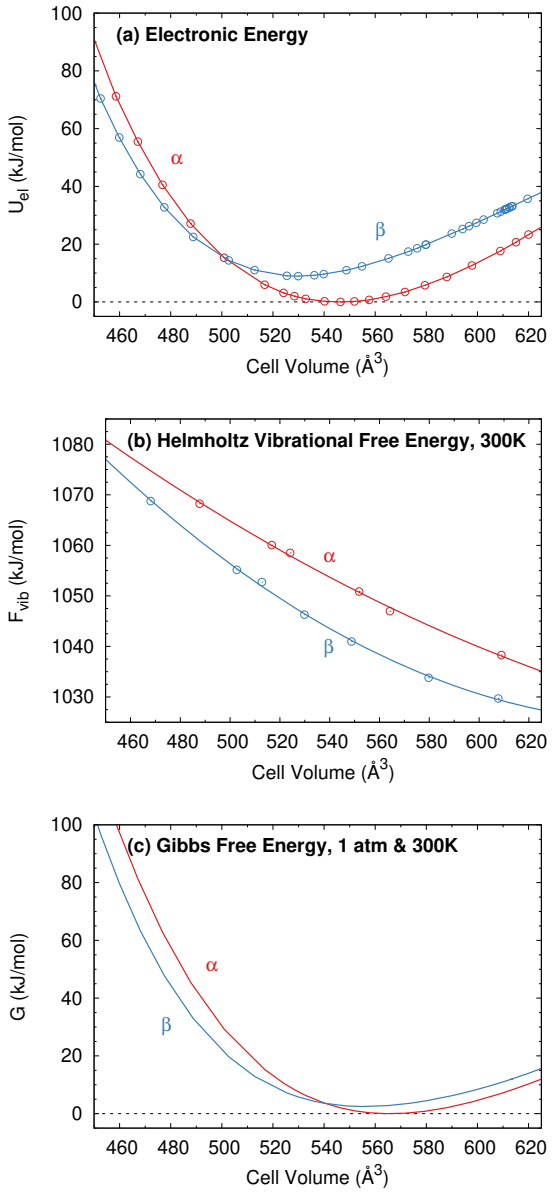

Figure 2.2: The quasi-harmonic treatment of resorcinol combines (a) electronic DFT energies and (b) Helmholtz vibrational free energies as a function of volume, which are then summed along with the PV term to obtain the Gibbs free energy. The predicted structures for the given thermodynamic conditions correspond to the minima of the $G(V)$ curves. Data shown here for 300 K and 1 atm.

The quasi-harmonic approximation (QHA) represents one of the simplest approaches for incorporating some anharmonicity into the harmonic phonon treatment. It typically works fairly well for molecular crystals up to moderately high temperatures below the melting point.[48,49] The QHA maps how the phonon frequencies and free energies vary with the molar volume of the crystal. In the implementation here, the electronic energy U_{el} is first computed as a function of volume by applying a series of positive and negative external isotropic pressures to the cell and relaxing the lattice parameters and atomic positions. This allows the unit cell to relax anisotropically, softens the one-dimensional potential energy curve compared to isotropic scaling of the lattice constants, and leads to improved description of the expansion/contraction.[50,51]

Next, the phonon density of states and free energies are evaluated at the equilibrium geometry and at several expanded and contracted volumes from the $U_{el}(V)$ curve. Each explicit phonon DOS evaluation was performed using the mixed DFT/DFTB approach described in Section 2.1, and care was taken to ensure the phonon DOS calculations were performed across the range of volumes associated with the temperatures and pressures of interest. After computing $F_{vib}(T)$ for each sampled structure at a chosen temperature, the F_{vib} values as a function of volume were fitted to a second-order polynomial. Summing $U_{el}(V)$, $F_{vib}(V)$, and PV for the given temperature and pressure produces $G(T,P,V)$. This free energy is fitted to a double-Murnaghan equation of state, in which the compression and expansion branches are fitted separately to the Murnaghan equation of state,[52]

$$G(V) = G_0 + \frac{B_0 V}{B_0'}\left[\frac{(V_0/V)^{B_0'}}{B_0' - 1} + 1\right] - \frac{B_0 V_0}{B_0' - 1} \tag{2.11}$$

and the two halves connect smoothly at the equilibrium volume V_0. From the fit, one obtains the optimal molar volume V_0, free energy at that volume G_0, the bulk modulus B_0, and the first derivative of the bulk modulus with respect to pressure, B_0'.

The effects of thermal expansion on cell volume and relative stability can be seen in Figure 2.2. Initially the two forms are separated by $\sim$10 *kJ/mol* at their respective equilibrium volumes as determined by U_{el} at 0 K as seen in Figure 2.2a. Applying the QHA and evaluating $G(T, P, V)$ at 1 atm and 300 K (Figure 2.2c) stabilizes β by $\sim$7 *kJ/mol* with respect to α, and shifts both of their equilibrium volumes by roughly 20 $\mathring{A}^3$, indicating thermal expansion. This technique allows us to predict more accurate finite temperature crystal structures and thermodynamic properties.

2.4 Transfer Integrals

Charge carrier mobility is an important property of organic molecular crystal based semiconductors. Here we introduce an important parameter for bulk mobility: the electronic transfer integral. This parameter is dependent on intermolecular separation in the crystal, which is a function of crystallographic cell parameters and therefore a function of temperature. The strategies introduced in this thesis are used to characterize the temperature dependence of this parameter as the crystal expands and intermolecular interactions are perturbed. Charge transport properties and their relationship to crystal structure is most clearly conveyed in the tight-binding approximation:[53]

$$H = \sum_i \epsilon_i a_i^+ a_i + \sum_{i \neq j} t_{ij} a_i^+ a_j \tag{2.12}$$

where a_i^+ and a_i are the creation and annihilation operators for an electron on molecular site i, respectively, ϵ_i is the electron site energy, and t_{ij} is the transfer integral.

Evaluation of t_{ij} from a single isolated dimer calculation can be approximated as half of the orbital splitting energy, however this has been shown to yield inaccurate transfer integrals as it neglects electronic polarization. Practical evaluation of t_{ij} instead involves a projection of the isolated monomer's frontier orbitals on those of the dimer.[53,54] The secular equation describing the dimer in the basis of monomer frontier orbitals is:

$$\mathbf{HC} - E\mathbf{SC} = 0 \quad ; \quad \mathbf{H} = \begin{pmatrix} e_1 & J_{12} \\ J_{12} & e_2 \end{pmatrix} \tag{2.13}$$

Where $\mathbf{H}$ is the electronic Hamiltonian, $\mathbf{C}$ is a matrix of orbital coefficients, E is the dimer energy, $\mathbf{S}$ is the overlap matrix, e_i is the site energy of molecule i and J_{ij} is the electronic transfer integral derived from the isolated molecular constituents of the dimer:

$$J_{ij} = \langle \Psi_i | H_{ij} | \Psi_j \rangle \tag{2.14}$$

Here, Ψ_i is the frontier orbital on the i^{th} molecule. J_{ij} is physically equivalent to t_{ij}, however it is represented in a non-orthogonal basis of the isolated monomers. This is corrected by projecting the orbitals of the monomers onto the orbitals of the dimer, giving an accurate transfer integral denoted J_{ij}^{eff}.[53–57] The present study focuses on the hole mobility, where the frontier orbitals of interest are the HOMO and HOMO-1 orbitals of the dimer, represented by the HOMO's of its constituent monomers.

In a semiconducting crystal, J_{ij}^{eff} is evaluated for each unique pair of molecules whose distance is close enough for considerable electronic coupling to occur. Exploiting translational and space group symmetry allows one to evaluate only the symmetrically unique subset of possible dimer pairs. While longer-range electron transfer can be important in evaluating bulk mobility, the present study focuses on local transfer integrals, which will be most sensitive to changes in crystal structure/volume.

Intermolecular charge transfer depends strongly on the degree of orbital overlap in the dimer pair. Changes in the crystal structure alter this overlap. For example, increasing intermolecular separation reduces the strength of interfacial π stacking interactions and the orbital overlap. Subtle changes in relative orientations of molecules, such as a face-to-edge angle in a herringbone-type packing, can also impact transfer integrals.[55] Accordingly, accurate knowledge of the unit cell is important when calculation transfer integrals and carrier mobility.

2.5 Intramolecular Conformational Energy Correction

Conventional density functionals used in solid-state calculations describe highly planar π conjugated regions of molecules poorly.[42,58–60] The issue stems from delocalization error in the approximate density functionals,[61] which artificially stabilizes extended π delocalization found in some organic molecules relative to nonplanar configurations.[42,59,60] Issues arising from DFT delocalization error have been identified in several organic crystals.[62–69]

To address the delocalization error issues inherent in common density functioanls, an intramolecular correction can be applied to periodic DFT lattice energies. This single-point energy correction replaces the intramolecular energies of the molecular unit with more accurate ones computed at the spin-component-scaled dispersion-corrected second-order Møller-Plesset perturbation theory (SCS-MP2D)[60] level,

$$E_{crystal} = E_{crystal}^{DFT} + \sum_{i=1}^{Z} \left(E_{molec,i}^{SCS\text{-}MP2D} - E_{molec,i}^{DFT} \right) \tag{2.15}$$

The molecular energies on the right-hand side are computed in the gas-phase using geometries extracted directly from the DFT-optimized crystal. The sum runs over all Z molecules in the unit cell, though space group symmetry can be exploited to compute the gas-phase molecular energies only for the molecules in the asymmetric unit. This correction has been employed successfully in several other systems.[42,66–68]

2.6 Crystal Structure Prediction

The CSP procedure in this work is conducted in a hierarchical fashion. First, crystals are generated and optimized with a cheap force field, then minimized further with an intermediate semi-empirical Hartree-Fock calculation, and finally minimized and ranked using more accurate electronic structure calculations. This is done to ensure that the landscape is adequately sampled and there is a wide variety of molecular conformations considered while remaining generally affordable. The CSP procedure is outlined as follows:

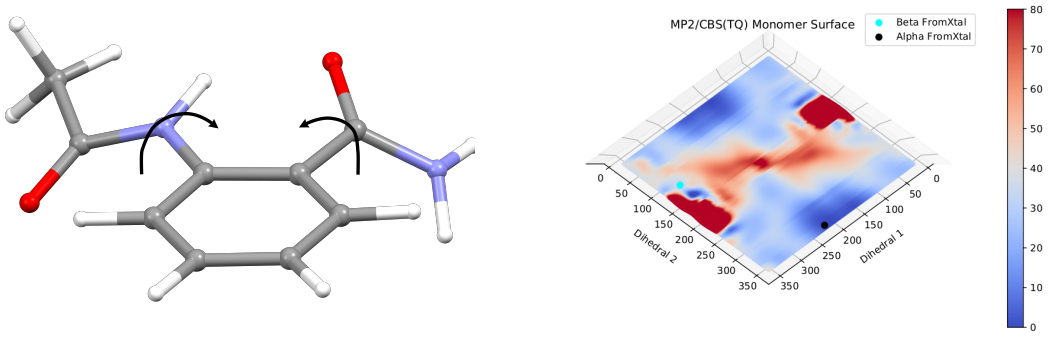

Figure 2.3: Intramolecular energy profile of ortho-acetaminobenzamide. The blue dot indicates the molecular configuration of the experimentally stable β-form, and the black indicates the α-form. Note how, although the β polymorph crystal lattice energy is more stable, the intramolecular energy of α is considerably lower.

0. Generation of the molecular geometries: Initial gas-phase molecular structures were constructed and optimized. For molecules with intramolecular flexibility, energy landscapes were constructed as to restrict the space in which to sample the crystals but to allow some molecular flexibility for structural variety. These coincide with the red regions and the blue/white regions of Figure 2.3, respectively.

1. Generation of Candidate Crystal Structures: Optimized monomers were then used to seed randomly-generated crystals. The search assumed $Z' = 1$ and covered 11 common space groups: $P1$, $P\bar{1}$, $P2_1$, $C2$, Cc, $P2_1/c$, $C2/c$, $P2_12_12_1$, $Pca2_1$, $Pna2_1$, and $Pbca$.

Typically, several thousand structures for each space group are generated and optimized at the molecular mechanics level. This leads to duplicate structures quite frequently that need to be removed from the set prior to further landscape refinement. Crystal struc-

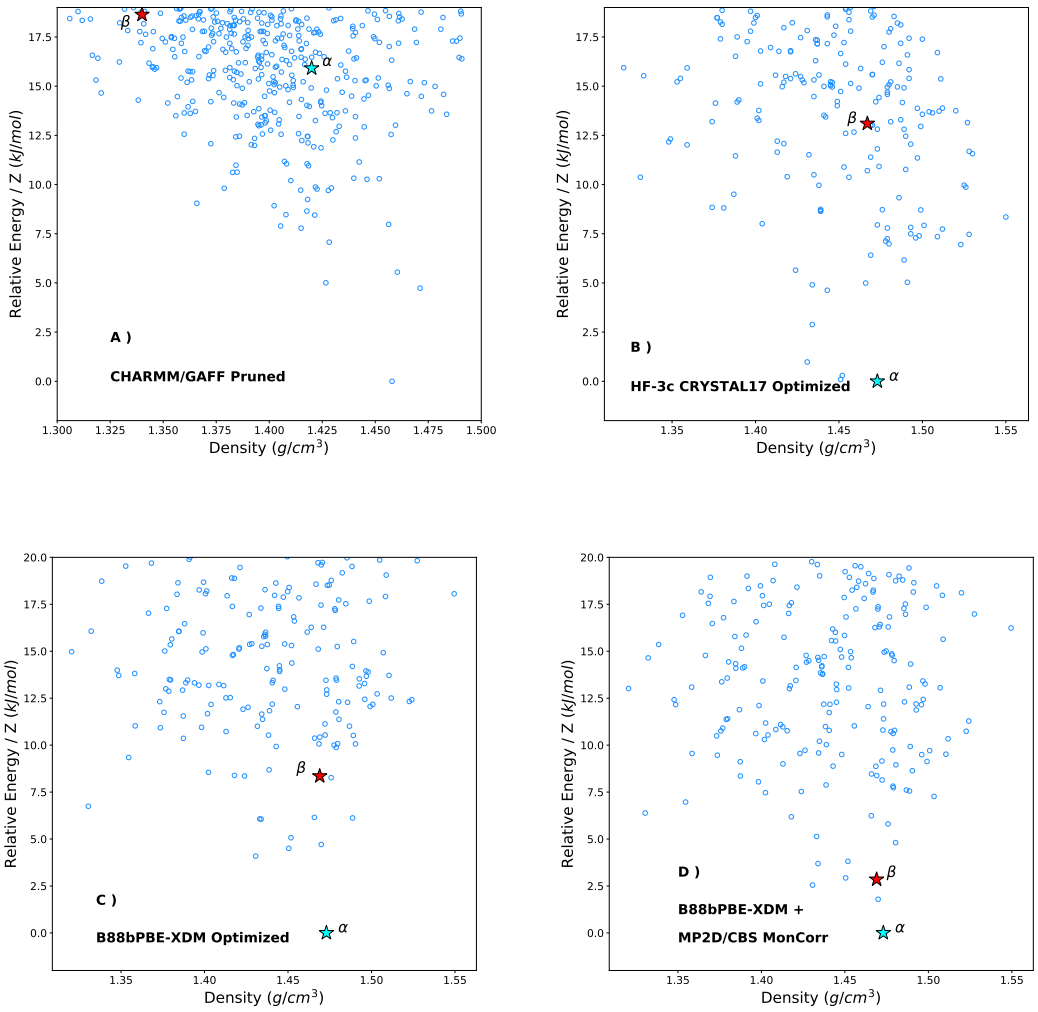

Figure 2.4: Primary steps in hierarchical crystal structure prediction for ortho-acetaminobenzamide (ACBNZA). **(A)** is evaluated with CHARMM/GAFF, **(B)** with semi-empirical HF-3c, **(C)** with periodic DFT, and **(D)** with an intramolecular conformational energy correction.

tures that exhibit relative energies of less than 1 kJ/mol, densities of less than 0.03 g/cm^3, and a root-mean-squared-deviation of atomic positions in a 15-molecule cluster of less than 0.25 $\AA$ are considered duplicates. One of the structures will be kept and the other discarded. All unique crystals that lie within some energy window of the predicted global minimum structure, 25 kJ/mol in this case unless otherwise indicated, of the predicted global minimum are subjected to the next round of refinement. An example landscape is shown in Figure 1.4a.

2. Intermediate Structure and Energy Refinement: A second stage of crystal structure geometry and energy refinements is performed on the low-energy structures from **Step 1** using the composite Hartree-Fock (HF-3c) model.[70] HF-3c combines minimal-basis-set HF with corrections for van der Waals dispersion, basis set superposition error, and a short-ranged basis-set incompleteness correction. HF-3c was chosen because it should be considerably more accurate than molecular mechanics, while still being 5–10-fold less computationally demanding than larger-basis periodic density functional theory (DFT) methods. Structures refined with HF-3c are also tested for duplicates, pruned, and cut off once more at 10 kJ/mol for further refinement. This step offers a significant correction over molecular mechanics as seen in Figure 1.4b.

3. Final Periodic DFT Refinement: Periodic DFT geometry optimizations were then carried out on the low-energy HF-3c structures. DFT procedures are further outlined in **Section 2.8**. Final DFT landscapes provide the lattice energy used in the final ranking, however require the intramolecular correction outlined in Section 2.5.

4. Single-Point Intramolecular SCS-MP2D Energy Corrections to DFT: The final stage of energy refinement is to correct for electron delocalization error. Spurious stabilization of delocalized charge causes significant errors in conformational polymorphism where the extent of π delocalization changes between polymorphs.[65–69] Intramolecular energies are re-evaluated with correlated wave functions and total crystal energy is expressed using Equation 2.15.

2.7 Photomechanical Reactions

A photomechanical reaction is a type of chemical reaction in which light energy is converted to mechanical work. This can take the form of twisting, stretching, and bending, among other interesting forms of movement following the transformation from reactant to product. These materials have promise in several fields relying on smart materials such as wearable electronics, artificial muscles, actuators, and soft robotics.[71] While these materials have been well studied for some time, detailed study of microstructure has been lacking. This thesis offers a solution in characterizing the structural transformation of photomechanical systems computationally.

Photomechanical reactions in the solid state can occur in a variety of ways, including intramolecular ring closure,[36] bond rotation,[72] [2 + 2] photodimerization, and [4 + 4] photodimerization.[73,74] Particular focus will be placed on the [4 + 4] mechanism, which involves a ring formation across cofacial polycyclic aromatics, as shown in Figure 2.5. Reactions of this type are of particular interest because of relatively large expansions of the cell parameters and the stiff elastic moduli of these crystals.[75] Unfortunately precise knowl-

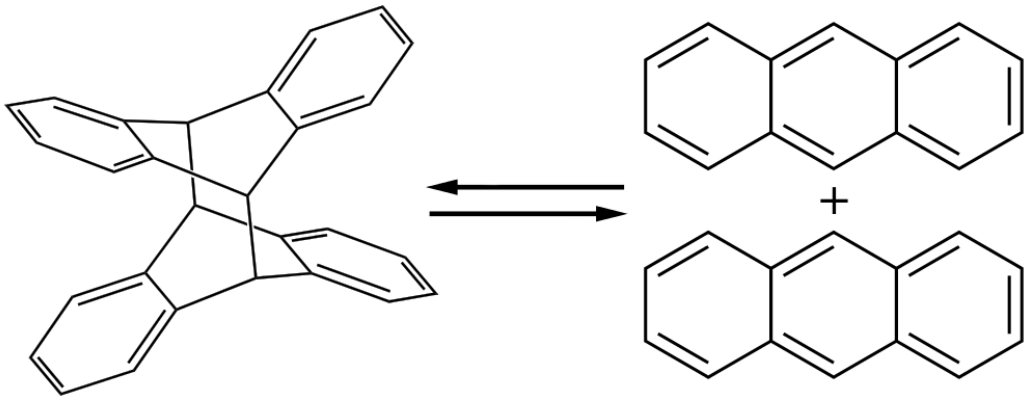

Figure 2.5: [4+4] photodimerization reaction of anthracene.

edge crystal structure of the product, also called the solid state reacted dimer (SSRD), is difficult to glean. This reaction can result in rapid degradation of the SSRD crystal through cracking or shattering, poor conversion to product because of thermal reversibility, or exhibit positive photochromism preventing complete conversion to product. CSP can provide a crucial pathway to SSRD determination, a key component in the evaluation of an array of important macroscopic properties.

A new topochemical procedure for generating the SSRD from the unreacted monomer crystal is developed here. First, some assumptions:

1. All reactant monomer pairs are converted

2. The reaction occurs instantaneously

These assumptions allow us to generate the SSRD with information from the reactant crystal, i.e. the molecular packing and crystallographic cell parameters. The cyclized photodimer product can be readily solved in the gas phase and used to substitute the cofacial monomers in the reactant unit cell. Instantaneous conversion to the SSRD results in the photodimerized product being present in the unit cell of the reactant, also

called the "proto-SSRD". This structure then is allowed to fully relax into the SSRD, and the differences in unit cell vectors from proto-SSRD → SSRD define the strain for anisotropic work:

$$C_{proto} = C_{eq}(\chi_{ij} + I) \tag{2.16}$$

$$\chi_{ij} = C_{proto}(C_{eq})^{-1} - I \tag{2.17}$$

$$\epsilon_{ij} = \frac{1}{2}(\chi_{ij} + \chi_{ij}) \tag{2.18}$$

where C_{proto} and C_{eq} are the proto-SSRD and relaxed SSRD unit cell row vectors, respectfully, χ_{ij} is the deformation, and ϵ_{ij} is the symmetric strain. Anisotropic work is evaluated and projected onto a unit sphere:

$$W(\hat{n}) = \frac{1}{2}\hat{n}^{\intercal}\sigma_{ij}\epsilon_{ij}\hat{n} \tag{2.19}$$

where $\hat{n}$ is the spherical polar unit vector and σ_{ij} is the stress tensor. Accurate determination of the SSRD allows us to evaluate anisotropic work W, which can serve as a descriptor for photomechanical device viability. Full CSP provides insight on additional forms that may be close by on the crystal landscape and quantify the thermodynamic stability relative to reachable solution grown forms or even others that may be accessible via photochemical processes. Further, this procedure can be heavily automated, showing significant potential for crystal engineering.

2.8 Computational Details

2.8.1 Density Functional Theory

Density functional theory (DFT) calculations were carried out using a variety of different software packages. Geometry optimizations and phonon force calculations for periodic molecular crystals were performed using the B86bPBE density functional and the XDM dispersion correction, as implemented in Quantum Espresso v6.4.1.[76,77] A plane-wave cutoff of 50 Ry and Γ-centered Monkhorst-Pack k-point grids with a spacing of 0.06 $\mathring{A}^{-1}$ are used throughout unless otherwise specified.

Additional periodic DFT calculations, namely for organic semiconducting crystals in Chapter 4, were performed with CRYSTAL17 using the Perdew-Burke-Erzhoff (PBE) density functional with Grimme's D3 dispersion correction and a 6-311G(2d,2p) atom-centered basis.[78,79]

Finally, gas-phase DFT optimizations for initiating CSP procedures, dihedral scanning, and evaluating charge transfer integrals were carried out with Gaussian09. The B3LYP hybrid density functional with a 6-311+G(d) basis set was used unless otherwise indicated.

2.8.2 Semi-empirical Methods

Semi-empirical quantum mechanical methods served as both the "low level" determination of supercell phonon dispersion in free energy assignment as well as the intermediate step during the crystal structure prediction ranking procedure.

Density functional tight binding (DFTB) was used for semi-empirical force calculations in the phonon mode matching procedure within the DFTB+ software package.[80,81]

Harmonic phonon calculations were performed using the frozen-phonon method as implemented in the Phonopy software package v2.4.2.[82]

Composite Hartree-Fock with a minimal basis set (HF-3c/MINIX) was used within the *CRYSTAL17* software package.[70,83]

2.8.3 CSP Sampling

Initial structures for CSP procedures were generated from optimized gas phase molecules using the Pyxtal python module v0.2.9.[84] Atomic coordinates and unit cell parameters were them optimized using molecular mechanics using the Generalized Amber Force Field (GAFF)[85] within the CHARMM 45b2 software package.[86]

2.8.4 Moller-Plesset Perturbation Theory

The gas-phase SCS-MP2D molecular calculations were performed with Gaussian basis sets and no periodic boundary conditions. They were extrapolated to the complete-basis-set limit by combining HF/aug-cc-pVQZ[87] with correlation energies extrapolated from the aug-cc-pVTZ and aug-cc-pVQZ basis sets.[88] The MP2 calculations were performed with Psi4 v.1.3.2,[89] while the spin-component scaling and dispersion corrections in SCS-MP2D were evaluated using the MP2D software library, available on GitHub at https://github.com/Chandemonium/MP2D.[90,91]

Chapter 3

Accurate Phonon Densities of State

Phonon contributions to organic crystal structures and thermochemical properties can be significant, but computing a well-converged phonon density of states with lattice dynamics and periodic density functional theory (DFT) is often computationally expensive due to the need for large supercells. Using semi-empirical methods like density functional tight binding (DFTB) instead of DFT can reduce the computational costs dramatically, albeit with noticeable reductions in accuracy. This work proposes approximating the phonon density of states via a relatively inexpensive DFTB supercell treatment of the phonon dispersion that is then corrected by shifting the individual phonon modes according to the difference between the DFT and DFTB phonon frequencies at the Γ-point. The acoustic modes are then computed at the DFT level from the elastic constants. In several small-molecule crystal test cases, this combined approach reproduces DFT thermochemistry with kJ/mol

accuracy and 1–2 orders of magnitude less computational effort. Finally, this approach is applied to computing the free energy differences between the five crystal polymorphs of oxalyl dihydrazide.

3.1 Introduction

Organic molecular crystals are prevalent in pharmaceuticals, organic semiconductors, energetic materials, and many other organic materials. Different crystal packings of a given molecule, known as polymorphs, can exhibit distinct physical properties, such as stability, solubility or charge-carrier mobility. Knowledge of the different possible polymorphs and their relative stabilities, called the crystal energy landscape, can be valuable for designing new materials with specific properties. However, reliable prediction of crystal energy landscapes is hindered by the small, few kJ/mol or less free energy differences that often separate different polymorphs.[92–94] Further complications arise from how those relative thermochemical stabilities can vary with temperature and pressure.[95] Accurate computational models are often required to map out these solid form landscapes correctly.[65,66,96–98]

Polymorph free energies are dominated by the electronic lattice energy contribution. Indeed, lattice energy rankings have long been the primary metric employed when ranking predicted crystal structures.[96,99,100] However, it is also clear that the vibrational contributions to the free energy can be important. Surveys suggest that F_{vib} contributions are sufficiently large to reverse the lattice energy stability orderings in 10–20% of polymorphic systems at room temperature.[92,101] Phonon contributions are crucial to understanding why aspirin form I is thermodynamically preferred over form II,[102] and they have proved

necessary to predict the thermodynamically most stable polymorphs correctly for several molecules in the blind tests of crystal structure prediction.[97,98]

More elaborate quasi-harmonic phonon treatments describe how the crystal structure and phonon frequencies change with temperature and pressure. Accounting for these changes is important for predicting properties including lattice parameters/molar volumes,[103–105] thermochemical properties,[50,51,103,104,106–108] mechanical properties,[109,110] vibrational spectra,[111,112] and nuclear magnetic resonance chemical shifts.[113] Capturing those pressure- and temperature-dependent changes in thermochemical properties proved essential to predicting the phase diagram of methanol, for example.[51] Beyond harmonic or quasi-harmonic treatments, there is increasing evidence that dynamics plays an important role in the structures and thermochemical stabilities of molecular crystals.[114–117]

Unfortunately, even within the harmonic approximation, computing a well-converged phonon density of states for a chemically interesting organic crystal can be very computationally demanding. The most straightforward approach to computing harmonic phonon modes relies on lattice dynamical calculations performed in large supercells to capture phonon dispersion.[118] Typically, the supercell should extend 10–15 Å in each direction,[119,120] and it will often contain hundreds of atoms. Density functional perturbation theory avoids the need for supercells and can compute the phonons at lower cost,[121] but the calculations remain computationally demanding.

One means of reducing the computational costs associated with evaluating the harmonic phonon density of states (pDOS) and the vibrational partition functions is to compute the phonons at a lower level of theory. For example, the use of DFT-optimized geometries

and phonon frequencies together with single-point energies computed via correlated wave function methods has proved effective.[122]

Alternatively, some researchers have explored the use of computationally inexpensive density functional tight binding (DFTB) models for predicting the structures and phonons. DFTB is a semi-empirical quantum mechanical method that is based off of the generalized gradient approximation (GGA) of DFT.[123,124] It expresses the electronic energy as a Taylor expansion about a reference DFT electron density ρ_0. The present work focuses on DFTB3, which includes terms through third-order in the expansion.[125] For systems like molecular crystals in which non-covalent interactions are important, DFTB3 must be paired with a dispersion correction, such as Grimme's D3 model.[79] Hydrogen bonding corrections can provide further improvements.[126] The combination of a minimal basis set of Slater-type orbitals and semi-empirical parameterization speeds DFTB by up to three orders of magnitude over *ab initio* DFT.

In the context of molecular crystals, DFTB has proved effective for optimizing crystal structures,[127] and it predicts the thermal expansion in carbamazepine accurately.[128] It can provide useful intermediate rankings of crystal structures in a multi-step, hierarchical crystal structure prediction,[129] and it can provide good embedding environment for DFT.[130] On the other hand, existing DFTB approximations and parameterizations appear insufficiently accurate for the final ranking stages of crystal structure prediction.[129,131–134] On the X23 benchmark set of molecular crystals, for example, it exhibits a mean absolute deviation in the lattice energies of 10 kJ/mol, compared to 5–6 kJ/mol for many dispersion-corrected GGA density functionals.[131,132] As the data presented below will demonstrate,

DFTB performance is often noticeably worse than DFT for computing the phonon density of states and the thermochemical properties derived from it.

Here, we propose a strategy for computing the harmonic pDOS that combines the computational efficiency of DFTB with the greater accuracy of DFT. In this approach, a supercell harmonic phonon calculation is performed at the dispersion-corrected DFTB3 level to capture the phonon dispersion, which is far more affordable than GGA DFT. However, the limitations of DFTB semi-empirical parameterizations mean that there will often be sizable errors in the phonon frequencies. Therefore, an additional Γ-point harmonic phonon frequency calculation is performed on the crystallographic unit cell with DFT. By matching the Γ-point modes between DFT and DFTB, we determine an additive offset for each individual DFTB phonon frequency that enables shifting of the DFTB dispersion curves such that they agree exactly with DFT at the Γ point. This simple shift improves the agreement between the low-cost DFTB and full DFT pDOS considerably. This corrected DFTB pDOS can be computed at least 1–2 orders of magnitude faster than the full supercell DFT calculation while sacrificing only modest accuracy in the final predicted thermochemical properties. Although the present study focuses purely on a harmonic phonon description, the generalization of the ideas here to a quasi-harmonic treatment for the more reliable treatment of temperature-dependent effects would be straightforward.

3.2 Theory

3.2.1 Approximating the phonon density of states

The principal finite-temperature contributions to the Gibbs free energy of a crystal arise from the Helmholtz vibrational energy, $F_{vib}(T)$. From statistical thermodynamics and the harmonic approximation, one obtains,

$$F_{vib}(T) = 3nN_A k_B T \int_0^\infty \ln\left[2\sinh\left(\frac{\hbar\omega}{2k_B T}\right)\right] g(\omega) d\omega \tag{3.1}$$

where n is the number of atoms in the unit cell, N_A is Avogadro's number, $g(\omega)$ is the phonon density of states as a function of frequency ω, $\hbar$ is Planck's constant, k_B is the Boltzman constant, and T is temperature.[45] The density of states $g(\omega)$ is normalized to unity (hence the factor of $3n$ in Eq 5.5) and is expressed as a kernel density estimate (KDE) of the overall frequency distribution for all phonon modes ω_i and all $\mathbf{k}$ by placing primitive Gaussian functions of width 5 cm^{-1} at each discrete phonon mode about each sampled k-point. Use of the KDE improves the convergence of thermodynamic properties with respect to phonon sampling.[101]

To evaluate the phonon dispersion in reciprocal space that contributes to the phonon density of states, it is necessary to generate a supercell consisting of multiple crystallographic unit cells in order to describe how the phonon frequency changes with respect to its interaction with neighboring cells. Doing so often dramatically increases the size of the system to be modeled and can make the computational cost prohibitive with DFT or other *ab initio* methods. The complexity introduced by phonon dispersion is often circum-

vented by simply evaluating the frequencies at the Γ-point (zone center, $\mathbf{k} = \mathbf{0}$) of the unit cell, which can be accomplished without supercell expansion. However, this Γ-point-only approximation omits potentially important contributions to the pDOS from the acoustic modes and dispersion of the optical modes away from the zone center.

Before describing the proposed efficient approach for computing the pDOS, the theory of lattice dynamics will be reviewed briefly. Within the harmonic approximation, the crystal potential can be approximated via the second term of the Taylor expansion of overall potential with respect to atomic displacements,

$$U = U_0 + \sum_{l,\alpha} U_\alpha^l u_\alpha^l + \frac{1}{2} \sum_{l,l',\alpha,\beta} U_{\alpha\beta}^{ll'} u_\alpha^l u_\beta^{l'} + \cdots \tag{3.2}$$

$$U_{\alpha\beta}^{ll'} = \frac{\partial^2 U}{\partial u_\alpha^l \partial u_\beta^{l'}} \tag{3.3}$$

where U is crystal potential and u_α^l is the displacement of atom l in direction α. U_α^l represents the nuclear gradient of the potential with respect to the displacement of atom l, which equals zero when the structure has been optimized to a stationary point. $V_{\alpha\beta}^{ll'}$ is the matrix of force constants describing the forces felt by atom l in the central unit cell after the displacement of atom l'. Mass weighting and transforming the coordinates into reciprocal space yields the dynamical matrix $D_{\alpha\beta}$, which can be diagonalized according to:

$$\omega^2 u_\alpha = \sum_\beta D_{\alpha\beta} u_\beta \quad \text{where} \quad D_{\alpha\beta} = \frac{1}{\sqrt{m_l m_{l'}}} \sum_n U_{\alpha,\beta}^{l,l'} \exp(-i\mathbf{k} \cdot \mathbf{r}_n) \tag{3.4}$$

This dynamical matrix equation relates atomic displacement, force response, and resulting vibrational frequencies ω. The normal mode eigenvectors u_α are normalized vectors describing the collective movement of the atoms that result in the frequency of that mode.

The hybrid approach proposed here seeks to benefit from the low-computational cost of DFTB while mitigating its comparatively lower accuracy. In particular, we capture phonon dispersion via large supercell DFTB calculations. The low-cost of DFTB makes it more feasible to converge the pDOS with respect to supercell size.[132,135] To address the accuracy limitations of the DFTB pDOS, an additive correction is applied to the frequencies associated with each DFTB phonon mode. This shift is computed separately for each mode i as the difference between the DFT and DFTB frequencies at the Γ-point,

$$\omega_i^{final}(\mathbf{k}) \approx \omega_i^{DFTB}(\mathbf{k}) + \left(\omega_i^{DFT}(\mathbf{\Gamma}) - \omega_i^{DFTB}(\mathbf{\Gamma})\right) \tag{3.5}$$

Performing this frequency shift does require computing the DFT frequencies at the Γ point, which is far more expensive than computing them with DFTB for the same unit cell. On the other hand, the cost of the DFT Γ-point calculation can be orders of magnitude cheaper than computing the DFT frequencies in a large supercell. Overall, this simple correction approximates the DFT phonon density of states well at a fraction of the usual computational cost.

The approximation in Eq 3.5 assumes that the dispersion in individual phonon bands is similar regardless of whether they are computed with DFT or DFTB, and that the simple additive correction is sufficient to improve the DFTB bands. That assumption is imperfect—our own anecdotal examinations of the pDOS for a few systems suggest that the

DFTB3-D3(BJ) bands with the 3ob-3-1 parameter set[136] tend to exhibit greater frequency dispersion across the Brillouin zone compared to their B86bPBE-XDM DFT counterparts. Nevertheless, these discrepancies in individual phonon bands partially cancel in the total pDOS, and the correction improves the overall phonon density of states considerably compared to the target DFT calculations. Note too that this Γ-point shift does not work for the three acoustic modes, since those phonon frequencies equal zero at $\mathbf{k} = \mathbf{0}$, regardless of the electronic structure treatment. The acoustic modes will be handled separately, as described in Section 3.2.2.

Employing this proposed hybrid pDOS calculation strategy requires addressing a few practical issues. First, the harmonic approximation requires that the crystal structure has been relaxed to an energy minimum at the same level of theory as the lattice dynamics calculation. Accordingly, the crystal geometry is first optimized with DFT for the Γ-point phonon calculation. The DFT-optimized unit cell is then relaxed with DFTB for the supercell lattice dynamics calculation.

Second, applying Eq 3.5 requires identifying which DFT phonon modes correspond to which DFTB modes. Due to differences in the optimized structures and the electronic structure models, the phonon frequencies will differ both in magnitude and the ordering obtained from the eigenvalue solver. The normal mode eigenvectors obtained from diagonalizing the Γ-point dynamical matrix (Eq 3.4) at each level of theory will also likely differ quantitatively, though they should still correspond to qualitatively similar atomic motions. Therefore, to match phonon normal modes between the two levels of theory, the overlap matrix $\langle u_\alpha^{DFTB}(\mathbf{\Gamma})|u_\beta^{DFT}(\mathbf{\Gamma})\rangle$ is computed as the set of all possible inner products between

the DFT and DFTB normal modes at the Γ-point. The optimal mode match for each DFT normal mode is then assigned based on the single largest overlapping DFTB normal mode eigenvector (with each DFTB mode being allowed to match only one DFT mode).

Figure 3.1 plots a sample overlap matrix for the DFT (B86bPBE-XDM) and DFTB3-D3(BJ) normal mode eigenvectors of phase I carbon dioxide at the Γ-point (see Section 3.3 for computational details). With only 12 atoms in the unit cell and 33 normal modes (excluding the acoustic modes), the overlap matrix can be visualized easily. For the vast majority of modes, there exists a single, clear match between the two levels of theory. The degree of the overlap can be smaller for degenerate modes, since the corresponding eigenvectors are not unique. However, this does not present a problem in practice as long as the correct subspaces are identified, since individual assignments within the subspace are arbitrary. Once the DFTB bands have been fully assigned, they can be shifted according to Eq 3.5 to construct the final approximate pDOS.

The overlap-based mode assignment has proved straightforward for all systems studied thus far. It is conceivable that one might find a system for which the simpler DFTB model performs poorly and for which assigning the modes becomes more difficult. As the DFTB models and parameterizations are continually improved, however, the likelihood of such difficulties will hopefully decrease even further.

3.2.2 Treatment of the acoustic modes

As noted above, the Γ-point shift cannot be applied to the three acoustic modes, since those frequencies equal zero at the Γ point by definition, regardless of the model

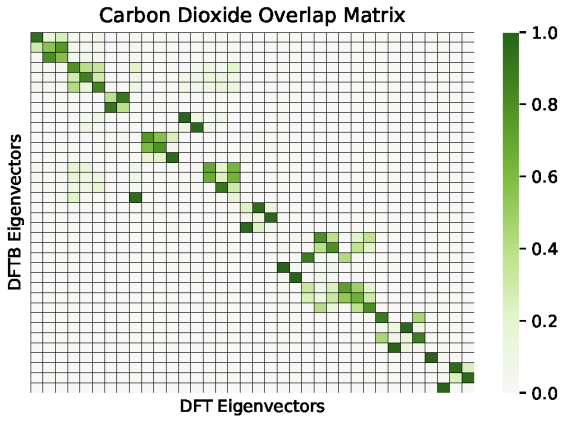

Figure 3.1: Sample normal mode overlap matrix computed between the DFTB3-D3(BJ) and DFT (B86bPBE-XDM) normal mode eigenvectors for phase I CO_2. Darker green corresponds to a larger-magnitude overlap.

chemistry employed. Moreover, very large supercells are required to converge the acoustic modes, which can become computationally expensive even with DFTB. Finally, it is unclear how well DFTB will model the soft acoustic vibrations in molecular crystals, given that such interactions were not a focus of the parameterization.

Instead, the acoustic modes here are solved for separately with DFT via the stress-strain relationships from the theory of elasticity,[47,137]

$$T = \lambda E \tag{3.6}$$

where T and E are the stress and strain tensors respectively, and λ is the matrix of elastic constants describing the stress-strain relationship.

Acoustic sound velocities ν are related to the elastic constants using the 3×3 Christoffel matrices Γ_{ik} for each unique direction in the Brillouin zone. The eigenvalues of these matrices describe the velocity of sound propagating through the crystal, which is

associated with the frequency of the acoustic phonons.

$$\det |\Gamma_{ik} - \rho\nu^2\delta_{ik}| = 0 \tag{3.7}$$

Acoustic sound velocity can be related to vibrational frequency using the Debye model, where the maximum Debye frequency ω_D is evaluated as

$$\omega_D = \frac{2\nu|k_{zb}|}{\pi} \tag{3.8}$$

The maximum Debye frequency defines the frequency of an acoustic vibration at the Brillouin zone boundary, k_{zb}. For inclusion in the shifted pDOS from Equation (3.5), the acoustic phonon dispersion between the zone center and k_{zb} is extrapolated sinusodally

$$\omega = \omega_D \sin\left(\frac{k}{k_{zb}}\frac{\pi}{2}\right) \tag{3.9}$$

Once the acoustic mode dispersion has been evaluated, it is substituted in lieu of the DFTB acoustic modes in the final density of states.

Figure 3.2 plots the acoustic modes for phase I carbon dioxide as computed directly from DFT in a $3 \times 3 \times 3$ supercell and from the elastic constant approach described above. Even in this 16.9 Å dimension supercell, the DFT acoustic modes retain significant imaginary components away from the Γ point. The elastic constant approach eliminates the imaginary components and broadly captures the k-point dependence of these modes, though the elastic constant model underestimates the frequencies by up to $\sim$10–15 cm^{-1} and

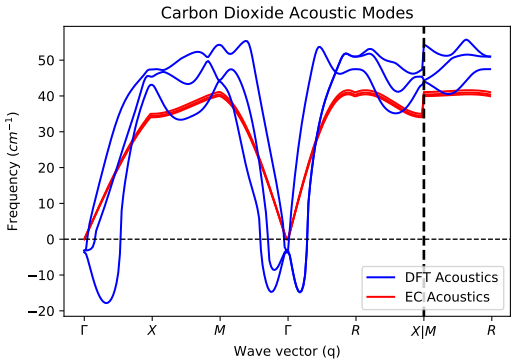

Figure 3.2: Comparison of the acoustic phonon mode dispersion curves for crystalline carbon dioxide as computed directly from lattice dynamics (blue) versus those derived from the elastic constants (red).

exhibits reduced dispersion across the Brillouin zone. Nevertheless, the room-temperature Helmholtz vibrational free energies obtained from the acoustic mode contributions to the phonon density of states differ by only 0.2 kJ/mol between the two models.

3.3 Computational Methods

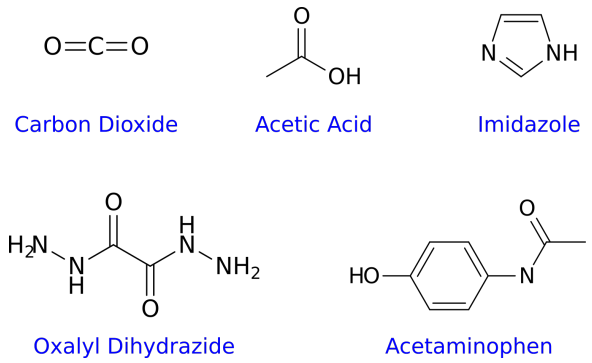

Figure 3.3: The five species whose crystals are modeled here.

The atomic positions and lattice parameters of all crystals were fully relaxed starting from experimental crystal structures. The structure of carbon dioxide phase I was

obtained from Ref. 138, while crystal structures of acetic acid (ACETAC01),[139] imidazole (IMAZOL06),[140] acetaminophen (HXACAN01),[141] and the five polymorphs of oxalyl dihydrazide (VIPKIO01–VIPKIO05)[142] were taken from the Cambridge Structural Database using the reference codes indicated in parentheses above. Molecular structures of these species are shown in Figure 3.3

The DFT geometry optimizations and finite displacements for the phonon calculations were performed using the B86bPBE density functional and the XDM dispersion correction, as implemented in Quantum Espresso v6.4.1.[76] The calculations employed a 40 Ry (acetic acid, due to the large supercell), 50 Ry (carbon dioxide, imidazole, and acetaminophen), or 60 Ry cutoff (oxalyl dihydrazide). Core electrons were treated according to the projector augmented wave (PAW) approach using PAW potentials for H, C, N, and O produced with A. Dal Corso's Atomic code v6.1. The DFTB3-D3 calculations were performed using the DFTB+ program[80,81] and the 3ob-3-1 Slater-Koster file parameter set.[136] Hubbard derivatives and empirical dispersion coefficients were set to the values recommended in the documentation.

For assessing the approximations proposed here, the specific choice of density functional and DFTB parameterization used to approximate the pDOS are somewhat arbitrary. The B86bPBE-XDM functional used here has performed well in many earlier molecular crystal studies.[63,77,97,143] Similarly, the dispersion-corrected DFTB3-D3(BJ) parameterization should also perform well for organic species like those studied here.[136] One might further improve the quality of these models by switching to a hybrid density functional[64,98] or by including hydrogen bonding corrections in DFTB, for example.[126] Nevertheless, the

Table 3.1: Supercell sizes used in the phonon calculations. Cells were chosen to achieve ∼15 Å or more in each direction, while also ensuring the supercell DFT calculations were feasible for the smaller molecules.

Crystal	Supercell
Carbon Dioxide	3×3×3
Acetic Acid	2×4×3
Imidazole	2×3×2
α Oxalyl Dihydrazide	4×3×2
β Oxalyl Dihydrazide	5×2×3
γ Oxalyl Dihydrazide	4×2×3
δ Oxalyl Dihydrazide	5×2×3
ϵ Oxalyl Dihydrazide	3×4×2
Acetaminophen	2×2×3

results here focus primarily on how well the shifted DFTB pDOS reproduces the target DFT one and the impact of this on computed thermochemical properties, rather than carefully examining how well these particular DFT results reproduce experiment.

The harmonic phonon calculations were performed with Phonopy v1.13.2,[82] which generates a series of finite displacements in accord with the supercell/frozen phonon method. The DFT Γ-point calculations employ the relaxed crystallographic unit cell, while the DFTB phonon dispersion calculations employ a supercell constructed by replicating the unit cell after DFTB relaxation. To ensure good convergence of the force constants,[135] supercells were chosen to achieve dimensions of 15 Å or greater along each lattice vector. Table 3.1 lists the specific supercell sizes used. The dynamical matrix can then be diagonalized at various wave vectors $\mathbf{k}$. The Γ-point DFTB phonon frequencies used to match normal modes between DFT and DFTB are obtained at $\mathbf{k} = \mathbf{0}$ from the supercell phonon calculation, while the remaining values at $\mathbf{k} \neq \mathbf{0}$ provide the raw DFTB3-D3(BJ) pDOS. High-symmetry $\mathbf{k}$ paths were assigned according to the schemes in Ref. 144.

The matching of the phonon normal modes between DFT and DFTB and the elastic constant solver algorithm were performed using in-house Python3 code. Elastic constants were solved in a similar manner to how they are implemented in Thermo_PW module of the Quantum Espresso suite.[145] Thermo_PW evaluates the elastic properties of a crystal by calculating the stress response for a series of strained conformations. Various magnitudes of each unique strain are applied, and the corresponding elastic constant is determined through a quadratic fit. Six unique stress/strain relationships are typically required to construct the elastic constant matrix, though this can often be simplified by exploiting crystal symmetry.

The stress/strain relationships were calculated via DFT. Test calculations found that DFTB3-D3(BJ) with the 3ob-3-1 parameterization gave elastic constants that differed considerably from the DFT ones. Performing these calculations with DFT instead of DFTB does not significantly increase the overall cost. The number of stress-strain relationships is independent of unit cell size, and evaluating each of the six stress-strain relationships involves four fixed-cell geometry optimizations of a slightly distorted crystallographic unit cell (rather than a supercell). All benchmark DFT phonon calculations here include the acoustic mode correction. To analyze how much this correction contributes, some DFTB results below include it, while others do not (as specified below).

3.4 Results and Discussion

To begin, Figure 3.4 compares the B86bPBE-XDM phonon density of states for the α polymorph of oxalyl dihydrazide against the DFTB3-D3(BJ) 3ob-3-1 ones before

and after applying the Γ-point correction in Eq 3.5. These two models are referred to as "DFT" and "DFTB" for the remainder of the paper. For computational simplicity, the DFT and DFTB phonon dispersion calculations in this illustrative example employed only a 4×1×1 supercell (4×3×2 would be more appropriate for quantitative accuracy). As can be seen in Figure 3.4a, the raw DFTB pDOS differs noticeably from the DFT one. The discrepancies are most obvious in the intramolecular bends and stretches in the ∼500-3500 cm^{-1} range. For example, a number of the DFTB bending modes in the 540-595 cm^{-1} range occur at 870–900 cm^{-1} in the DFT pDOS. Considering all DFT phonon modes above 500 cm^{-1}, the mean and mean absolute difference between DFT and DFTB are 54 and 84 cm^{-1}, respectively. In other words, the DFTB model is systematically underestimating the bending and stretching frequencies on average. Discrepancies in higher-frequency intramolecular modes will primarily impact the enthalpy and free energy via the zero-point vibrational energy. Close inspection of the pDOS in the low-frequency region also reveals discrepancies between the two models that will primarily impact the entropy as well as the temperature dependence of the enthalpy. In the region below 500 cm^{-1}, DFTB underestimates the DFT phonon frequencies by 22 cm^{-1} on average, or 26 cm^{-1} in mean absolute error.

Figure 3.4b shows how the pDOS is dramatically improved after shifting the DFTB phonon modes according to Eq 3.5 and correcting the acoustic modes. A few minor discrepancies do remain: for example, the shifted DFTB peaks near 500 cm^{-1} should be broader and less intense, while the opposite is true for several peaks in the ∼750–1750 cm^{-1} range.

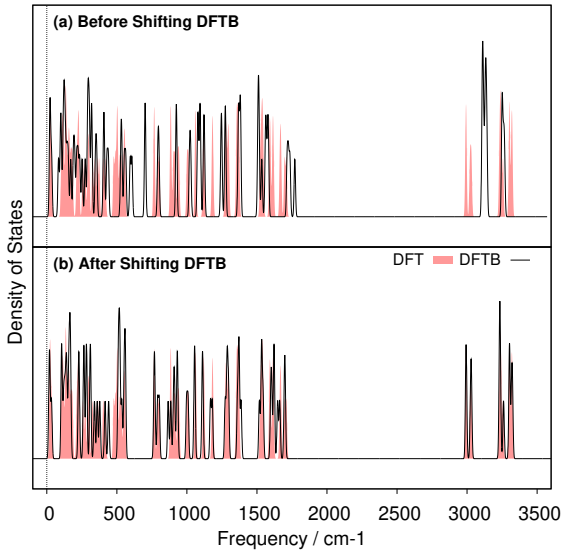

Figure 3.4: Comparison of the DFTB3-D3(BJ) phonon density of states for the α polymorph of oxalyl dihydrazide (a) before and (b) after the phonon shifting procedure against a supercell DFT (B86bPBE-XDM) calculation. The reference DFT pDOS is plotted in red, while the DFTB one is in black. All results except the unshifted DFTB pDOS in (a) include the corrected acoustic modes derived from DFT elastic constants.

Nevertheless, the shifted DFTB band positions and intensities as a whole exhibit far better agreement with the target DFT ones.

For more insight into the performance of the shifted DFT frequencies, Figure 3.5 plots the phonon frequencies for four modes in the 440–500 cm^{-1} range for acetic acid. It shows how the additive shift, which ranges from 10–25 cm^{-1} for these particular modes, brings the DFTB phonon frequencies into perfect agreement with DFT at the Γ-point. However, the level of agreement between the two models is moderately reduced elsewhere in the Brillouin zone due to differences in the dispersion predicted by the two models. Nevertheless, the shifted DFTB pDOS still mimics the target DFT one fairly well, and it represents a noticeable improvement over the original, unshifted DFTB pDOS.

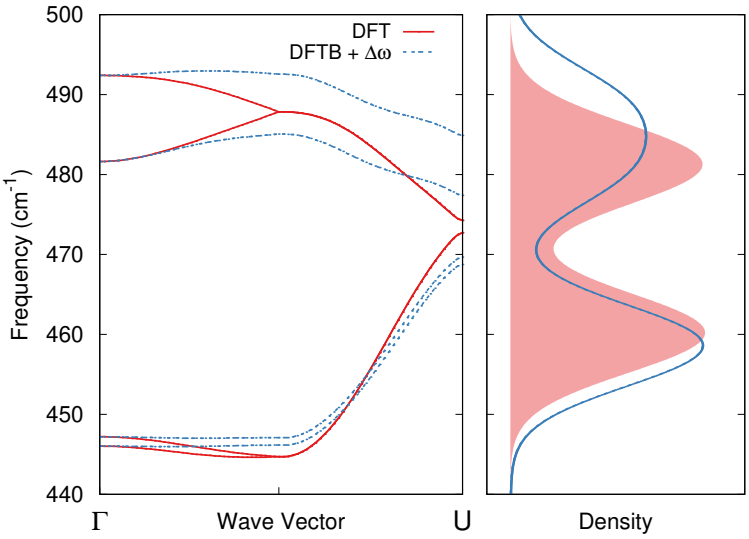

Figure 3.5: A narrow region of the acetic acid phonon band structure (left) and density of states (right) as evaluated by DFT and DFTB after frequency shifting.

Next, we compare the performance of the approximate strategies for computing the room-temperature Helmholtz vibrational free energy against the DFT results obtained for acetic acid. Figure 3.6 plots the errors in the vibrational free energy per molecule relative what one obtains with supercell DFT (including elastic constant treatment of the acoustic modes). DFT Γ-point frequencies underestimate the target vibrational free energy by 2.5 kJ/mol compared to the supercell result. Given that the net vibrational free energy contribution to polymorph energy differences is often 1–2 kJ/mol,[92,101] this error is potentially significant.

DFTB Γ-point frequencies perform even worse, underestimating the target vibrational free energy by 6.8 kJ/mol. Including phonon dispersion via a supercell DFTB calculation further reduces the error by about a third, to 4.4 kJ/mol. Once the DFT-derived phonon frequency shift (Eq 3.5) is applied, however, the free energy error drops to

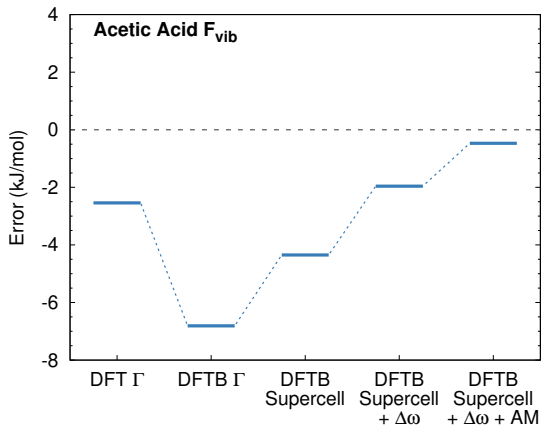

Figure 3.6: Errors in the room-temperature Helmholtz vibrational free energies per molecule ($F_{vib}(300K)$) computed with various approximate models relative to the full DFT supercell evaluation.

2.0 kJ/mol. Adding the appropriate acoustic modes (Eq 3.9) computed from the elastic constants brings the Helmholtz vibrational free energy to within 0.5 kJ/mol of the target supercell DFT treatment (which includes the same acoustic mode contributions).

Figure 3.7 plots the errors in the DFTB vibrational enthalpy, entropy (multiplied by temperature), and Helmholtz free energies for acetic acid as a function of temperature before and after applying the frequency shift and acoustic mode correction. Note that the pressure-volume work contribution to the enthalpy is negligible for a crystal at ambient pressure, which means that the Helmholtz and Gibbs free energies are essentially identical. Figure 3.7 highlights how the errors in the uncorrected DFTB model relative to the target DFT result vary considerably with temperature. For example, the errors in F_{vib} computed purely with DFTB range from -2.5 kJ/mol at 0 K to -4.3 kJ/mol at 300 K. The vibrational enthalpy error decreases with increasing temperature, from -2.5 kJ/mol to -1.8 kJ/mol, but this is more than compensated for by the growth of the error in the entropic contribution to

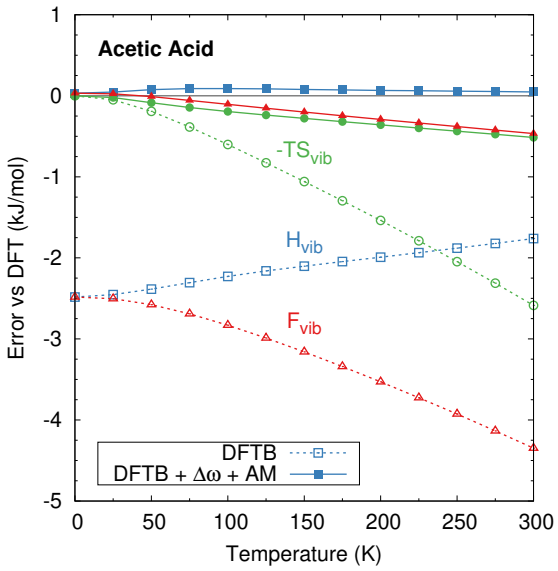

Figure 3.7: Temperature-dependence of the errors in the predicted enthalpy (blue), entropic (green), and free energy (red) energies for crystalline acetic acid. Errors are computed relative to supercell DFT with the acoustic mode correction. Dotted lines correspond to the raw DFTB results, while solid lines indicate DFTB after shifting the frequencies and applying the acoustic mode fix.

the free energy. In contrast, after shifting the phonon frequencies and correcting the acoustic modes, the errors become much smaller and vary by only half a kJ/mol between 0 K and room temperature. The largest error in F_{vib} is only 0.5 kJ/mol, a nine-fold reduction from the uncorrected value.

For further insight, Table 3.2 examines the predicted thermochemical properties for five different crystals: carbon dioxide, acetic acid, imidazole, the α polymorph of oxalyl dihydrazide, and acetaminophen form I. Benchmark supercell DFT phonon calculations with acoustic mode corrections were performed for the three smaller crystals. Supercell DFT phonon calculations were not performed for oxalyl dihydrazide and acetaminophen due to computational expense.

Table 3.2: Predicted vibrational thermochemical contributions (excluding the electronic energy) for several molecular crystals, in kJ/mol per molecule, as computed with supercell DFTB, frequency-shifted supercell DFTB, frequency-shifted supercell DFTB with corrected acoustic modes (AM), and supercell DFT with corrected acoustic modes.

	DFTB	DFTB $+\Delta\omega$	DFTB $+\Delta\omega$+AM	DFT + AM
Carbon Dioxide				
H_{vib}(0K)	30.4	32.4	32.5	32.0
H_{vib}(300K)	42.4	43.3	43.3	43.1
TS_{vib}(300K)	32.7	25.1	25.5	26.5
F_{vib}(300K)	9.5	17.5	17.8	16.5
Acetic Acid				
H_{vib}(0K)	160.7	163.2	163.2	163.2
H_{vib}(300K)	175.5	177.3	177.3	177.3
TS_{vib}(300K)	31.4	30.0	29.3	28.8
F_{vib}(300K)	144.1	147.3	148.0	148.4
Imidazole				
H_{vib}(0K)	186.3	186.2	186.2	186.2
H_{vib}(300K)	200.9	199.8	199.8	199.8
TS_{vib}(300K)	34.5	30.5	30.0	29.2
F_{vib}(300K)	166.3	169.2	169.7	170.6
α-Oxalyl Dihydrazide				
H_{vib}(0K)	274.7	285.0	285.0	–
H_{vib}(300K)	300.6	307.7	307.8	–
TS_{vib}(300K)	52.2	45.5	43.5	–
F_{vib}(300K)	248.4	262.2	264.3	–
Acetaminophen Form I				
H_{vib}(0K)	411.4	414.7	414.7	–
H_{vib}(300K)	442.0	444.3	444.3	–
TS_{vib}(300K)	64.9	60.4	60.2	–
F_{vib}(300K)	377.1	383.6	384.0	–

For the first three crystals which have benchmark supercell DFT results, uncorrected DFTB exhibits modest mean absolute errors (MAD) in the vibrational enthalpy of 1.4 kJ/mol at 0 K and 1.2 kJ/mol at 300 K. In contrast, the frequency-shifted DFT models (with or without corrected acoustic modes) perform far better for the enthalpies, with a MAD of 0.1 kJ/mol. This MAD reflects a 0.4 kJ/mol error for carbon dioxide and essentially zero error for the other two crystals. Because the enthalpy is dominated by the

zero-point contribution and exhibits modest temperature dependence, the frequency shift alone corrects most of the deficiencies of DFTB.

The vibrational entropy is more sensitive to the low-frequency phonon modes and shows greater variation across the different models. Raw DFTB performs poorly, with MAD of 4.7 kJ/mol in TS_{vib} at 300 K. This error reduces substantially to 1.3 kJ/mol upon shifting the frequencies and further down to 0.8 kJ/mol after correcting the acoustic modes. Because the errors for the two corrected DFTB models are dominated by the entropies, the errors in F_{vib} are similar. The final MAD error in the room-temperature free energies is 0.9 kJ/mol once the DFTB frequencies have been shifted and the acoustic modes corrected. Overall, the $\sim$1 kJ/mol errors in the absolute vibrational free energies represent a several-fold improvement over raw DFTB, and they are promising for organic crystal polymorphism problems for which some error cancellation often occurs when computing relative polymorph stabilities. The issue of error cancellation in relative polymorph free energies will be revisited below.

While benchmark DFT values were not obtained for oxalyl dihydrazide and acetaminophen, the data in Table 3.2 shows similar convergence behaviors of the different thermochemical quantities at the DFTB level. The frequency shift alters the DFTB enthalpies by up to 10 kJ/mol, while the acoustic mode correction has little impact. In contrast, both the frequency shift and acoustic mode corrections are important for the entropic contribution of oxalyl dihydrazide (and acetaminophen to a lesser extent). The final corrected free energies differ from the raw, uncorrected DFTB values by about 16 kJ/mol for oxalyl dihydrazide and 7 kJ/mol for acetaminophen. These errors are considerably

larger than those found for the smaller three molecules discussed earlier, suggesting that the proposed DFTB corrections may become increasingly large as molecular complexity increases.

Next, we apply the pDOS approximation approach to the five polymorphs of oxalyl dihydrazide. This system is representative of polymorph problems where one might be interested in understanding how free energy contributions alter the relative polymorph stabilities. Oxalyl dihydrazide has five known polymorphs at ambient pressure, which are denoted $\alpha, \beta, \gamma, \delta$, and ϵ.[142] Additional high-pressure forms have been reported, though they have not been fully characterized.[146] The five ambient-pressure forms differ in their hydrogen bonding networks, including differences in whether they form intra- or intermolecular hydrogen bonds. The β polymorph is metastable and hard to crystallize; it is believed to be the least stable polymorph. The γ form is the second least stable. The α, δ, and ϵ forms are more stable than the other two, though the precise stability ordering among those three is unclear. Oxalyl dihydrazide has become a notable test case for electronic structure models due to its difficulty.[65,96,147–149] The current consensus points to the following stability ordering (from most to least stable): $\alpha < \epsilon < \delta < \gamma < \beta$, and this ordering will be taken as the correct one here.

Figure 3.8 compares the relative oxalyl dihydrazide polymorph stabilities as computed from pure B86bPBE-XDM electronic lattice energies (U_{el}) and from several different Helmholtz vibrational free energy approximations. While the DFT electronic energy alone predicts the correct stability ordering, the 12 kJ/mol range is moderately larger than the 10 kJ/mol energy window that typically separates experimentally observed polymorphs.[92–94]

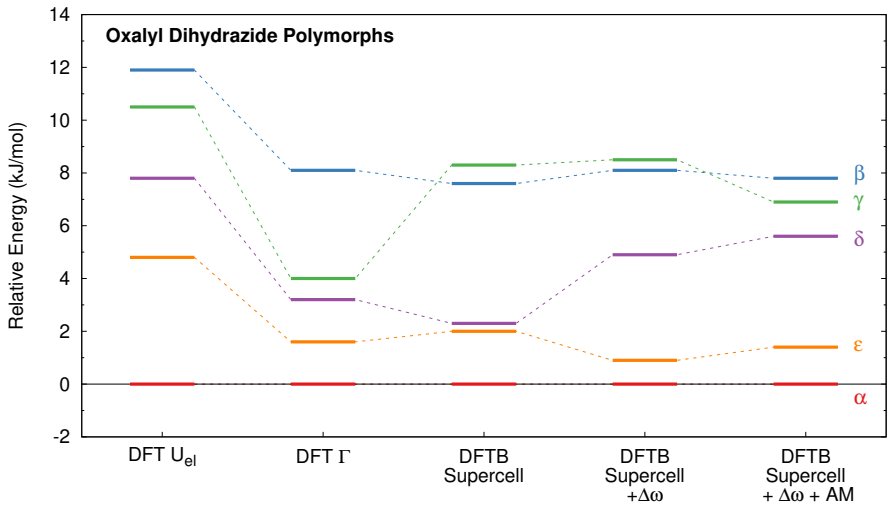

Figure 3.8: Relative stabilities of the five oxalyl dihydrazide polymorphs. The first column presents relative DFT electronic lattice energies, while the subsequent ones correspond to free energies as computed from Γ-point DFT frequencies, supercell DFTB, and supercell DFTB corrected with the frequency shift and acoustic modes.

The DFT Γ-point approximation to the free energy narrows this range somewhat, stabilizing the γ form most noticeably. Using the raw DFTB supercell phonon treatment alters the stabilities considerably, and it incorrectly suggests that the γ form is less stable than the β one. Not until both the Γ-point frequency shift and the acoustic mode correction are included do the free energies predict a stability ordering that is consistent with experiment. Without further experimental information, it is not possible to assess the quantitative accuracy of these stabilities, but it is reassuring to see that the proposed approximations for the phonon density of states does produce the qualitatively correct polymorph rankings in this difficult system.

It is also worth noting how the differences in the relative polymorph free energies vary by only a few kJ/mol between models, while the absolute F_{vib} values in for α oxalyl dihydrazide in Table 3.2 differ by 16 kJ/mol between the corrected and uncorrected DFTB

results. In other words, considerable error cancellation occurs in the relative polymorph free energies. Despite the error cancellation, the uncorrected DFTB results predict qualitatively incorrect relative free energies. This emphasizes the importance of the DFTB correction for capturing the small energy differences associated with polymorphism.

Finally, we examine the computational savings associated with the approximate pDOS treatment explored here. Table 3.3 summarizes the relative computational costs associated with evaluating the acetic acid pDOS. The 2×4×3 supercell used here contains 24 replicas of the crystallographic unit cell, for a total of 768 atoms. The cost of the DFTB supercell phonon calculation is about 19 times that of a DFT Γ-point one. On the other hand, that is far cheaper than the supercell DFT calculation, which costs 615 times that of the DFT Γ-point one. The fixed-cell geometry optimizations required to evaluate the elastic constants and acoustic modes have an effective cost of about three times the DFT Γ-point frequency calculation for this system. In other words, the additional calculations required to perform the pDOS correction comprise only a small fraction of the DFTB supercell phonon calculation. Combining the DFT Γ-point calculation, the DFTB supercell one, and acoustic mode correction brings the total computational cost to 22.9 times that of the DFT Γ-point alone. This is 27 times faster than the supercell DFT calculation (including the acoustic mode correction), with only 0.4 kJ/mol loss in accuracy in the vibrational free energy at room temperature (*cf* Table 3.2).

Table 3.3: Computational cost associated with computing the different phonon density of states approximations for acetic acid, computed relative to the cost of a DFT Γ-point frequency evaluation. The relative costs were derived from processor hours, rather than wall time.

Model	Relative Cost
DFT Γ	1.0
DFTB Γ	0.02
DFTB Supercell	18.6
Shifted DFTB Supercell	19.6
Shifted DFTB Supercell + Acoustic Modes	22.9
DFT Supercell	614.6
DFT Supercell + Acoustic Modes	617.8

3.5 Conclusions

Despite its computational efficiency advantages, the phonon density of states computed from DFTB3-D3(BJ) with the 3ob-3-1 parameterization exhibits appreciable errors relative to a DFT GGA treatment. In the systems examined here, these discrepancies introduce errors ranging from a few kJ/mol to more than ten kJ/mol. Even with the error cancellations that can occur in relative energies, it seems likely that thermochemical properties predicted from this DFTB model will be unable to provide the kJ/mol accuracy often required for problems in organic polymorphism and crystal structure prediction.

This study demonstrated how a simple additive shift to the DFTB phonon frequencies and careful treatment of the acoustic modes leads to a model that performs far better with only moderate increase in computational cost. Unsurprisingly, the biggest improvements from the corrections manifest in the entropic contribution to the free energy, since that term is particularly sensitive to the low-frequency phonon modes. However, sizable corrections were found for the absolute vibrational enthalpies as well, arising primarily from the zero-point contribution.

The correction proposed in this study is independent from the particular DFTB approximation or density functional used here. The same ideas could be applied to any pair of "high" and "low" level models. Improvements to existing DFTB models and parameterizations that are actively being pursued by the community could be useful in this context, including extensions to hybrid and/or range-separated functionals and better descriptions of non-covalent interactions.[81] Alternatively, semi-empirical composite models have found success in non-covalent interactions and certain aspects of crystal structure prediction[131,133,150–152] and could potentially be suitable here too. The most important criteria in selecting the appropriate pair of models will be the accuracy of the high-level method, the computational cost of the two methods, and the fidelity with which the low-level method reproduces the shapes of the phonon dispersion curves. In the future, it will be interesting to employ this approach more widely. Beyond basic harmonic free energy contributions, the approach could readily be combined with quasi-harmonic calculations of phase diagrams, spectroscopic properties, mechanical properties, etc.

Chapter 4

Solid-state Phase Diagrams and Thermal Expansion

The ability to predict not only what organic crystal structures might occur, but also the thermodynamic conditions under which they are the most stable would be extremely useful for discovering and designing new organic materials. The present study takes a step in that direction by predicting the temperature- and pressure-dependent phase boundary between the α and β polymorphs of resorcinol using density functional theory (DFT) and the quasi-harmonic approximation. To circumvent the major computational bottleneck associated with computing a well-converged phonon density of states via the supercell approach, a recently developed approximation is employed which combines a supercell phonon density of states from dispersion-corrected third-order density functional tight binding (DFTB3-D3(BJ)) with frequency corrections derived from a smaller B86bPBE-XDM functional DFT phonon calculation on the crystallographic unit cell. This mixed

DFT/DFTB quasi-harmonic approach predicts the lattice constants and unit cell volumes to within 1–2% at lower pressures. It predicts the thermodynamic phase boundary in almost perfect agreement with the experiment, though this excellent agreement does reflect fortuitous cancellation of errors between the enthalpy and entropy of transition.

4.1 Introduction

Organic molecular crystal structure prediction (CSP) has progressed dramatically in recent years, including many successful "blind" predictions.[29,30,63,97,98,153–155] CSP is increasingly being employed to understand pharmaceutical solid form landscapes,[156–164] for example. While polymorph stability rankings of experimentally known structures are often predicted with reasonable accuracy, one of the long-standing challenges of CSP lies in understanding why crystal energy landscapes frequently include far more putative structures than have been observed experimentally.[165] In some cases, McCrone's remark[166] that the number of crystal structures known for a compound is proportional to the time and money spent searching for them seems to hold true. Nevertheless, the number of predicted structures greatly exceeds the number of experimentally known ones even for prolific polymorph formers like ROY (5-methyl-2-[(2-nitrophenyl)-amino]-3-thiophenecarbonitrile),[167,168] galunisertib,[162] and axitinib.[169]

One partial explanation for this failure to observe predicted polymorphs lies in the idea that researchers simply have not yet provided the correct crystallization conditions for these forms. Kinetics plays an important role in the phenomenon of polymorphism, as exemplified by the recent reports of two new ROY polymorphs which were discovered

via non-traditional crystallization techniques.[170,171] Unfavorable kinetics has also been invoked to explain why the predicted "global minimum" polymorph of galunisertib has not been found experimentally despite years of effort,[162] though recent work has also argued that the high stability of that polymorph may be an artifact of density functional theory.[66]

In 2018, Price described current-generation crystal structure prediction approaches that search for the global lattice energy minimum structure as "zeroth-order" CSP.[172] The next generation "thermodynamic" CSP would rank structures based on free energy as a function of temperature and pressure, as well as on crystal size, solvent, and the presence of heterogeneous templates or impurities. The free energy landscape can differ considerably from the lattice energy one due to factors such as the phonon contributions or dynamic behaviors that cause multiple lattice energy minima to coalesce[116,173,174] into a single free energy basin. Overall, thermodynamic CSP represents a greater challenge for computational chemistry: moving beyond predicting what polymorphs might form to predicting the experimental conditions under which they will be most likely to form. This has been realized already in select cases. For the drug candidate Dalcetrapib, for example, CSP prediction of a stable, densely packed polymorph led to a subsequent successful high-pressure crystallization of that form.[159]

Aiming toward the goal of predicting polymorph stability as a function of temperature and pressure, the present work focuses on predicting the structures, thermochemical properties, and thermodynamic phase boundary between two polymorphs of resorcinol. Predicting phase transition temperatures is particularly difficult for several reasons. Beyond the fundamental challenge of predicting accurate lattice energies, one must also compute phonon

contributions to the free energy. Vibrational contributions also typically induce thermal expansion of the crystal lattice, and accounting for how the resulting anharmonicities impact free energies (e.g. via the quasi-harmonic approximation[48,49,106]) can be critical to predicting even qualitatively correct phase boundaries.[51] Further treatments of anharmonicity and/or quantum effects can also be considered.[114,115,117,120,173,175–181] Uncertainty analysis indicates how the predicted thermal phase transition temperatures can exhibit strong sensitivity to small errors.[182] In particular, the more parallel the free energy curves are for different phases, the greater the impact of small errors on the predicted phase boundary. High-pressure phase boundaries can be moderately easier to predict, since thermal expansion is reduced and packing density becomes a major factor in determining the enthalpy at high pressures.

Despite these challenges, there have been a number of successful predictions of phase boundaries in systems such as carbon dioxide,[183–188] ice,[189,190] nitrogen,[191–196] methanol,[51] benzene,[115,173,176,197] and others.[96,114] In methanol, for example, fragment-based calculations at the coupled-cluster singles, doubles, and perturbative triples (CCSD(T)) level coupled with the quasi-harmonic approximation predicted the phase diagram of the α, β, and γ to within $\sim$0.5 kJ/mol accuracy over a range of several hundred Kelvin and a few GPa.[51]

Unfortunately, that coupled cluster theory prediction of the methanol phase diagram required a few hundred thousand central processing unit hours,[51] and applying the same techniques to pharmaceutical-sized molecules would be infeasible. Density functional theory is considerably less computationally demanding, though it can still be expensive due

to the high-cost of computing harmonic phonons with DFT. Instead, the current study utilizes a quasi-harmonic model that combines density functional theory (DFT) treatment of the lattice energies and a recently developed approach[198] for obtaining the phonon density of states from a mixture of DFT and density functional tight binding (DFTB). In particular, the high computational cost of the phonon calculation is exacerbated by the need for large supercells to obtain well-converged phonon densities of states. The new approach first computes the phonon density of states in a large supercell with DFTB at relatively low cost, and then shifts the individual phonon bands based on the difference between DFT and DFTB frequencies in a smaller crystallographic unit cell. This ensures DFT-quality phonon modes at the Γ point, while the phonon dispersion is modeled with DFTB.

A number of earlier studies have found dispersion-corrected DFTB3 models to be useful in molecular crystal applications,[132,133,199] including for embedding models,[130] intermediate screening steps in crystal structure prediction[127,129] and for quasi-harmonic calculations.[128] This evidence suggests that the same DFTB3 models may be suitable for the present phonon approximation as well. In testing on a few simple crystals using dispersion-corrected, third-order DFTB3-D3(BJ) and the B86bPBE-XDM density functional,[198] the approximation introduced $\sim$1 kJ/mol errors or less into the total Gibbs free energies compared to the DFT ones. Additional error cancellation occurred in the relative energy differences between different crystal polymorphs. At the same time, the mixed DFT/DFTB approach reduced the computational effort required for evaluating the phonon density of states by 1–2 orders of magnitude compared to a more conventional approach based purely on DFT.

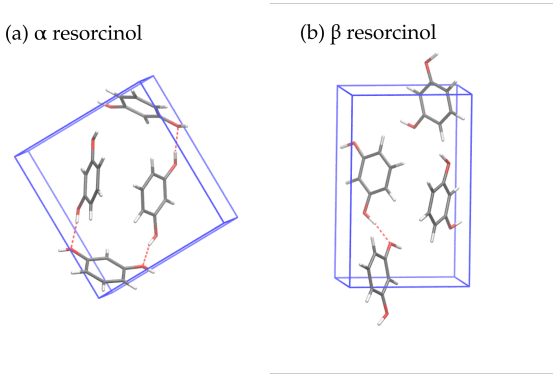

Figure 4.1: The crystal structures of α and β resorcinol differ in the hydroxyl group orientations and their intermolecular hydrogen bond networks.

The present study extends that earlier research by combining this phonon density of states approximation with the quasi-harmonic approximation and then modeling the crystal structures and phase transition of the α and β polymorphs of resorcinol at finite temperatures and pressures. Resorcinol, also known as benzene-1,3-diol, has been studied for many decades and is used in the synthesis of resins and pharmaceuticals. Crystalline resorcinol can occur in several known polymorph phases. The α and β phases adopt the same $Pna2_1$ space group, though they differ in their intramolecular conformations and intermolecular hydrogen bonding patterns (Figure 4.1).[2]

The α polymorph is the thermodynamically preferred form at ambient conditions, even though it is less dense than the β phase (i.e. contrary to the density rule.[200]). The α phase converts to the β polymorph upon heating to ∼360–370 K, or at room temperature upon compression at ∼0.4–0.5 GPa.[1–3] The transition temperature and pressure depend strongly both on the rate of heating and the rate of pressurization, implying that kinetics plays a role in the phase transition.[1,201–203] The experimental phase observations used

here result from careful measurements which attempted to control for these kinetic factors through sample equilibration and by using slower heating and pressurization rates.[1,201]

Three other phases of resorcinol are not considered here. The disordered γ polymorph and the ordered δ one form at several GPa of pressure, though neither crystal structure has been solved.[1,202,203] In 2016, the structure of a new ϵ polymorph was reported at atmospheric conditions through a combination of experimental powder x-ray diffraction and crystal structure prediction, and there was even some evidence of another (as yet unconfirmed) $P2_1$ phase.[204] However, this ϵ polymorph is believed to be metastable relative to the α and β phases at all temperatures, so it is not considered here either. The next section describes the approximation used for the phonon density of states and its incorporation into the quasi-harmonic approximation.

4.2 Theory

4.2.1 Gibbs Free Energies

The thermodynamic stability of a crystal at a given temperature and pressure is governed by the Gibbs free energy,

$$G(T,P) = U_{el} + F_{vib}(T) + PV \tag{4.1}$$

where U_{el} is the electronic energy, $F_{vib}(T)$ is the Helmholtz vibrational free energy, and PV represents the pressure-volume contribution. The electronic energies here will be computed with DFT using periodic boundary conditions. Within the harmonic approximation, the

Helmholtz vibrational free energy is computed as,

$$F_{vib}(T) = 3nN_a k_B T \int_0^\infty \ln\left[2\sinh\left(\frac{\hbar\omega}{2k_B T}\right)\right] g(\omega) d\omega \tag{4.2}$$

where n is the number of atoms in the crystallographic unit cell, N_a is Avogadro's number, $\hbar$ is Plank's constant, k_b is the Boltzmann constant, T is the temperature, and $g(\omega)$ is the phonon density of states (DOS) as a function of frequency ω.[45]

4.2.2 Efficient approximation for the phonon density of states

Because evaluation of the harmonic phonon DOS often forms the major computational bottleneck in computing the free energy, approximations that reduce the cost of the phonon DOS can be very helpful. One of the simpler phonon DOS approximations is to evaluate only the zone-center (Γ-point) phonons. However, this approximation neglects contributions arising from dispersion of the optical phonon modes throughout reciprocal space and the non-zero frequencies of the acoustic modes away from the Γ point. Acoustic modes contribute significantly to the entropy and to the temperature dependence of the enthalpy. They can be important when predicting thermodynamic phase boundaries, where even small errors in the free energy can shift the transition temperature by a hundred degrees Kelvin or more. These contributions away from the Γ point are generally expected to be most important in smaller unit cells for which the Γ-point phonon DOS is less-well converged, and in cases where the unit cell shapes differ considerably between polymorphs, thereby hindering error cancellation in the thermochemical energy differences.

Phonon contributions away from the Γ point can be captured by performing a supercell lattice dynamics calculation[49,82,135] or using density functional perturbation theory.[121] Unfortunately, the need for large supercells extending ∼10–15 Å or more in each direction to converge the phonon density of states[119,120,135] makes the supercell approach far more expensive than a simple harmonic phonon calculation on the crystallographic unit cell. To address this computational bottleneck, we recently proposed a strategy[198] for approximating the phonon density of states which reduces the computational cost by ∼1–2 orders of magnitude while introducing only small errors into the resulting free energies. This approach first performs the lattice dynamics calculation in a large supercell using density functional tight binding (DFTB) to capture the optical mode phonon dispersion. However, individual DFTB phonon bands will often be shifted considerably in frequency from the DFT values due to the limitations of the DFTB model, which leads to substantial errors in the resulting free energies. To improve the DFTB phonon DOS, the harmonic phonons are computed at the Γ point using DFT. This DFT unit cell calculation is typically far less computationally demanding than a large DFT supercell calculation would be. Each DFTB normal mode is then assigned to the corresponding DFT mode based on overlap of the normal mode eigenvectors, and an additive shift is applied to the frequencies of each DFTB phonon band based on the difference between the DFT and DFTB frequencies at the Γ point. The normal mode matching is similar to how eigenvector overlaps can be used to identify common normal modes in a crystal structure at multiple different volumes, for example.[205] Previous testing in other crystals[198] and for resorcinol here suggests that the mode assignments based on maximal overlaps are generally straightforward. After re-

ordering the phonon modes based on the matched pairs, the overlap matrix becomes highly diagonally dominant, and virtually all of the diagonal overlap elements between the DFT and DFTB normal mode eigenvectors exceed 0.5 (and they are often closer to unity).

This phonon mode matching procedure ensures that the Γ-point phonon values match DFT, while the phonon dispersion away from the Γ point is modeled by DFTB. Because this shift is not applicable to the three acoustic modes (their frequencies are always zero at the Γ point), the acoustic mode frequencies are computed from DFT elastic constants using the theory of elasticity.[206] Finally, the phonon density of states is constructed using a kernel density estimation (KDE) in which a 5 cm^{-1} wide normal distribution is placed at the frequencies from each discretely sampled k-point. This KDE approach improves the convergence of thermal properties with respect to reciprocal space sampling.[206] In small-molecule crystal benchmarks, this phonon DOS approximation approach introduced errors of ∼1 kJ/mol or less into the total free energies compared to supercell DFT results. Further error cancellation appears to occur for the relative free energies between crystal forms. See ref 198 for further details.

To help visualize this approximation, Figure 4.2 plots a sample phonon DOS for α-resorcinol before and after applying the frequency shift. These phonon densities of states use the DFTB3-D3(BJ) model and the generalized gradient approximation (GGA) functional B86bPBE-XDM that will be described in the Computational Methods section below. As seen here, the correction shifts the phonon modes considerably. The most substantial changes occur in the intramolecular stretching region above ∼1000 cm^{-1}. Some of the C-H stretching modes shift by hundreds of cm^{-1}. However, there are also many less visi-

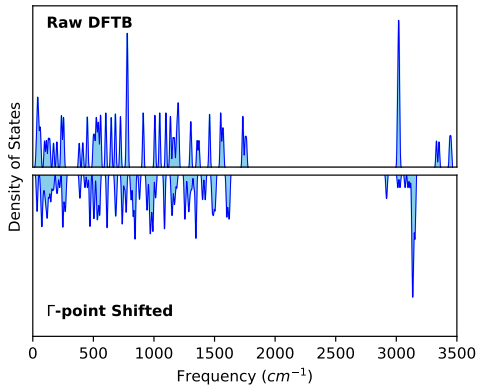

Figure 4.2: Comparison of the DFTB3-D3(BJ) phonon density of states for α resorcinol before and after applying the B86bPBE-XDM DFT Γ-point frequency shift.

ble changes to the density distribution in the lower-frequency region. Overall, the average magnitude of the frequency shift is 78 cm^{-1}, and these changes impact the thermochemistry considerably. The zero-point enthalpy increases by 2.4 kJ/mol per molecule, though the shift in the thermal enthalpic contributions exhibits the opposite sign, and the total enthalpy shift at 300 K is only 0.9 kJ/mol. The impact on the entropies is even larger. The frequency shift reduces the entropy by 17.1 J/(mol K) at room temperature, which reduces the entropic contribution TS to the free energy by 5.1 kJ/mol. The final free energy is shifted by 6.1 kJ/mol. Similar magnitude shifts occur for the β polymorph as well, leading to partial cancellation of these corrections in the relative polymorph energy difference. Nevertheless, these results highlight the significant impact of applying the Γ-point shift to the DFTB phonons. Finally, we note that this phonon DOS approximation is not restricted to particular DFTB or GGA functional models used here; any combination of a computationally inexpensive model with a more expensive, higher-accuracy model could be used. As will be demonstrated in the Results and Discussion, the chosen combination

works fairly well for resorcinol, but it is possible that the results could be improved further with alternative model choices.

4.2.3 Quasi-harmonic approximation

Anharmonic contributions can also contribute appreciably to the predicted thermochemical energies. The quasi-harmonic approximation (QHA) represents one of the simplest approaches for incorporating some anharmonicity into the harmonic phonon treatment. It typically works fairly well for molecular crystals up to moderately high temperatures below the melting point.[48,49] The QHA maps how the phonon frequencies and free energies vary with the molar volume of the crystal. In the implementation here, the electronic energy U_{el} is first computed as a function of volume by applying a series of positive and negative external isotropic pressures to the cell and relaxing the lattice parameters and atomic positions. This allows the unit cell to relax anisotropically, softens the one-dimensional potential energy curve compared to isotropic scaling of the lattice constants, and leads to improved description of the expansion/contraction.[50,51]

Next, the phonon density of states and free energies are evaluated at the equilibrium geometry and at several expanded and contracted volumes from the $U_{el}(V)$ curve. Each explicit phonon DOS evaluation was performed using the mixed DFT/DFTB approach described in Section 4.2.2, and care was taken to ensure the phonon DOS calculations were performed across the range of volumes associated with the temperatures and pressures of interest. After computing $F_{vib}(T)$ for each sampled structure at a chosen temperature, the F_{vib} values as a function of volume were fitted to a second-order polynomial. This F_{vib} fitting procedure appears to work well (e.g. see Figure 4.3b and Refs 51, 108, 113, 122, though

one could alternatively fit the individual phonon frequencies as a function of volume.[128] Summing $U_{el}(V)$, $F_{vib}(V)$, and PV for the given temperature and pressure produces $G(V)$. This free energy is fitted to a double-Murnaghan equation of state, in which the compression and expansion branches are fitted separately to the Murnaghan equation of state,[52]

$$G(V) = G_0 + \frac{B_0 V}{B_0'}\left[\frac{(V_0/V)^{B_0'}}{B_0' - 1} + 1\right] - \frac{B_0 V_0}{B_0' - 1} \tag{4.3}$$

and the two halves connect smoothly at the equilibrium volume V_0. From the fit, one obtains the optimal molar volume V_0, free energy at that volume G_0, the bulk modulus B_0, and the first derivative of the bulk modulus with respect to pressure, B_0'. The double-Murnaghan form was chosen based on a prior study of crystalline methanol which found it reproduced the ab initio free energy data more accurately than several other common functional forms.[50] Figure 4.3 plots sample electronic energy, Helmholtz vibrational free energy, and combined Gibbs free energies versus volume for the two resorcinol polymorphs at room temperature and ambient pressure.

The computational bottleneck lies in computing the electronic energy curve and phonons. The subsequent steps described here to determine the optimal structure at a particular temperature and pressure require minimal computational cost, which allows one to map out $G(T, P)$ readily. Lattice parameters and atomic coordinates for the current volume are interpolated from the values explicitly obtained in the geometry optimizations used to generate $U_{el}(V)$.

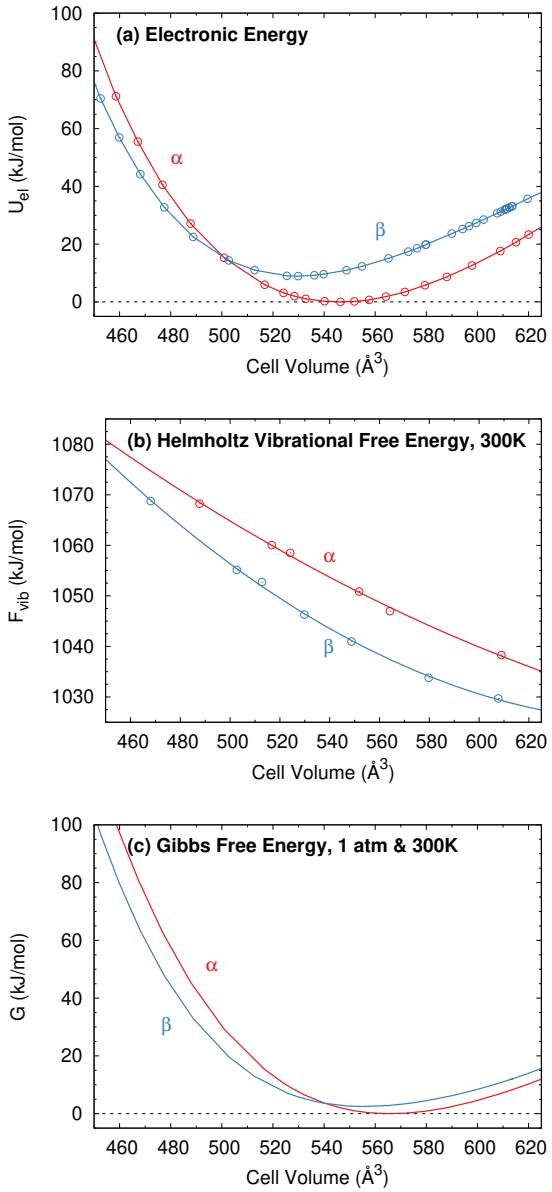

Figure 4.3: The quasi-harmonic treatment of resorcinol combines (a) electronic DFT energies and (b) Helmholtz vibrational free energies as a function of volume, which are then summed along with the PV term to obtain the Gibbs free energy. The predicted structures for the given thermodynamic conditions correspond to the minima of the $G(V)$ curves. Data shown here for 300 K and 1 atm.

The specific form of the quasi-harmonic approximation used here does make some approximations. The thermal expansion is mapped onto a one-dimensional quasi-anisotropic dependence on volume. Moreover, the atomic positions at each given volume/pressure are optimized based on the electronic lattice energy, rather than the free energy. As a result, contributions from zero-point vibrational energy and the ansiotropy of the thermal expansion are only partially captured. Nevertheless, approaches similar to the one used here have proved successful in many applications.[49–51,98,103,105–108,113,120,122,205] Moreover, Abraham and Shirts studied different quasi-harmonic approximations for predicting thermal expansion and polymorph free energies in organic molecular crystals, including for the α and β polymorphs of resorcinol. At room temperature, they found an approach similar to the one used here differed from more complete quasi-harmonic approximation models by no more than 0.5% in lattice parameters and ∼0.1 kJ/mol in the free energy difference between the two polymorphs. That will not always be true: they found less faithful performance for an approximation like the one used here when studying two polymorphs of piracetam, however, and further work is needed to ascertain more clearly when more elaborate treatments such as those found in Refs 175 and 207 will be required.

4.3 Computational Methods

4.3.1 DFT Structure optimizations

Experimental crystal structures for α- (RESORA03[208]) and β-resorcinol (RESORA08[209]) at ambient pressure were taken from the Cambridge Structure Database (CSD). The experimental α structure was solved at 120 K, while the β-form one was determined

at room temperature. The atomic positions and lattice parameters for each structure were fully relaxed to their electronic energy minima using planewave DFT. The electronic energy surface U_{el} was mapped out over 37 volumes spanning 408–720 Å^3 for α, and 39 volumes spanning 408–638 Å^3 for β, through a series of additional structure relaxations subjected to positive and negative external isotropic pressures. Similar equation of state fits could likely have been obtained with significantly fewer energy-volume data points as well.

These periodic DFT calculations were performed in Quantum Espresso v6.1[210] using the B86bPBE density functional[78,211] and the exchange-hole dipole method (XDM) dispersion correction.[77] This functional has performed well in many earlier molecular crystal studies.[63,77,97,143] Core electrons were treated according to the projector augmented wave (PAW) approach, and PAW potentials for H, C, and O were produced using A. Dal Corso's Atomic code v6.1.[76] Optimizations were carried out using a 50 Ry planewave energy cutoff. Reciprocal space k-points were placed on a $1\times1\times3$ Monkhorst-Pack grid[212] for $\alpha-$resorcinol and on a $3\times1\times3$ grid for $\beta-$resorcinol.

4.3.2 Phonon density of states and free energies

DFT and DFTB3-D3(BJ) harmonic vibrational frequencies were computed using the finite displacement method as implemented in Phonopy v2.4.2.[82] DFT Γ point phonons were evaluated using the same B86bPBE-XDM density functional, k-point grid, and plane wave cutoff as described in the optimization procedure.

To ensure stationarity of the DFTB potential energy, the atomic positions in the unit cells were subsequently optimized with DFTB3-D3(BJ) prior to supercell expansion using the DFTB+ software, version 19.1.[80,81] The DFTB3-D3(BJ) calculations employed the

3ob-3-1 Slater-Koster parameterization,[136] which has shown good performance for organic species,[124] and Grimme's D3 dispersion correction.[79] All other DFTB job parameters employ the default values recommended in the DFTB+ documentation. The optimized DFTB structures were expanded to $3 \times 3 \times 4$ supercells for both structures. For the equilibrium structures, this corresponds to a minimum supercell dimension of 31 Å $\times$ 28 Å $\times$ 22 Å for α and 23 Å $\times$ 38 Å $\times$ 21 Å for β, each consisting of 2,016 atoms. Similar results could probably been obtained with smaller supercells, but these large cells were chosen to ensure good convergence of the phonon DOS, and they were affordable with DFTB3-D3(BJ). Finally, the Helmholtz vibrational free energies were computed from the phonon DOS via numerical integration of Eq 5.5. The quasi-harmonic approximation calculations and phase-diagram predictions were managed via an in-house python script, which is available on GitHub at https://github.com/cjcook41/Modematching. Inelastic neutron scattering spectra were simulated using the OCLIMAX program, version 3.0.[213]

For perspective on the computational timings, optimizing the α polymorph geometry from the experimental structure required 90 central processing unit (CPU) core hours on an Intel Xeon E5-2680v3 processor. Computing the Γ-point phonons and the elastic constants for a single structure (56-atom unit cell) required 139 and 446 CPU core hours, respectively. Finally, the DFTB phonon frequency calculation on the 2,016-atom supercell required 8,260 core hours.

Table 4.1: Comparison of predicted and experimental lattice parameters for the α and β polymorphs of resorcinol. The quasi-harmonic approximation is employed for the finite-temperature predictions, while the "no QHA" results utilize lattice energy minimization without any phonon contributions.

	Temperature	a (Å)	b (Å)	c (Å)	Cell Volume (Å^3)
		α-Resorcinol			
B86bBPBE-XDM	no QHA	10.37	9.32	5.58	539.91
B86bBPBE-XDM	120 K	10.45	9.40	5.65	554.27
Experiment[208]	120 K	10.47	9.41	5.67	557.95
		β-Resorcinol			
B86bBPBE-XDM	no QHA	7.77	12.51	5.35	520.82
B86bBPBE-XDM	4 K	7.88	12.49	5.46	537.52
Experiment[209]	4 K	7.81	12.62	5.43	534.69
B86bBPBE-XDM	300 K	8.00	12.47	5.58	556.55
Experiment[209]	300 K	7.93	12.61	5.51	551.19

4.4 Results and Discussion

4.4.1 Assessment of thermal expansion

First, we investigate the quality of the predicted unit cell volumes for both polymorphs relative to experiment at ambient pressure. Table 4.1 shows the predicted and experimental lattice parameters and unit cell volumes at select temperatures for α- and β-resorcinol. The optimized B86bPBE-XDM lattice parameters obtained from pure lattice energy minimization (i.e. without employing the quasi-harmonic approximation) are also included for comparison with the QHA results.

The QHA thermal expansion of the unit cell proves key to the accurate prediction of the experimental lattice parameters at all temperatures considered. Predicted cell volumes and lattice parameters for α-resorcinol are in excellent agreement with experiment.[208] Inclusion of the zero-point vibrational contribution and heating to 120 K causes a 2.7% vol-

ume expansion in α resorcinol. At 120 K, the QHA cell volume is only 0.7% smaller than the experimental volume, whereas the purely electronic DFT structure without QHA phonon contributions underestimates the volume by 3.2%. The 120 K QHA lattice constants are also exhibit excellent agreement with those determined experimentally, with errors of 0.02 Å or less.

In β-resorcinol, even at extremely low temperatures (4 K), QHA expansion leads to a 3.2% increase in volume with respect to the electronic minimum. This expansion again improves agreement with the experimental volume at 4 K, reducing the error from 2.6% too small without the QHA to only 0.5% too large with the QHA. This low temperature expansion primarily originates from the zero-point vibrational energy contributions, as the thermal population of the density of states is quite low. At room temperature, further expansion in the experimental cell means that the electronic energy minimum (no QHA) structures are 5.5% too small in volume, while the QHA treatment overestimates the volume by only 0.8%. In other words, the QHA treatment mildly exaggerates the expansion that occurs over the 0–300 K temperature range in this system.

The errors in the individual lattice parameters are somewhat larger for β-resorcinol than they were for the α polymorph, though they still exhibit reasonable agreement with experiment. The a and c lattice constants are over-estimated by 0.07 Å and 0.03–0.06 Å, respectively, while b is under-predicted by 0.13–0.14 Å. The opposing signs of these errors leads to some error cancellation that leads to the excellent predicted cell volumes. The QHA model does correctly predict the slight contraction of the b lattice constant with increasing temperature seen in the experiments. This contraction of b and coupled with

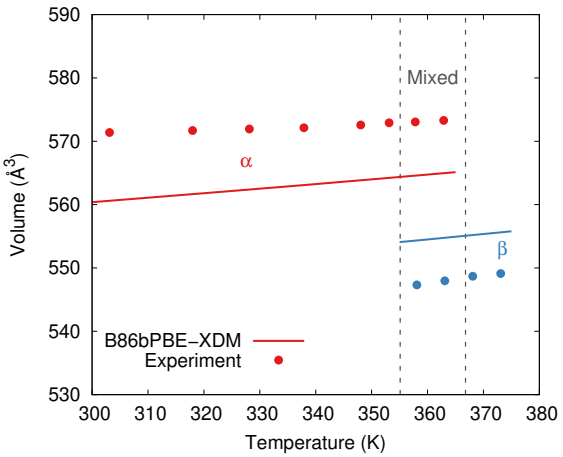

Figure 4.4: Comparison of the experimentally reported unit cell volumes (points) for α-(red) and β-resorcinol (blue) at 0.09 GPA against those predicted from the quasi-harmonic B86bPBE-XDM calculations (lines). The vertical lines indicate the temperature regimes under which pure α, pure β, or a mixture of the two phases was observed experimentally.

expansion of a and c also highlights the importance of allowing anisotropic relaxation of the cell constructing the initial $E(V)$ curves used in the QHA.[214]

Second, Figure 4.4 compares the predicted thermal expansion of both polymorphs relative to experiment at 0.09 GPa.[1] The quasi-harmonic B86bPBE-XDM calculations underestimate the unit cell volume of α-resorcinol by about 1.5–2% throughout the temperature range shown, while the β form volumes are overestimated by 1.2% on average. These errors are reasonably consistent with the results in Table 4.1, especially when considering that the α polymorph results are above room temperature here, compared to 120 K in Table 4.1. This level of agreement between theory and experiment is also consistent with the errors found for quasi-harmonic modeling in previous studies.[50,98,103–106,109,112,215,216] The quasi-harmonic model also reproduces the slope of the volume expansion with temperature for both polymorphs fairly well in this temperature range. The opposite signs of the errors

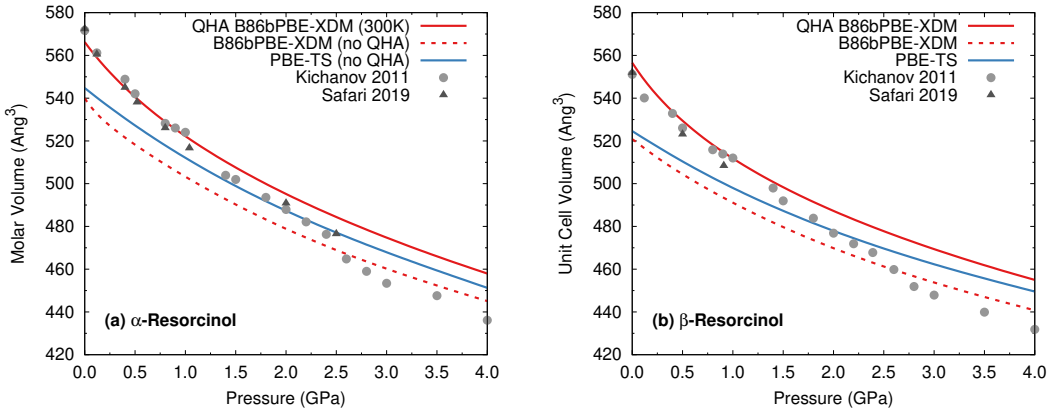

Figure 4.5: Comparison of predicted (lines) and experimental (points)[1,2] volumes of (a) α and (b) β resorcinol as a function of pressure. The quasi-harmonic approximation (QHA) B86bPBE-XDM predictions at room-temperature agree best with experiment at low pressure, while the B86bPBE-XDM and PBE-TS[3] models without quasi-harmonic thermal expansion underestimate the volume at low pressures. All models overestimate the volumes to some extent at higher pressures.

between the two phases does mean that the predicted volume difference between the two phases is only about half the experimental difference, however.

Next we investigate the quality of the predicted room-temperature unit cells as a function of pressure. Figure 4.5 compares the predicted volumes for both polymorphs from 0 to 4 GPa against experimental data from Ref 1 and 2. The reported volumes from the two experimental studies are in generally good agreement. The plot also includes data from previous PBE-TS calculations from Ref 3 which did not employ the quasi-harmonic approximation. For that reason, Figure 4.5 shows B86bPBE-XDM data with and without quasi-harmonic thermal expansion. Without thermal expansion, the PBE-TS and B86bPBE-XDM volumes are very similar at low pressure for both phases, though PBE-TS predicts volumes that are consistently $\sim$5–10 Å^3 larger than the B86bPBE-XDM ones. Both underestimate the experimental unit cell volume considerably below 1 GPa.

Upon applying the quasi-harmonic approximation with B86bPBE-XDM, the predicted unit cell volume expands by ∼3–5% for α and ∼3–7% for β, leading to much improved agreement with experiment at pressures in the ∼0–1 GPa range. As usual, thermal expansion occurs to a greater extent at lower pressures. Interestingly, all three computational models predict the resorcinol crystals to be considerably less compressible at higher pressures than the experiments, which leads to the cell volumes being considerably too large by 4 GPa. The reasons behind this discrepancy are unclear, but the fact that it occurs for all three models suggests that it is not due either to the specific generalized gradient approximation (GGA) density functionals used or to the inclusion/exclusion of phonon contributions. Regardless, the accuracy of the predicted volumes below 1 GPa is promising for predicting the phase transition in that regime.

Good agreement between the QHA B86bPBE-XDM model and experiment[2] is also seen in the pressure dependence of the lattice constants, as shown in Figure 4.6. For the α polymorph, the largest mean absolute error of 1.1% occurs for b, while a and c exhibit errors of only 0.2% and 0.5%, respectively. For β-resorcinol, the mean absolute errors are moderately larger at 1.3% for a, 0.9% for b, and 0.6% for c, but these still represent overall good agreement with experiment.

4.4.2 Phase diagram and thermochemical properties

Having seen that the model reproduces the experimental crystal structures well at lower pressures, we now investigate the thermodynamic phase-transition boundary in the 0 to 1 GPa regime. The experimentally observed phase behaviors depend on sample purity,

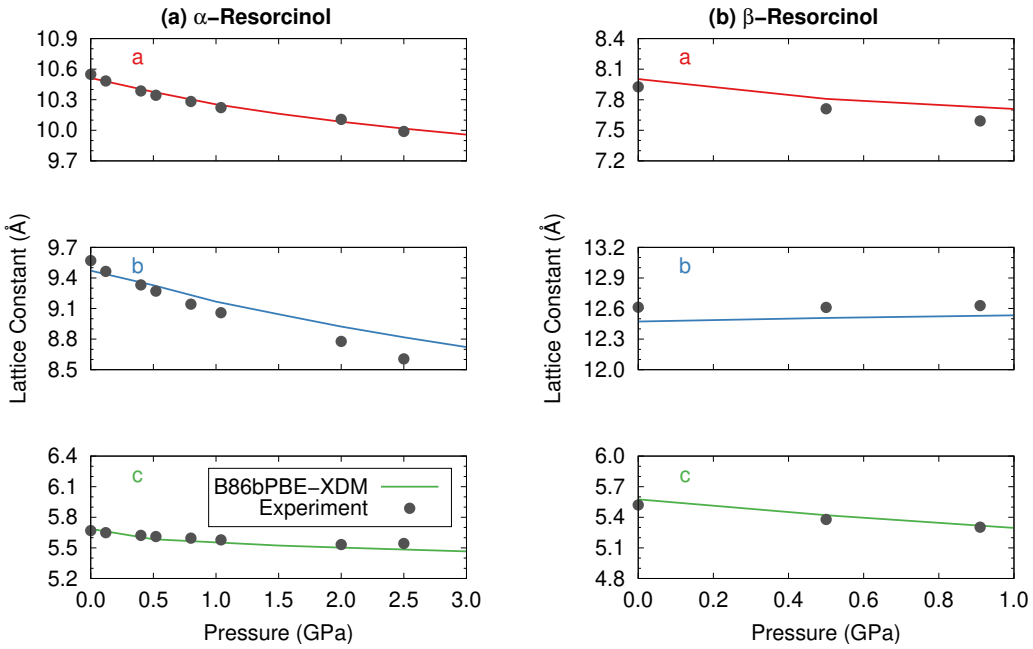

Figure 4.6: Comparison of room-temperature experimental (points)[2] and predicted (lines) quasi-harmonic B86bPBE-XDM lattice parameters of (a) α and (b) β resorcinol as a function of pressure. The first column of figures shows lattice parameters a, b, and c for the α polymorph, while the second shows them for the β form.

heating or pressurization rate, and in some cases the thermal history of the sample.[1,203] Early studies at ambient pressure reported the $\alpha \rightarrow \beta$ phase transition to occur at 344 K[217] or 347 K.[218] Ebisuzaki et al[201] reported the α to β phase transition at 369 $\pm$ 6K, followed by melting of the β phase at 382.8 $\pm$ 0.1 K. They attributed their higher phase-transition temperature to improved sample purity. Kichanov et al[1] similarly reported the ambient-pressure $\alpha \rightarrow \beta$ phase transition at 363 K by monitoring the proton spin-lattice relaxation time using free induction decay amplitudes. The phase transition temperature decreases with increasing pressure, and by 0.4 GPa, it occurs at room temperature. Figure 4.7 plots the experimentally observed phase behavior from Ref 1. Over much of the pressure region, the precise thermodynamic phase boundary is not clear. Rather, the authors observed a

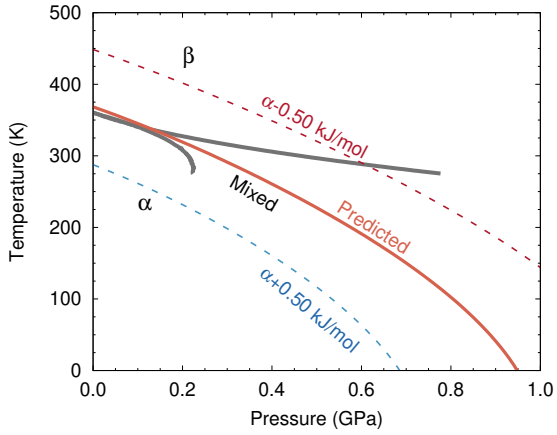

Figure 4.7: Comparison of the experimentally observed[1] and predicted phase-transition between $\alpha-$ and β-resorcinol. The solid red line corresponds to the predicted quasi-harmonic B86bPBE-XDM result, while the dotted lines indicate how the boundary changes if the α polymorph is artificially stabilized or destabilized relative to the β one.

long-lived mixed-state that contained seeds of the β phase nucleating within the α polymorph. The same mixed phase was also seen in earlier Raman studies.[203]

Figure 4.7 overlays the predicted quasi-harmonic B86bPBE-XDM thermodynamic phase boundary between the α and β phases on top of the experimental one. At ambient pressure, the phase transition is predicted to occur at 368 K, in nearly perfect agreement with the more recent experimentally reported transition temperatures of 363 K and 369 $\pm$ 6K. At 0.4 GPa, the transition is predicted to occur at 260K, in reasonable agreement with the experimental observation of a room-temperature transition at that pressure. The predicted slope of the phase-transition boundary with temperature and pressure appears qualitatively consistent with the experimental observations.

For further insight, sensitivity analysis is performed on the phase boundary by artificially stabilizing or destabilizing the α phase relative to the β one by up to 0.5 kJ/mol. The resulting phase boundaries are also plotted in Figure 4.7. Shifting the polymorph free en-

Table 4.2: Comparison of predicted and experimental thermochemical data for the α to β phase transition of resorcinol at ambient pressure and the predicted/observed phase transition temperature. [a] $\Delta H_{\alpha\to\beta}$ and $\Delta S_{\alpha\to\beta}$ were computed at 373 K, independent of the predicted phase-transition temperature.

Method	Source	$\Delta H_{\alpha\to\beta}$ (kJ/mol)	$\Delta S_{\alpha\to\beta}$ (J/(mol K))	Temperature (K)
Experiment	Ebisuzaki et al[201]	1.370 ± 0.007	3.71 ± 0.05	369 ± 6
Experiment	Bret-Dibat et al[219]	1.2 ± 0.1	3.3	367 ± 0.4
B86bPBE-XDM	this work	2.33	6.26	368
B86bPBE-XDM Γ	this work	2.17	5.97	364
PBE-TS, no QHA	Druzbicki et al[3]	0.97	4.16	373[a]

ergy difference by ±0.5 kJ/mol causes the predicted transition temperature at zero-pressure to vary by ±80 K, or roughly from ∼290–450 K. The same shift alters the pressure-induced phase transition by ±0.3–0.4 GPa at room temperature. In other words, the predicted phase boundary is very sensitive to small errors in the Gibbs free energy, as has been noted previously for other systems.[51,182] In this light, the excellent agreement between theory and experiment here reflects a combination of good model accuracy and fortuitous error cancellation.

To analyze the thermodynamic behavior more closely, Table 4.2 decomposes the free energy of transition at the phase transition temperature into its enthalpy and entropy components. Compared to the experiments of Ebisuzaki et al[201] and by Bret-Dibat et al,[219] the predicted $\Delta H_{\alpha\to\beta}$ is overestimated by 1–1.2 kJ/mol, reflecting a spurious stabilization of the α phase relative to the β one. The enthalpy error is largely compensated for by a 2.6–3.0 J/mol K overestimation of $\Delta S_{\alpha\to\beta}$ which over-stabilizes the β form relative to α at finite temperatures. Cancellation between these two errors produces the Gibbs free energy difference that leads to near perfect agreement in the predicted phase boundary.

The error in $\Delta H_{\alpha\to\beta}$ arises from a combination of the electronic lattice energy and phonon contributions, while the $\Delta S_{\alpha\to\beta}$ error stems primarily from the phonon contributions. As a crude numerical experiment, we examined how these two thermochemical quantities change when we shift the entire β-resorcinol phonon DOS toward higher frequencies. A +25 cm^{-1} phonon DOS shift decreases $\Delta H_{\alpha\to\beta}$ by about 0.25 kJ/mol, and a 50 cm^{-1} shift decreases $\Delta H_{\alpha\to\beta}$ by only 0.4 kJ/mol. In other words, only a fraction of the enthalpy error versus experiment likely stems from the phonon contribution; DFT errors in the lattice energy components are probably responsible for the larger fraction of the $\Delta H_{\alpha\to\beta}$ error. On the other hand, a $\sim$25 cm^{-1} shift would be sufficient to bring $\Delta S_{\alpha\to\beta}$ into excellent agreement with experiment. While the true phonon errors are surely more nuanced than a simple shift of the entire phonon DOS employed here, these results do suggest that the discrepancies between the predicted and observed thermochemical quantities in Table 4.2 can readily be accounted for within the expected errors of DFT.

Druzbicki et al[3] computed $\Delta H_{\alpha\to\beta}$ and $\Delta S_{\alpha\to\beta}$ at 373 K using a variety of density functionals and the harmonic approximation. While most of the functionals they tested gave larger errors than those seen here, PBE-TS performed very well, with enthalpies and entropies of transition of 0.97 kJ/mol and 4.16 J/mol K at 373 K, despite neglecting thermal expansion. On the other hand, it appears that despite the better agreement in the enthalpy and entropy of transition, the error cancellation between the two is less effective: Although their study did not report the temperature-dependence of $\Delta H_{\alpha\to\beta}$ and $\Delta S_{\alpha\to\beta}$, using the reported 373 K values would indicate a phase transition around 235 K, which is about 130 K below the experimental transition temperature. Furthermore, these PBE-TS thermochem-

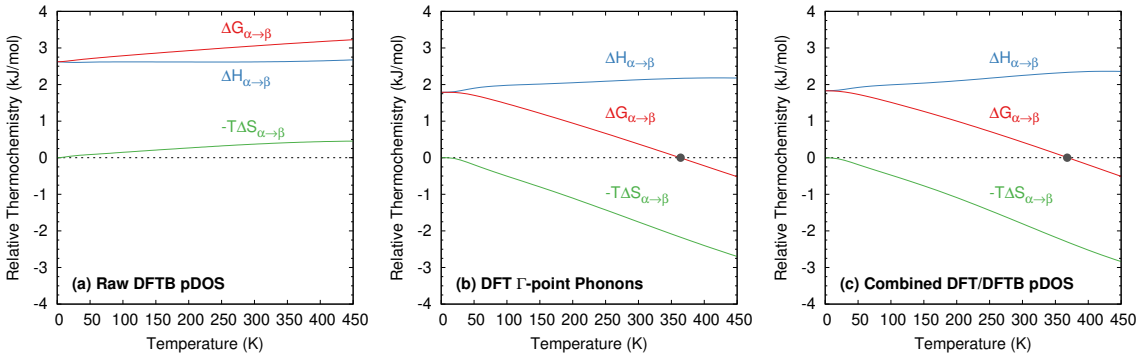

Figure 4.8: Relative enthalpy, entropy ($-T\Delta S$), and Gibbs free energy differences for the $\alpha \rightarrow \beta$ phase change (in kJ/mol) using (a) the raw DFTB3-D3(BJ) phonon density of states or (b) the phonon density of states obtained after performing the B86bPBE-XDM Γ-point shift and acoustic mode corrections. The gray point in (b) indicates the phase transition at 407 K.

ical results were obtained for structures which did not account for thermal expansion and therefore underestimate the molar volumes considerably (Figure 4.5).

Next, in order to assess the impact of the phonon DOS approximation used here, we also examined the Gibbs free energies computed from the DFTB3-D3(BJ) phonon density of states (without applying the DFT Γ-point shift or acoustic mode correction). In that case, the two phases are incorrectly predicted to be monotropically related—i.e. α-resorcinol is thermodynamically preferred at all temperatures and pressures, and there is no $\alpha \rightarrow \beta$ phase transition. As shown in Figures 4.8a and 4.8c, enthalpy favors the α form throughout this temperature range for both phonon models, and the difference in $\Delta H_{\alpha \rightarrow \beta}$ between the two models is less than 0.8 kJ/mol. However, the two models predict completely different relative entropies. The polymorph entropy difference computed from the raw DFTB3-D3(BJ) phonon DOS has the wrong sign—it predicts that the α phase entropy is always greater than the β phase entropy (or in Figure 4.8, that $-T\Delta S_{\alpha \rightarrow \beta}$ is positive). This error

prevents the relative Gibbs free energy in Figure 4.8a from changing sign. After applying both the DFT-based Γ-point shift and acoustic mode corrections, however, we see that the relative entropy reverses sign such that the β phase is increasingly favored at higher temperatures. At 368 K, the corrected entropy becomes sufficiently large to overcome the enthalpy difference between the two phases, and the β polymorph becomes the stable phase. In other words, entropy drives the temperature-dependent phase transition, and correcting the DFTB3-D3(BJ) phonon DOS with the DFT Γ-point shift is essential to obtaining the proper enantiotropic relationship between the two phases.

For completeness, we also examine the performance of B86bPBE-XDM employing only Γ-point phonons, omitting the DFTB phonon dispersion contribution. At room temperature, the total Gibbs' free energy of each phase is ∼3.5-3.75 kJ/mol smaller in magnitude without phonon dispersion. Because phonon dispersion is most pronounced in the low-frequency and acoustic modes, the majority of this difference stems from the decreased entropy in the Γ-point-only model. Nevertheless, much of this difference cancels when computing the thermochemical energy differences between the two polymorphs. As shown in Figure 4.8b and 4.8c, the enthalpy, entropy, and free energy changes differ only by a few tenths of a kJ/mol or less. Moreover, as shown in Table 4.2, the predicted $\Delta H_{\alpha\rightarrow\beta}$ and $\Delta S_{\alpha\rightarrow\beta}$ values agree marginally better with experiment, but the predicted phase transition temperature at ambient pressure is nearly identical (364 K vs. 368 K with phonon dispersion). The strong similarity between the models with and without phonon dispersion here likely reflects the similarity of the crystal packing between the two forms.

For further evidence of the fortuitous nature of the agreement in the thermochemical properties, Figure 4.9 compares the simulated inelastic neutron scattering (INS) spectra against the experimental ones from Ref 3 for the three different phonon DOS models: raw DFTB, DFT Γ-point, and the mixed DFT/DFTB approach. For the ∼50-300 cm^{-1} region where phonon dispersion is generally more appreciable, the combined DFT/DFTB phonon DOS model gives improved agreement with the experimental spectra compared to the DFT Γ-point phonon modes only. It does appear that the DFT/DFTB phonon DOS model underestimates the acoustic mode frequencies moderately, leading to an erroneous peak below ∼50 cm^{-1}. The Γ-point DFT model nominally appears more faithful to experiment in the sub-50 cm^{-1} region by virtue of neglecting the acoustic mode contributions entirely. In the high-frequency region above 300 cm^{-1}, the differences between the DFT Γ-point and DFT/DFTB models are smaller. In contrast to the DFT/DFTB or DFT Γ-point spectra, the INS spectrum simulated from the raw DFTB phonon DOS exhibits poor agreement with experiment, further demonstrating the need for correcting the DFTB phonon frequencies as is done here.

Finally, we compare the predicted and experimental enthalpies of sublimation for α-resorcinol. Many experimental values for the α-resorcinol sublimation enthalpy have been reported.[220–227] Table 4.3 lists the averaged 298 K value of 95.6 ± 0.6 kJ/mol obtained by critical analysis of several studies[225] along with the more recent measurement from Gonçalves et al of 99.7 ± 0.4 kJ/mol.[227] The theoretical sublimation enthalpy was computed for using the standard ideal gas, rigid rotor, and harmonic oscillator partition function expressions for the gas-phase species (see Ref 104 for details). The room-temperature pre-

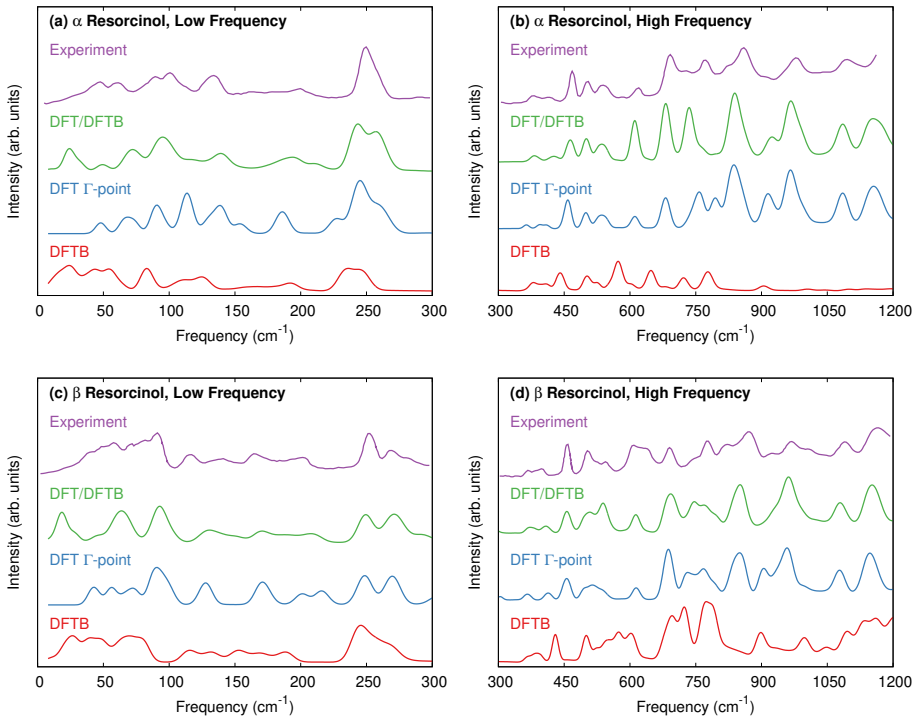

Figure 4.9: Inelastic neutron scattering spectra for α and β resorcinol in the low- and high-frequency regions. The experimental spectra at 35 K are compared against quasi-harmonic ones using the raw DFTB phonon DOS, the Γ-point DFT phonon spectra, and the combined DFT/DFTB phonon DOS.[3]

Table 4.3: Comparison between experimental and predicted sublimation enthalpies at 298 K.

Method	Source	ΔH_{sub} (kJ/mol)
Experiment	Verevkin & Kozlova[225]	95.6 ± 0.6
Experiment	Gonçalves et al[227]	99.7 ± 0.4
B86bPBE-XDM	this work	102.7

diction of 102.7 kJ/mol overestimates the experimental values by 3–7 kJ/mol, depending on which experimental value is used. This error is consistent with earlier quasi-harmonic ΔH_{sub} benchmarks in small-molecule crystals[122] and DFT lattice energy benchmarks.[96,119,215] On the other hand, this error is several times larger than the error in $\Delta H_{\alpha\rightarrow\beta}$ in Table 4.2, highlighting once again the importance of error cancellation in predicting the phase boundaries correctly. Errors in describing the intermolecular interactions in the crystalline phase are fully exposed when computing the lattice energy or sublimation enthalpy, but they cancel somewhat when examining energy differences between polymorphs.

4.5 Conclusions

Predicting phase boundaries between crystal polymorphs represents one of the challenging problems in modeling the organic solid state due to the extreme sensitivity of the results to small errors in the models. This challenge is compounded by the computational expense associated with computing accurate electronic energies and well-converged phonon densities of state over a range of temperatures and pressures in order to obtain the Gibbs free energies. The present work shows how DFT and DFTB can be combined in a quasi-harmonic model that accurately describes the crystal structures, thermochemistry, and

phase boundaries for the α and β phases of resorcinol. The key approximation here lies in using DFT Γ-point phonon frequencies to shift the DFTB phonon density of states. Overall, the model reproduces experimental crystal structures to within 1–2% or better, especially at lower pressures. It predicts the $\alpha \rightarrow \beta$ phase transition boundary to within a few degrees Kelvin. However, the phase transition temperature is shown to be very sensitive to small changes in the relative free energy. The level of quantitative agreement in the transition temperature reflects fortuitous error cancellation between the enthalpy and entropy, both of which are overestimated by the model relative to experiment.

The mixture of DFT and DFTB used to compute the phonon density of states here reduces the computational costs associated by orders of magnitude,[198] making it much more feasible to model the finite-temperature thermochemistry of chemically interesting organic crystals without consuming exorbitant amounts of computer resources. At the same time, DFTB3-D3(BJ) alone proved inadequate, and the DFT-derived correction to the DFTB phonon density of states was essential to capturing the correct phase behavior in resorcinol. Therefore, the combined DFT/DFTB approach appears to provide a good balance between computational cost and accuracy. In this particular case, Γ-point DFT phonons perform about the same as the mixed approach, though one would expect greater differences in polymorphs where the crystal packing exhibits greater differences in conformation and/or intermolecular packing.

In the future, it will be interesting to apply these same modeling procedures to crystals of more complex species, such as small-molecule pharmaceuticals. The resorcinol polymorphs here involve both hydrogen bonding and significant van der Waals dispersion

interactions through the π system. In that regard, this system is reasonably representative of many rigid-molecule organic crystals. On the other hand, the similar crystal packings between the two polymorphs studied here may facilitate error cancellation to a greater extent compared to other polymorphic systems. This system also lacks the greater conformational flexibility of many larger molecules and pharmaceuticals that might complicate quasi-harmonic treatments (though some recent research has suggested that limitations of the quasi-harmonic approximation may not be well-correlated with conformational flexibility[117]).

To improve the accuracy of these approaches, it may be useful to improve the quality of the DFT electronic energies via use of hybrid or other higher-quality density functionals,[98] inclusion of conformational energy corrections when needed,[66] or perhaps even employing post-DFT treatments where feasible.[65,122]Fortunately, the Γ-point "reference" frequencies used in the matching procedure are not restricted to DFT-GGA. This provides a particular advantage over the density functional perturbation treatment, where the implementation of hybrid density functionals is less straightforward.[228] Incorporation of additional phonon mode anharmonicity[120] might also help improve the predicted thermochemistry, especially for molecules with greater intramolecular conformational flexibility. Regardless of the specific modeling choices made, one should take care to understand how uncertainties in the computational models manifest in the final predictions and remain cognizant of the role of error cancellation in making useful thermochemical predictions for the organic solid state.

Chapter 5

Organic Semiconducting Crystals

Classification of charge mobility in organic semiconductors is imperative in modern device design, but computational methods are often restricted to the zero- or low-temperature regime. The thermal fluctuation of intermolecular charge transfer integrals indicates that a finite-temperature approach is necessary in accurately predicting the parameters of charge carrier mobility. These effects can be captured using quasi-harmonic techniques, which can predict the physical properties of thermally expanded organic molecular crystals. In this work we characterize the temperature dependence of intermolecular charge transfer integrals due to the thermal expansion of three popular Van der Waals bound molecular semiconducting crystals.

5.1 Introduction

The search for efficient organic semiconductors (OSCs) in organoelectronics has accelerated significantly in recent years. Market research predicts that the global annual

semiconductor market is expected to grow from USD 53.3 billion in 2018 to 179.4 billion by 2024, an annual growth rate of 22.4%.[229] While the efficiency of organic semiconductors is still lacking compared to polycrystalline silicon, it has increased by several orders of magnitude over the past decade. OSCs also pave the way for flexible electronics, fine-tuned electronic properties via organic synthesis,[10,230] and a more energy efficient manufacturing processes. Steep increases in viability shows incredible promise in the field of organic semiconductors.[231]

OSC efficiency of is most simply characterized by charge carrier mobility μ. This quantity can be somewhat elusive to calculate directly, falling in either band-like high mobility transport regimes as seen in metals and smaller-band-gap semiconductors,[232,233] and thermally-activated charge hopping akin to Marcus transport as seen in larger-band-gap semiconductors and electronic insulators.[234,235] Higher-efficacy organic semiconductors exist in an intermediate transient localization regime where mobility is limited by carrier-phonon coupling, which is significant in Van der Waals bound organic crystals.[236,237] The evaluation of bulk mobility μ within the transient localization regime requires extensive knowledge of the dynamics of the system. Regardless of the charge transport model, transfer integrals are an important parameter in the determination of μ and can be characterized in a more straightforward manner.

Changes in crystal packing and mechanical strain can significantly impact charge transport parameters.[13,238–242] Chemical modification of a species provides many possibilities for tuning molecular electronic properties, but it can also impact intermolecular packing therefore bulk transport properties. For example, oxidation of the pentacene molecule

disrupts the molecular π-conjugation and alters the intermolecular packing from the herringbone motif to a slip-stacked crystal structure.[230,243] Similar structure-based approaches in optimizing carrier mobility have been focused on stifling intermolecular oscillations with the introduction of bulky functional groups.[236,241] A unifying concept in the strategies used to boost the viability of OSCs is that even the most nuanced contortions of the crystal can have major impacts on the intermolecular interactions governing bulk mobility. Thermodynamic effects such as thermal expansion are known to alter crystal structure, however they are less often studied in this context.

Temperature effects on carrier mobility is not unknown, however simulation of transport properties is often limited in practice to experimentally determined structures at finite temperatures due to the high cost of necessary lattice dynamics calculations. This could be problematic for the assessment of carrier mobility parameters in structures determined via crystal structure prediction techniques, often ranking candidate crystals at the electronic minimum. This work aims to establish a reliable and affordable thermal expansion procedure using the quasiharmonic approximation for organic semiconducting crystals. Further, we highlight the effects of thermal expansion on the carrier mobility parameters in three common organic semiconductors: naphthalene, pentacene, and benzothieno[3,2-b][1]benzothiophene (BTBT). Readily determined structural and electronic properties at several temperatures could prove useful for device research and fabrication in real-life conditions.

5.2 Theory

5.2.1 Carrier Mobility and Transfer Integrals

Charge transport properties and their relationship to crystal structure is most clearly conveyed in the tight-binding approximation:[53]

$$H = \sum_i \epsilon_i a_i^+ a_i + \sum_{i \neq j} t_{ij} a_i^+ a_j \tag{5.1}$$

where a_i^+ and a_i are the creation and annihilation operators for an electron on molecular site i, respectively, ϵ_i is the electron site energy, and t_{ij} is the transfer integral. The remainder of this study focuses on the t_{ij} parameter, which is an important indicator of efficient charge transfer.

Evaluation of t_{ij} from a single isolated dimer calculation can be approximated as half of the orbital splitting energy, however this has been shown to yield inaccurate transfer integrals as it neglects electronic polarization. Practical evaluation of t_{ij} instead involves a projection of the isolated monomer's frontier orbitals on those of the dimer.[53,54] The secular equation describing the dimer in the basis of monomer frontier orbitals is:

$$\mathbf{HC} - E\mathbf{SC} = 0 \quad ; \quad \mathbf{H} = \begin{pmatrix} e_1 & J_{12} \\ J_{12} & e_2 \end{pmatrix} \tag{5.2}$$

Where $\mathbf{H}$ is the electronic Hamiltonian, $\mathbf{C}$ is a matrix of orbital coefficients, E is the dimer energy, $\mathbf{S}$ is the overlap matrix, e_i is the site energy of molecule i and J_{ij} is the electronic

transfer integral derived from the isolated molecular constituents of the dimer:

$$J_{ij} = \langle \Psi_i | H_{ij} | \Psi_j \rangle \tag{5.3}$$

Here, Ψ_i is the frontier orbital on the i^{th} molecule. J_{ij} is physically equivalent to t_{ij}, however it is represented in a non-orthogonal basis of the isolated monomers. This is corrected by projecting the orbitals of the monomers onto the orbitals of the dimer, giving an accurate transfer integral denoted J_{ij}^{eff}.[53–57] The present study focuses on the hole mobility, where the frontier orbitals of interest are the HOMO and HOMO-1 orbitals of the dimer, represented by the HOMO's of its constituent monomers.

In a semiconducting crystal, J_{ij}^{eff} is evaluated for each unique pair of molecules whose distance is close enough for considerable electronic coupling across interacting monomers. Exploiting translational and space group symmetry allows one to evaluate only the symmetrically-unique subset of possible dimer pairs. While longer-range electron transfer can be important in evaluating bulk mobility, the present study focuses on local transfer integrals, which will be most sensitive to changes in crystal structure/volume.

Intermolecular charge transfer depends strongly on the degree of orbital overlap in the dimer pair. Changes in the crystal structure alter this overlap. For example, increasing intermolecular separation reduces the strength of interfacial π stacking interactions and the orbital overlap. Subtle changes in relative orientations of molecules, such as a face-to-edge angle in a herringbone-type packing, can also impact transfer integrals.[55] Accordingly, accurate knowledge of the unit cell is important when calculation transfer integrals and carrier mobility.

5.2.2 Quasi-Harmonic Approximation

The quasi-harmonic approximation (QHA) is employed here to predict the molecular crystal volume/atomic positions as a function of temperature. Standard DFT geometry optimization produces the minimum electronic energy crystal structure. The volume of this 0 K structure will typically be several percent smaller than the room-temperature crystal structure due to the neglect of zero-point vibrational energy and thermal expansion.[113] Even a few percent change in volume can impact certain bulk properties appreciably.[244,245] To obtain the finite-temperature structure, one should instead minimize the Gibbs free energy $G(T, P, V)$ with respect to the atomic positions and lattice vectors for a chosen temperature and pressure:

$$G(T, P, V) = U_{el}(V) + F_{vib}(T, V) + PV \tag{5.4}$$

where $U_{el}(V)$ is the electronic energy as a function of volume, $F_{vib}(T, V)$ is the Helmholtz vibrational free energy, and PV is the pressure-volume contribution which is typically negligible at ambient pressures. For a given volume, the harmonic Helmholtz vibrational free energy is computed as,

$$F_{vib}(T) = 3nN_A k_B T \int_0^\infty \ln\left[2\sinh\left(\frac{\hbar\omega_k}{2k_B T}\right)\right] g(\omega_k) d\omega_k \tag{5.5}$$

where n is the number of atoms in the crystallographic unit cell, N_a is Avogadro's number, $\hbar$ is Planck's constant, k_B is the Boltzmann constant, T is temperature, and $g(\omega)$ is the phonon density of states (pDOS) at that volume.

The key difficulty in minimizing the Gibbs free energy stems from how the pDOS, and therefore F_{vib}, varies with volume. A standard harmonic treatment of the phonons neglects this volume-dependence and therefore does not predict any thermal expansion. To capture the volume-dependence of the Gibbs free energy at finite temperatures and pressures, the QHA is employed. In particular, the electronic energy of the crystal is optimized with DFT at several different unit cell volumes. The harmonic phonon density of states is computed for each structure using the approach described below in Sec 5.2.3. From these calculations, $U_{el}(V)$, $F_{vib}(T, V)$ and therefore $G(T, P, V)$ can be interpolated as a one-dimensional function of volume for any given temperature and pressure. Minimizing G with respect to volume at the chosen temperature and pressure gives the optimal unit cell volume. The final lattice parameters and atomic positions for that T and P are then obtained from a constant volume DFT structure optimization at the optimal volume. The QHA often models thermal expansion of organic molecular crystals well, at least for without too much flexibility and at low or moderate temperatures.[13,246,247]

5.2.3 Phonon Calculations

Adequate convergence of phonon density of states $g(\omega)$, particularly including phonon dispersion of the intermolecular modes, is important for predicting thermal expansion accurately. This is often achieved via the supercell method, but performing a harmonic phonon DFT calculation on large supercells can be computationally demanding. Instead, we employ our recently-developed mixed DFT/density functional tight binding (DFTB) approximation scheme,[198] which is multiple orders of magnitude faster than a traditional DFT calculation.

The approximation begins by relaxing the atomic positions for the given volume and computing the supercell phonons frequencies with semi-empirical DFTB, resulting in a series of phonon dispersion curves. The low computational cost of DFTB makes obtaining a well-converged pDOS from large supercell phonon calculations much more feasible compared to DFT, but the accuracy of DFTB phonon band frequencies is often comparatively poor. To improve the accuracy of the phonon frequencies, a DFT phonon calculation is also performed on the crystallographic unit cell (Γ point). Using the crystallographic unit cell instead of a supercell makes this DFT phonon calculation much more affordable. Then each optical DFTB phonon band is shifted based on the difference between the DFT and DFTB frequencies at the Γ point ($\mathbf{k} = \mathbf{0}$):

$$\omega_i^{final}(\mathbf{k}) \approx \omega_i^{DFTB}(\mathbf{k}) + \left(\omega_i^{DFT}(\mathbf{0}) - \omega_i^{DFTB}(\mathbf{0})\right) \tag{5.6}$$

To determine the frequency corrections, the DFT and DFTB phonon modes are matched based on maximizing the overlap of the normal mode eigenvectors.[198] In the end, the phonon bands have the "correct" DFT phonon frequencies at the Γ point, but the dispersion of each phonon band is obtained from DFTB.

Unfortunately, this mixed DFT/DFTB approach is not applicable to the acoustic modes, since their frequencies are zero at the Γ point by definition. In our experience, standard DFTB approximations describe the acoustic modes poorly away from the Γ point ($\mathbf{k} \neq 0$). The low-frequency acoustic modes contribute significantly to thermal expansion, so it is important to improve the description of these modes.

Accordingly, the acoustic modes are evaluated from DFT-computed stress-strain relationships and the theory of elasticity. Computing the DFT elastic constants and solving for the eigenvalues of the Christoffel matrix yields the sound velocities in each plane of the crystal. The sound velocities can be related to the acoustic mode frequencies via Debye theory and a sinusoidal extrapolation of the acoustic modes to the Brillouin zone edges. The final pDOS is the sum of contributions from the optical and acoustic modes. See ref 198 for details. This pDOS approximation has previously been validated for small-molecule crystal thermochemistry,[198] the finite-temperature and pressure structures of resorcinol, and for predicting the polymorph phase diagram of resorcinol.[245] Compared to DFT supercell calculations, it introduces $\sim$1 kJ/mol errors into the absolute Helmholtz vibrational free energies of small molecules, and the errors in the relative free energy differences between polymorphs appear to be even smaller.

5.3 Computational details

5.3.1 Crystal optimizations

Initial crystal structures for the three systems studied here were pulled from the Cambridge Structure Database (CSD): naphthalene (NAPHTA24[4]), pentacene (PENCEN04[248]), and BTBT (PODKEA[9]). For consistency with the computations, the experimental naphthalene crystal was transformed to from the $P2_1/a$ space group setting to $P2_1/c$; all cell vector comparisons are with respect to the $P2_1/c$ crystal. Pentacene can adopt a variety of different polymorphs depending on the crystallization method; these are often characterized by d(001)-spacings.[248,249] The structure used to initialize the optimiza-

tions here corresponds to Form II at 90K, which is also known as the 14.5 Å d-spacing variant or the low temperature form. Variable cell optimizations were performed with density functional theory, using the Perdew-Burke-Erzhoff (PBE)[78] density functional with Grimme's D3 dispersion correction[79] and a 6-311G(2d,2p) basis. All optimizations were carried out in the CRYSTAL17 module with an appropriate Monkhorst-Pack k-point grid ensuring an energy-per-cell convergence of 0.001 eV, which has shown to be sufficient for insulating and semiconducting systems.[250] Fixed cell optimizations for determination of elastic constants on the various strained volumes of each crystal were performed in Quantum Espresso v.6.4[210,251] with the PBE functional and D3 dispersion correction, with a 60 Ry planewave cutoff.

5.3.2 Phonon Density of States Calculations

Harmonic Γ-point phonons and eigenvectors were evaluated with Phonopy v2.4.0 and its CRYSTAL17 interface.[252] DFTB Γ-point and supercell phonons were evaluated with DFTB+. DFT/DFTB hybrid phonon density of state integrations, as well as QHA-based cell volume optimizations, were carried out with our previously developed ModeMatch v0.0.10 code.[198,245] Integration q-points and band samplings were determined via the scheme proposed by Setyawan *et al.*[253] Elastic constants, sound velocities, and acoustic frequencies were determined with ModeMatch v0.0.10.

5.3.3 Thermal Expansion

The QHA was applied to all crystals as described in our previous work.[198,245] In particular, the optimal unit cell volume was determined by fully relaxing the atomic posi-

tions and lattice parameters with DFT. Four additional constant-volume optimizations were performed on unit cells whose volumes were expanded or contracted from the equilibrium volume by ±2% or ±4%. These constant-volume optimizations allow the lattice parameters to vary subject to maintaining the overall target volume, thereby allowing quasi-anisotropic compression/expansion. Phonon density of states calculations were then performed on each of the five optimized structures via the mixed DFT/DFTB approach. The resulting phonon frequencies were used to determine the F_{vib} as a function of volume and temperature, from which the Gibbs free energy could be computed. A final fit to a Burch-Murnaghan equation of state is used to the predicted $G(T, P, V)$, where compressed and expanded volumes are fit separately to better model the anharmonic well. For a given temperature and pressure, the minimum free energy and its corresponding cell volume V_{QHA} were be extracted via one-dimensional optimization. Final atomic positions and lattice parameters were obtained via a final constant-volume optimization of the unit cell at V_{QHA} computed for those thermodynamic conditions. The QHA procedure was performed using the ModeMatch v0.0.10 python module.

5.3.4 Transfer Integrals

Transfer integrals were evaluated for each unique dimer pair in the supercell up to a cutoff of 10 Å, after which the values become small.[254] To do so, $3 \times 3 \times 3$ supercells were constructed for the predicted finite-temperature QHA crystal geometries of interest. The individual monomer and dimer orbital energies were determined with the hybrid-GGA PBE0 density functional and the def2-TZVP basis set within the *GAUSSIAN09* software

package.[255] Monomer basis set orthogonalization to the dimer pair and subsequent evaluation of J_{ij}^{eff} was carried out with the open-source CATNIP module.[256]

5.4 Results and Discussion

5.4.1 Thermal Expansion

Naphthalene: Figure 5.1a plots how the lattice constants and cell volume of naphthalene change with increasing temperature. Lattice constants a, b, and c expand anisotropically, elongating by 3.8%, 2.5%, and 4.6%, respectively, between the DFT electronic energy minimum crystal structure and the quasi-harmonic DFT structure at 300 K. A significant fraction of that expansion stems from the inclusion of zero-point vibrational energy, as has been noted previously for other systems.[104] Comparing against three sets of temperature-dependent x-ray and neutron diffraction studies,[4,7,257] the predicted lattice constants lie within ∼0.1 Å or better of experiment. The largest errors among the three lattice constants occur for the a lattice parameter, whose value starts out 0.07 Å too large relative to experiment at low temperature, but the rate of thermal expansion is too small such that it underestimates the experimental value by 0.1 Å at room-temperature. The errors for the b and c lattice constants are at least 2-3-fold smaller. In contrast to the three lattice constants, the predicted temperature dependence of the β angle is poorly captured by the model: its value lies within 0.7° of experiment at low temperature, but it is 2.5° too small at room temperature. These β angle errors are still rather small, but they will impact on the predicted transfer integrals as discussed in the next section.

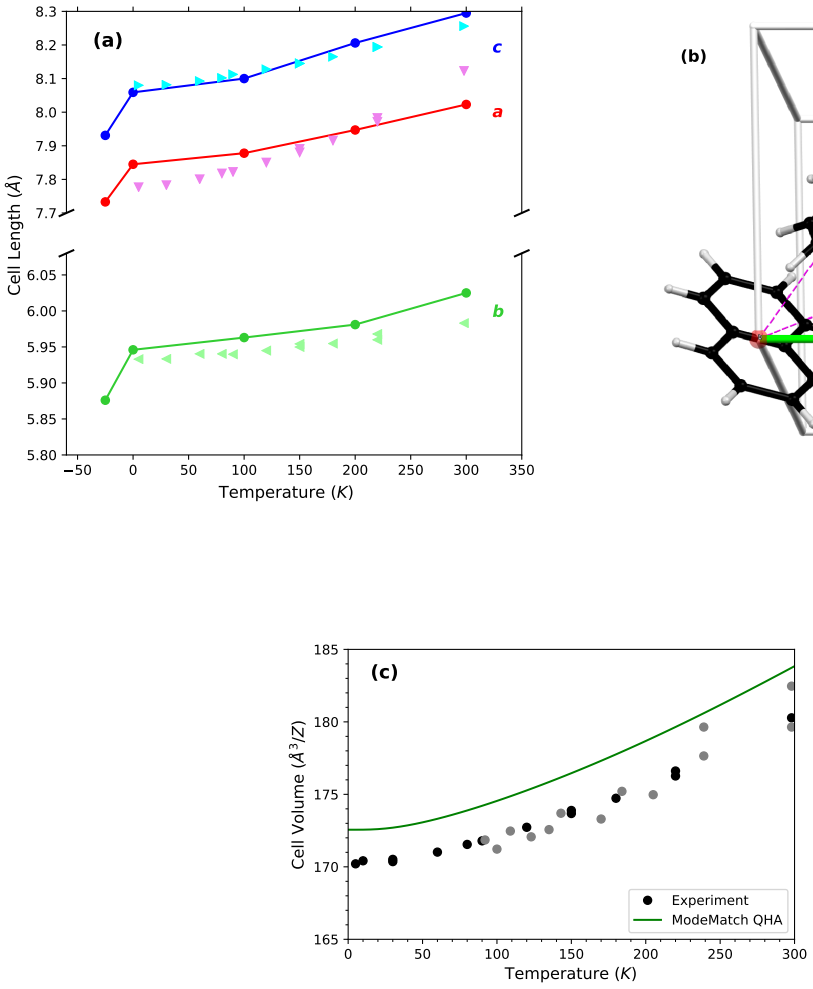

Figure 5.1: **(a)** Comparison of predicted and experimental lattice constants for napthalene as a function of temperature. Lattice vectors a, b, and c are shown by the red, green, and blue lines, respectively. Experimental values are shown in colored triangles. **(b)** $P2_1/c$ representation of the 6 K experimental structure as determined by Capelli *et al.*[4] Colored axes coincide with the color scheming in (a). Dashed magenta dashed lines indicate the primary dimer pairs analyzed for charge transport parameters. **(c)** Comparison of the predicted and experimental unit cell volumes as a function of temperature. Black and gray dots represent experimentally observed unit cell volumes.[4–7]

Nevertheless, the overall volume and its expansion with temperature are predicted accurately. The quasi-harmonic predicted volumes are $1.6 \pm 0.3\%$ too large on average (Figure 5.1c), due in large part to the under-estimated β angle. The predicted rate of expansion with temperature agrees even better with experiment, with less than a percentage point difference between the volume errors at low temperature and those near room temperature. The predicted 6.5% total expansion between 5 K and room temperature, the largest seen among the three systems investigated here, agrees well with the 5.9% thermal expansion from the structures reported by Capelli et al.[258] Such accuracy for the models is competitive with previous quasi-harmonic molar volume predictions for naphthalene and other crystals.[13,104,122,216]

BTBT The thermal expansion of BTBT is shown in Figure 5.2. The a, b, and c lattice constants expand by 1.8%, 1.8%, and 3.8%, respectively, upon heating to room temperature. This predicted lattice constants and their rate of expansion with temperature are again generally consistent with experiment, with the largest errors occurring for the a constant. Importantly, the subtle widening of the β cell angle with increasing temperature is captured by the QHA calculations. This angle proves important for capturing the edge-face transfer integral between molecules in the bc-plane.

The overall volume of the BTBT unit cell expands 4.3% between 0 K and 300 K, as shown in 5.2c. The predicted QHA volumes reproduce to the experimental ones to within 1%. This excellent accuracy of the predicted volumes at higher temperatures partly reflects the error cancellation between the over-estimation of the a and b constants and the under-estimation of c. Similar cancellations occurred for naphthalene as well. Compared

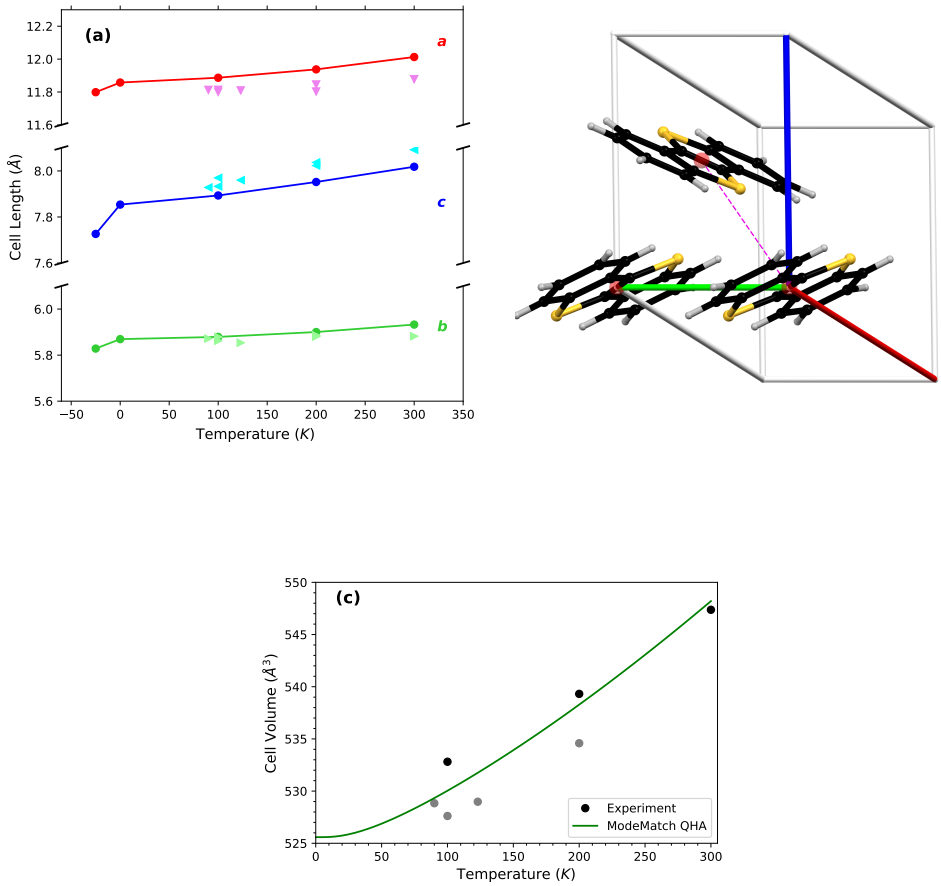

Figure 5.2: **(a)** Comparison of predicted and experimental lattice constants for the BTBT crystal as a function of temperature. Lattice constants a, b, and c are shown by the red, green, and blue lines, respectively. Experimental values are shown in colored triangles.[8–12] **(b)** Crystal structure of BTBT crystal structure, with the axes colored to match part (a). Dashed magenta dashed lines indicate the primary dimer pairs analyzed for charge transport parameters **(c)** Comparison of the predicted and experimental unit cell volumes as a function of temperature, in Å^3 per molecule. Black dots represent the volumes reported in the temperature dependent study of Banks et al,[8] while the gray points represent volumes from other entries in the CSD.[9–12]

to the temperature-dependent X-ray diffraction measurements of Banks et al[8] at 100 K, 200 K, and 300 K (black points in Figure 5.2c), the predicted rate of thermal expansion with increasing temperature appears slightly too large. On the other hand, it appears more reasonable if one also considers additional reported unit cell volumes from the CSD.[9–12]

Pentacene Finally, we examine the thermal expansion of pentacene. Experimental unit cell volumes for pentacene have been reported up to 400 K. However, we primarily focus on temperatures up to room temperature for a few reasons: this temperature regime is most relevant for organic semi-conductor devices, the performance of the quasi-harmonic approximation deteriorates at higher temperatures in general, and finally the experimental volume at 400 K lies outside the range of volumes explicitly sampled in generated the energy-volume curve used in the QHA procedure (the range could be extended, but we have not done so because of the other two reasons). As shown in Figure 5.3, the predicted volumes generally reproduce the experimental lattice constants and volumes well up to room temperature. The predicted volumes like within $\sim$1% of experiment up to 300 K, though they increase to $\sim$2.1% at 400 K. Based on the predicted lattice constants in Figure 5.3a, it appears that the rate of thermal expansion with temperature is mildly underestimated. The lattice constants lie within $\sim$0.1 Å of experiment, while the three angles of the triclinic unit cell are mostly within 1°. Only at 300 K does the β angle error grow to 2.2°.

Overall, the predicted quasi-harmonic finite-temperature structures using the mixed DFTB/DFT phonon density of states agree well with experiment for all three systems.

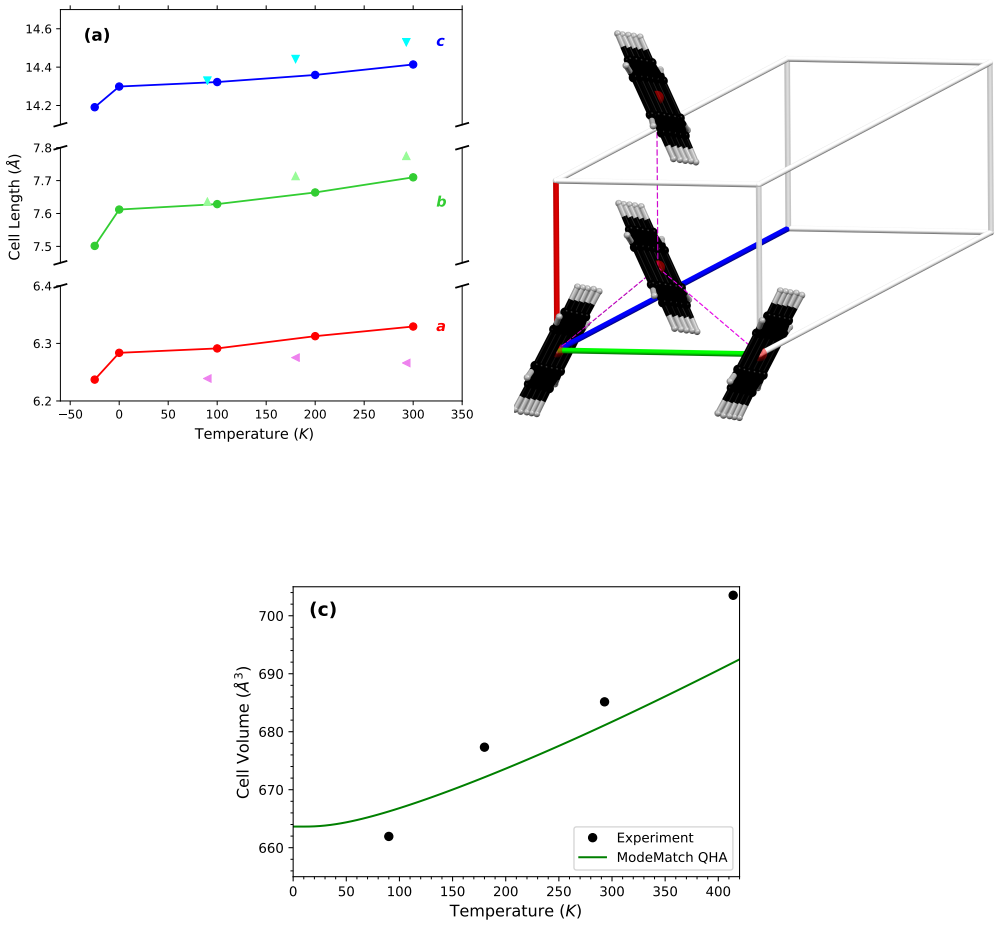

Figure 5.3: **(a)** Comparison of predicted and experimental lattice constants for the pentacene crystal as a function of temperature. Lattice vectors a, b, and c are shown by the red, green, and blue lines, respectively. Experimental values are shown in colored triangles.[9–13] **(b)** Experimental 100K BTBT crystal structure as determined by Vyas *et al.* Colored axes coincide with the color scheming in (a). Select symmetrically equivalent molecules, centroids, and magenta dashed lines are displayed to show the primary dimer pairs analyzed for charge transport parameters. **(c)** Predicted thermal expansion of the fully relaxed electronic minimum BTBT crystal. Black and gray dots coincide with experimentally observed finite temperature cell volumes.

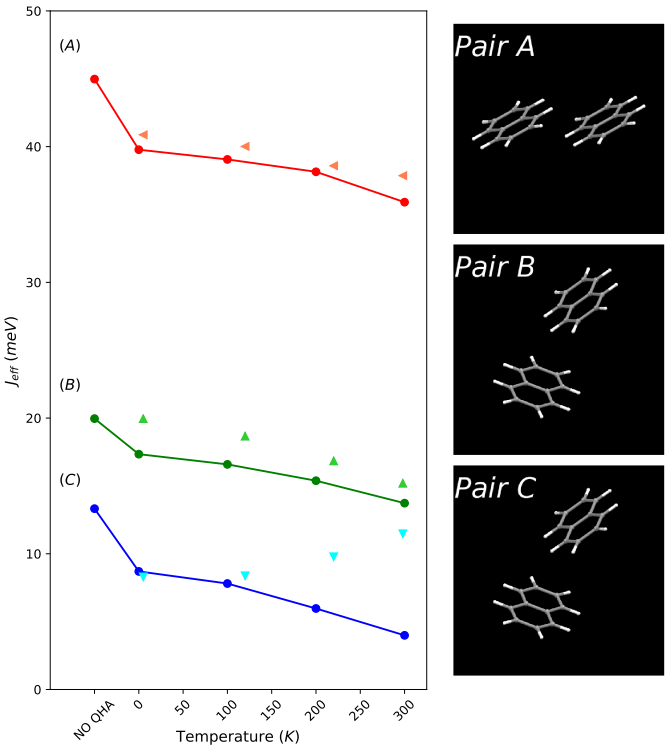

Figure 5.4: Transfer integrals as a function of temperature (left) and the corresponding dimer interaction (right) for crystalline naphthalene. Connected lines are evaluated from dimers pulled from the QHA-predicted cell, while angled points are from the fixed cell optimized experimental structure.

Source	Temperature (K)	Volume	%Err
expt[248]	90	661.9	–
expt[259]	180	677.3	–
expt[248]	293	685.2	–
Modematch QHA	90	666.3	0.65
Modematch QHA	180	672.2	-0.77
Modematch QHA	293	681.3	-0.61

Table 5.1: Thermal expansion of the pentacene Form II crystal.

5.4.2 Transfer Integrals

Having used the quasi-harmonic approximation to predict how unit cells change as a function of temperature, we now investigate the impact of thermal expansion on the predicted transfer integrals between adjacent molecules in the crystal.

Naphthalene

Naphthalene adopts a herringbone packing in the monoclinic $P2_1/c$ space group. Figure 5.4 presents the structures and transfer integrals for the three primary, symmetrically-unique electron transfer dimer pairs. Dimer pair A exhibits a co-facial slipped-stack geometry, while pairs B and C both exhibit tilted-T-shaped arrangements with different lateral offsets. The co-facial interaction and shorter intermolecular center-of-mass separation in A lead to it being the most significant hole transfer pathway.

Thermal expansion increases the intermolecular separations within the dimer pairs, which in turn causes noticeable changes in the magnitude of intermolecular electronic coupling J_{eff} as a function of temperature (Figure 5.4). The "No QHA" data points in Figure 5.4 correspond to the transfer integrals calculated with the dimer geometries taken from

the fully-relaxed DFT crystal structure, without applying the quasi-harmonic approximation. In contrast, the 0 K data points include the impact of quasi-harmonic zero-point vibrational expansion of the unit cell, and the higher-temperature values represent how finite-temperature changes in the crystal structure and dimer geometries impact the transfer integrals. As evidenced by the comparison between the "No QHA" and 0 K data, the crystal expansion induced by zero-point vibrational effects decreases the J_{eff} appreciably. contributions while still neglecting thermal expansion. NO QHA $\rightarrow$ 0K shows the most significant reduction in J_{eff} which is consistent with this transition being the largest single increase in volume. The reduction then accelerates from 0K $\rightarrow$ 300K coinciding with the acceleration of lattice thermal expansion.

Angled points in Figure 5 indicate transfer integrals evaluated via fixed cell optimized experimental structures. A reverse in the trend at 200K can be seen for the C dimer. This is due to errors in the simulated high temperature β angle. Experimentally, this angle widens to increased orbital overlap despite the growing lattice parameters. This is untrue for the predicted structure, whose angle remains relatively constant causing all expansion in the a direction to result in increased distance between the pair, causing a decrease in J_C^{eff}.

The overall reduction in magnitude of the 3 primary transfer integrals is quite significant from the electronic minimum to 300K range. The largest absolute decrease was in the J_A^{eff} pair, whose constituent molecules lie on lattice points along cell vector b. J_C^{eff}, however, sees the most significant percentage decrease in hole transfer, reducing by 56% at 300K. This indicates that while thermal expansion universally decreases hole transfer by

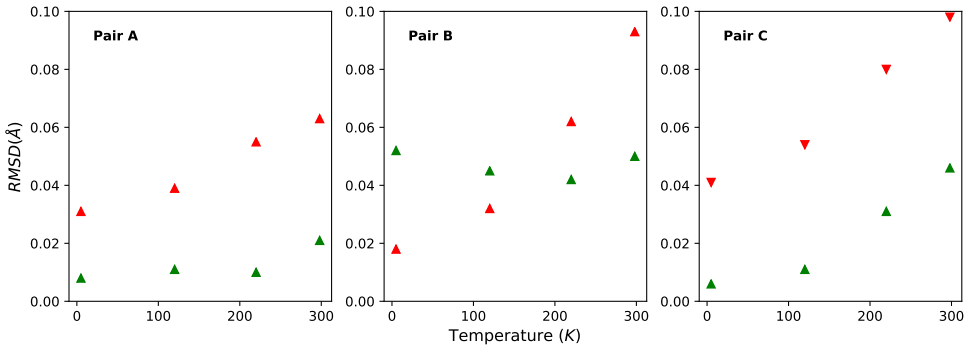

Figure 5.5: RMSDs of atomic positions in the dimers with respect to those pulled from the experimental unit cell. Comparisons were done for the fully optimized unit cell at 0K (red) and the QHA-determined finite temperature cells (green).

driving intermolecular separation, the relative impact is highly dependant on the type of packing pattern in that direction. The cofacial dimer saw only a 19% (A) reduction in the magnitude of the transfer integral as opposed to 32% (B) and 56% (C) in the face-to-edge pairs.

The largest transfer integral J^A_{eff} indicates that the most efficient bulk hole mobility would lie in the b direction of the conventional cell. Predicted individual vector expansions over-expand in this direction as indicated in Figure 1a. This could lead to potential over-estimation of the transfer integral at low temperatures and under-estimation at higher temperatures. However, the non-QHA estimation of this parameter is far below experimental values, and would lead to a significantly overpredicted charge transfer in this direction.

RMSD's of the atomic positions in the three dimer pairs with respect to the experimental fixed cell optimization were also determined, as shown in Figure 5.5. The largest overall disparity was found at roughly 0.05Å in Pair B, coinciding with the green curve in

Figure 5.4. This stays relatively consistent throughout the temperature, however, providing qualitative agreement with the FC-optimized experimental crystal in this direction. Pair C, where it seems as though our model fails to capture the positive temperature dependence of J_C^{eff}, is in excellent agreement with the atomic positions at lower temperatures (accounting for a correct 5K J_C^{eff}). Due to the shape of the crystal contorting in this direction, however, the progressively worse description of the transfer integral for this pair is mirrored by the RMSD's as temperature increases. At 5K, the QHA-expanded crystal is correct within 0.006Å; this increases to 0.046Å at room temperature.

Dimer RMSD analysis was also carried out for pairs extracted from the variable cell (no QHA) optimized crystal compaired to the experimental structures. For naphthalene, T-dependent RMSD's for the VC dimers significantly outpaced the QHA-expanded counterparts at that temperature. This indicates that while our model did not correctly expand β and subsequently underestimated J, the predicted structures are more accurate. Agreement between the VC minimum and $J_C^{eff}(300)$ is fortuitous; both the interplanar angle and intermolecular separation are incorrect.

BTBT

BTBT is a monoclinic $P2_1/c$ that packs in a herringbone pattern with two primary carrier transfer directions, denoted J_A^{eff} and J_B^{eff} in Figure 5.6. The larger magnitude J_A^{eff} relies on cofacial orbital overlap, decreasing by 10.2% from the DFT optimized minumum to the predicted 300K structures. J_B^{eff}, as with the experimental naphthalene interaction

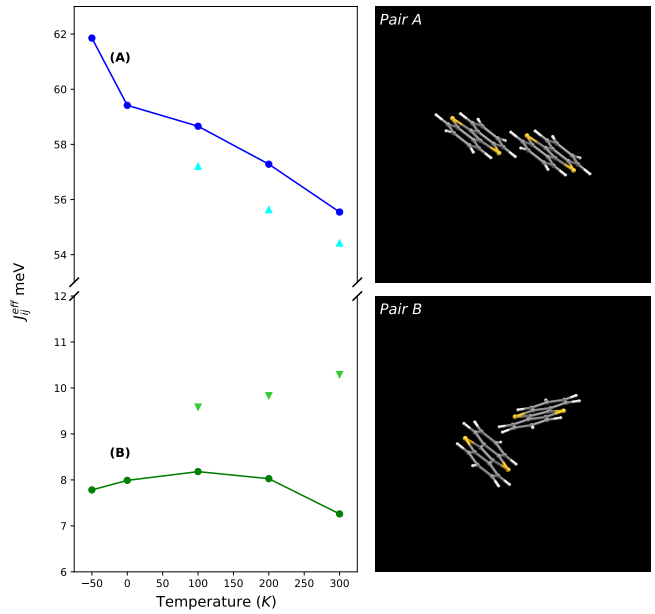

Figure 5.6: Transfer integrals as a function of temperature (left) and the corresponding dimer interaction (right) for crystalline BTBT

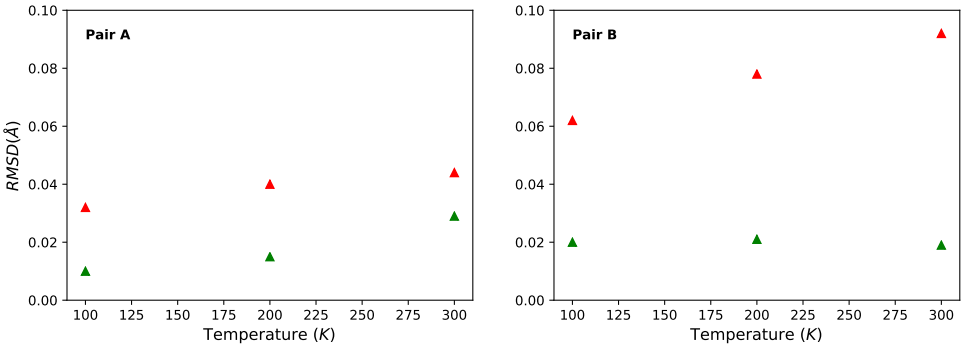

Figure 5.7: RMSD of the atomic positions for **Pair A** (left) and **Pair B** (right) if BTBT. Green points correspond to the QHA-predicted dimer positions whereas red is the DFT-predicted 0K minimum structure.

of the same form, slightly increases at lower temperatures while decreasing at intermediate to room temperature. There are two competing interactions at play: the increased distance of the two monomers (decreasing overlap) and the variation of the intermolecular angle (increasing overlap) which relies on the β lattice parameter. This results in an clear optimum temperature of the hole transfer in this direction at around 100K resulting in the interplay of these two orbital overlap descriptors.

As was done with naphthalene, fixed cell optimized dimers A and B were pulled from experimental crystals and transfer integrals were determined, as indicated by the unconnected angular points in Figure 5.6. While the reduction in J_A^{eff} is accurately modeled both in magnitude and trend, a disparity is seen at 100 $K \rightarrow$ 300 K for J_B, similar to naphthalene. Both pairs are comprised of a face-to-edge interacting dimer whose interfacial angle is dependent on predicted β.

RMSD analysis was also carried out for the BTBT dimers of interest, located in Figure 5.7. A subtle but noteable deviation from the experimental crystal dimer is found in the predicted B pair atomic structure as temperature increases. The molecular centers of mass from 100 $K \rightarrow$ 300 K drift 0.016 Å further in the predicted QHA structure while β is widened by 0.3° less compared to the same dimer from the experimental cell. This results in a similar competing contribution to the transfer integral: the value is expected to dampen as intermolecular separation increases and amplify with a narrower interfacial angle, reaching a maximum in the face-to-face (π-stacking) orientation. While the absolute differences are miniscule the sensitivity of J in the face-to-angle interactions is highly exaggerated from the face-to-face counterparts.

Pentacene

Pentacene has 3 primary transfer integrals each involving unique intermolecular interfaces as shown in Figure 5.8. Pair A and B have a staggered and aligned face-to-edge interactions, respectively, each with a comparable interfacial angle. Pair C is a staggered face-to-face orientation. As was seen with the other crystals, predicted J^{eff} experiences the most significant relative reduction in the face-to-edge pairs; J_A^{eff} and J_B^{eff} are reduced by 15.3% and 16.9%, respectively. J_C^{eff} is reduced by a modest but non-negligible 4.7%

Due to our attempt at establishing trends in the impacts of temperature on charge transport parameters as well as identifying potential shortcomings of thermally expanded structures, fixed cell optimized pentacene comparisons were omitted. Experimental finite temperature structures displayed somewhat erratic expansion (Figure 5.3), and experimental structures used in these comparisons before were performed in single studies with consistent experimental procedures.[4,13]

5.5 Conclusions

Finite temperature contributions to $G(T, P, V)$ using DFT/DFTB phonon densities of state are demonstrated to yield accurate thermal expansions of organic semiconducting crystals with comparable cost to Γ-point only approximations. For example, full QHA treatment with the method outlined here yields accurate cell volumes for naphthalene with an approximate cost of 2000 CPU hours. Full DFT supercell phonons would require an excess of 100,000 CPU hours for a similar treatment, *i.e.* five sampled volumes for

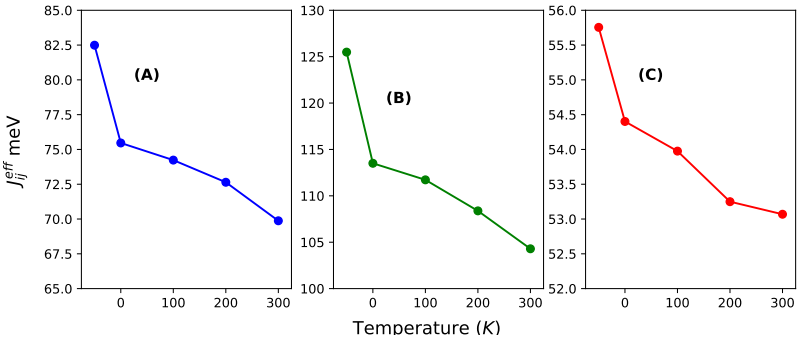

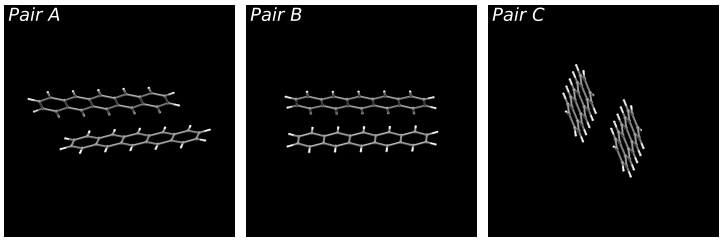

Figure 5.8: Pentacene J_{ij}^{eff} values and corresponding dimer pairs.

QHA fitting. This severely inhibits the possibility for high throughput or more complicated materials than simple anthracenes.

Evaluation of transfer integrals along cofacial interactions using QHA-predicted unit cells was demonstrated to be successful. While small errors were discovered in over- or under-prediction of cell vectors in the direction of the π-stacking and edge-to-edge interactions, corresponding transfer integrals were impacted only slightly, and the temperature evolution was correctly modeled. Complications in predicting the face-to-edge transfer integrals arose from accumulation of small errors in both lattice vector lenghts and unit cell angles. The interplay of beneficial and detrimental intermolecular orbital overlap depending on both orientation and separation became difficult to account for at $T > 100K$. This work demonstrates that while subtle, the impact of finite temperatures on the crystal structure of organic semiconductors does have considerable implications on the transport properties, and should be recognized.

Chapter 6

Photomechanical Crystal Structure Prediction

Photomechanical molecular crystals have garnered attention for their ability to transform light into mechanical work, but difficulties in characterizing the structural changes and mechanical responses experimentally have hindered the development of practical organic crystal engines. This study proposes a new computational framework for predicting the solid-state crystal-to-crystal photochemical transformations entirely from first principles, and it establishes a photomechanical engine cycle that quantifies the anisotropic mechanical performance resulting from the transformation. The approach relies on crystal structure prediction, solid-state topochemical principles, and high-quality electronic structure methods. After validating the framework on the well-studied [4+4] cycloadditions in 9-methyl anthracene and 9-*tert*-butyl anthracene ester, the experimentally-unknown solid-state transformation of 9-carboxylic acid anthracene is predicted for the first time. The

results illustrate how the mechanical work is done by relaxation of the crystal lattice to accommodate the photoproduct, rather than by the photochemistry itself. The large $\sim 10^7$ J/m^3 work densities computed for all three systems highlight the promise of photomechanical crystal engines. This study demonstrates the importance of crystal packing in determining molecular crystal engine performance and provides tools and insights to design improved materials *in silico*.

6.1 Introduction

Organic photomechanical crystals transform light into mechanical work via the changes in solid-state structure that result from a photochemical reaction.[260] These structural changes can induce elongation, bending, twisting, photosalience, and other behaviors.[71,261–263] While numerous examples of photomechanical behaviors can be found in the literature,[35,264–271] a predictive understanding of the relationships between molecular structure, crystal packing, photochemical transformation, and the mechanical work output remains elusive. Such understanding is vital for the rational design of photomechanical engines based on molecular crystals.

In principle, determining the work output of a light-induced crystal-to-crystal transformation should be straightforward. In practice, photomechanical crystals present specific challenges that have so far prevented the development of a comprehensive theoretical framework. First, it is often difficult to determine the structure of the product crystal after photoreaction. Performing solid-state photochemical reactions in bulk crystals often causes them to shatter, complicating diffraction experiments.[?,35,272] If the photoproduct

absorbs strongly at the excitation wavelength (positive photochromism), then a photostationary state is reached and complete conversion is impossible. To circumvent this problem, one might isolate the photoproduct in solution and recrystallize it. Unfortunately, the product crystal grown in this manner may have a different crystal packing from that formed by direct photoconversion in the solid-state.[273] Finally, if the reaction is thermally reversible (T-type), the photoproduct may be too short-lived for practical structure determination.

Even if the photoproduct crystal structure can be determined experimentally, this leads to a second, more fundamental challenge: how does the transformation from the reactant to the product crystal actually occur? As with gas expansion cycles in thermodynamics, this process should consist of a series of well-defined steps, each of which can be associated with an energy change. To simplify the problem, we will concentrate on complete conversion of the reactant to product that gives rise to crystal expansion and contraction. It should be noted that the most commonly reported mode of photomechanical crystal actuation involves bending due to partial conversion that yields a reactant-product bimorph structure.[274–276] In principle, a bending crystal can be divided into subdomains that undergo expansion/contraction after complete conversion, so this approach should be general and adapatable to bending as well.

The significant experimental and conceptual challenges in this field motivated us to turn to computational chemistry to predict the structures, transformations, and properties of photomechanical crystals entirely from first-principles. Organic molecular crystal structure prediction has advanced considerably in recent years, thanks in large part to the development of accurate and computationally efficient electronic structure models for the solid

state,[96,105,277,278] which have considerably enhanced researchers' abilities to predict the thermodynamically most stable polymorphs.[63,65,66,68,97,98,120,143,155,158,160,161,163,279–284] As a result, successful examples of crystal structure predictions in the Blind Tests,[29,30,153] pharmaceuticals,[159,164,285–287] and organic materials[288–295] are accumulating rapidly.

Successful application of crystal structure prediction to photomechanical crystals would enable first-principles design and optimization of this promising class of materials. Unfortunately, this effort faces two major challenges. First, instead of generating the landscape of candidate structures for a single species, as in traditional crystal structure prediction, predicting a solid-state photomechanical response requires understanding the structures and transformations between two distinct crystal energy landscapes (reactant and product). Second, energetic stability cannot be the primary criterion for identifying the photochemical polymorph produced by the solid-state reaction. High photon energy and the steric constraints created by the solid-state reaction environment can drive the reaction toward a high-energy, thermodynamically metastable product.[42] In other words, the conventional crystal structure prediction goal generating a modest number of low-energy polymorphs is replaced by the challenge of identifying the relevant structure(s) from a much larger pool of higher-energy candidate structures.

Here, we develop a new, first-principles methodology for predicting solid-state molecular crystal photomechanical transformations that overcomes these difficulties. It generates structures using crystal structure prediction, employs a crystalline topochemical hypothesis to predict the solid-state photochemical transformations, and establishes a photomechanical engine cycle that characterizes the anisotropic work produced by the

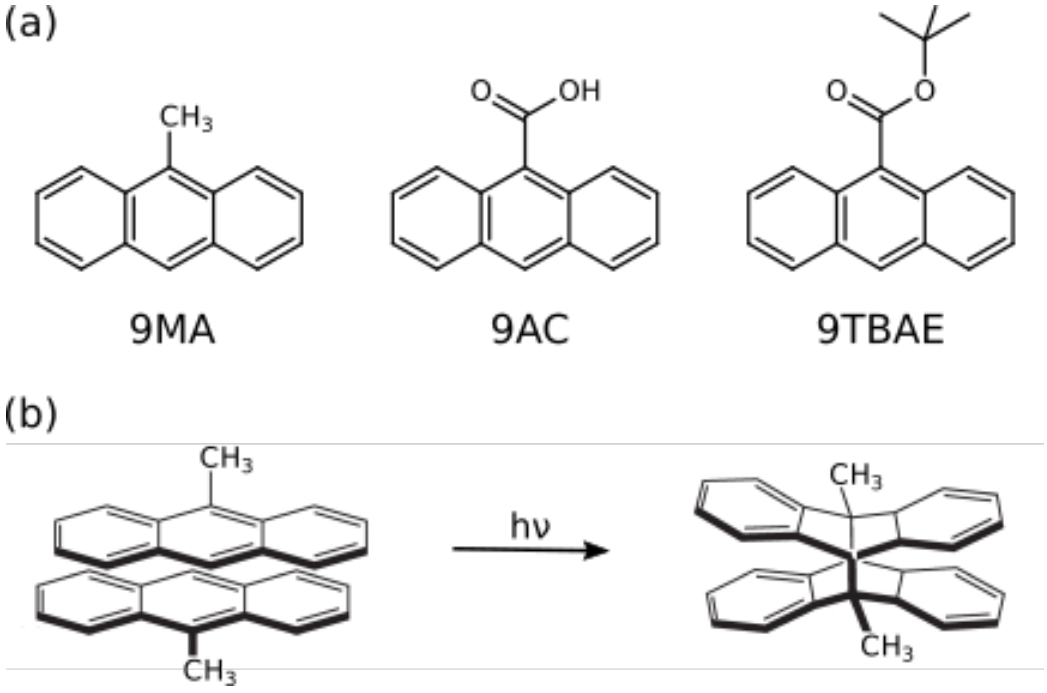

Figure 6.1: (a) Structures of 9-methyl anthracene (9MA), 9-anthracene carboxylic acid (9AC), and 9-*tert*-butyl anthracene ester (9TBAE). (b) [4+4] photodimerization reaction of 9MA. The solid-state photochemical transformations have been established experimentally for 9MA and 9TBAE, but not for 9AC.

structural changes. This theoretical approach is validated on two well-characterized [4+4] anthracene derivative photodimerization systems (9MA and 9TBAE, Figure 6.1). This negative photochromic reaction permits complete conversion of the crystals to a stable photodimer form, avoiding mixtures and facilitating comparison to theory. We also use the theory to predict the photodimer crystal structure of a T-type reversible crystal (9AC) that has not yet been measured experimentally but may be more practical for actuator applications. The large $\sim 10^7$ J/m^3 work densities computed for all three systems demonstrate the exceptional promise of organic molecular crystal engines. Moreover, our findings demonstrate how molecular crystal packing plays a key role in determining the anisotropic work

generated, emphasizing the value of theoretical tools capable of characterizing the stress and strain generated in these transformations.

6.2 Methods

Crystal Structure Prediction for 9MA: After optimizing the gas-phase monomer and photodimer structures using B3LYP/6-311+G(d)[296] in Gaussian09,[255] candidate crystal structures for the monomer and photodimer were generated from first-principles via a hierarchical crystal structure prediction protocol. For each species, 55,000 crystal structures from 11 common space groups were randomly generated using PyXtal,[84] assuming a single molecule in the asymmetric unit (Z'=1). These crystal structures were relaxed using the Generalized Amber Force Field (GAFF)[85] in CHARMM 45b2[86] and clustered to eliminate duplicates.

Next, all 281 monomer crystal structures lying within 10 kJ/mol of the lowest-energy structure, and all 255 photodimer crystal structures within 25 kJ/mol were further relaxed with the semi-empirical HF-3c method[70] as implemented in CRYSTAL17.[83] The higher energy cutoff for the photodimer landscape was chosen due to the relative sparsity of structures compared to the monomer landscape and the expectation that the SSRD could lie relatively high in energy. HF-3c refinement and another round of structure clustering reduced the landscape to 63 monomer structures within 10 kJ/mol and 42 photodimer structures within a 15 kJ/mol energy window. Final refinement of those crystal structures was performed using planewave density functional theory (DFT), using the van der Waals-corrected B86bPBE-XDM functional[77,78,211] in QuantumEspresso.[210]

Energy relationships between the monomer and photodimer landscapes were computed according to,

$$2\ \text{9MA} \longrightarrow\ (\text{9MA})_2. \tag{6.1}$$

However, conventional density functionals used in solid-state calculations describe the anthracene photodimerization poorly.[42,58–60] The issue stems from delocalization error in the approximate density functionals,[61] which artificially stabilizes extended π delocalization found in the anthracene monomer by dozens of kJ/mol relative to the photodimer with sp^3-hybridized carbon centers and more localized electron density (Figure 6.1).[42,59,60] Issues arising from DFT delocalization error have been identified in a number of other organic crystals as well.[62–69]

To address the delocalization error issues inherent in B86bPBE-XDM (and other density functionals) for these systems, an intramolecular correction is applied to all periodic DFT lattice energies. This single-point energy correction replaces the intramolecular energies of the monomer or photodimer with more accurate ones computed at the spin-component-scaled dispersion-corrected second-order Møller-Plesset perturbation theory (SCS-MP2D)[60] level,

$$E_{crystal} = E^{DFT}_{crystal} + \sum_{i=1}^{Z} \left(E^{SCS\text{-}MP2D}_{molec,i} - E^{DFT}_{molec,i} \right) \tag{6.2}$$

The molecular energies on the right-hand side are computed in the gas-phase using geometries extracted directly from the DFT-optimized crystal. The sum runs over all Z molecules in the unit cell, though space group symmetry can be exploited to compute the

gas-phase molecular energies only for the molecules in the asymmetric unit. This correction has been employed successfully in several other systems.[42,66–68] SCS-MP2D reproduces the benchmark coupled cluster single, doubles, and perturbative triples (CCSD(T)) anthracene photodimerization reaction energy to within 1.2 kJ/mol.[60] Further computational details regarding the crystal structure prediction procedure are outlined in **Section 2.6**.

Topochemical Identification of the Solid-State Reacted Structures: Characterizing the photomechanical transformation and the associated work performed requires identifying the solid-state reacted dimer (SSRD) crystal structure which results from the solid-state reaction. This is done topochemically, replacing the reacting monomer pairs in the monomer crystal structure with photodimers placed at the same center of mass positions and oriented to maximize overlap with the original monomer pair according to the following algorthim:

1. Identify the reacting monomer pair based on having the shortest center-of-mass distances.

2. Extract the Cartesian coordinates of the monomer pair from the crystal and orient it to align its principle axes of inertia along the Cartesian xyz axes.

3. Construct the gas-phase photodimer (e.g. via gas-phase DFT geometry optimization), and orient it based on its own principle axes of inertia.

4. Perform an initial alignment of the monomer pair and photodimer by applying all possible inversion and reflection symmetry operations to the photodimer to determine which operation(s) minimize the root-mean-square deviation (rmsd) in atomic coor-

dinates between the monomer and the photodimer. To avoid issues with aspects such as methyl rotations, hydrogen atoms are excluded from the rmsd calculation.

5. Optimize the alignment between the monomer pair and photodimer by rotating the photodimer about its three Cartesian axes to minimize the heavy-atom rmsd with respect to the monomer pair (i.e. performing three 1-D optimizations).

6. Once the optimal overlap between the monomer pair and photodimer has been found, rotate the resulting photodimer dimer coordinates into the monomer's original axes of inertia coordinate frame.

7. Translate the dimer to the original monomer pair center-of-mass location.

8. Apply space group symmetry operations to populate symmetry-equivalent molecules in the unit cell.

Constrained DFT geometry optimization of the replaced molecules within the fixed monomer lattice parameters produces the "proto-SSRD," while subsequent variable-cell relaxation produces the equilibrium SSRD structure. Similarly, one can construct the "proto-Monomer" for the reverse dissociation reaction by substituting monomers into the photodimer unit cell.

Work Density Calculations: The elastic work density is evaluated from the DFT-computed Cartesian stress (σ) and strain (ϵ) tensors for the proto-SSRD/proto-Monomer relative to their fully-relaxed equilibrium structures. Tight DFT geometry-optimization criteria were employed to improve convergence of the stress and strain tensors. The orientational dependence of the work density was computed by projecting it onto different

crystallographic directions defined by the unit vector $\hat{n}$.

$$W(\hat{n}) = \frac{1}{2}\hat{n}^{\intercal}\sigma\epsilon\hat{n} \tag{6.3}$$

After scanning over all directions $\hat{n}$, the absolute value of the work densities are plotted as a heat map on the surface of a sphere. Examination of the 9MA proto-SSRD relaxation finds the stress to vary nearly linearly with strain, supporting the assumption of elastic work. See **Section 2.7** for further details.

6.3 Results and Discussion

6.3.1 1. Crystal structure prediction of key intermediates for the photomechanical cycle

The crystal energy landscape for photomechanical materials based on the anthracene [4+4] photodimerization will typically contain at least three notable structures: the reactant crystal, a polymorph of the photochemical product crystallized from solution (referred to as the solution-grown dimer, or SGD), and the SSRD polymorph generated through the solid-state crystal-to-crystal photochemical reaction. The SSRD is central to the photomechanical process, and we hypothesize that the SGD and SSRD crystal structures will match only in rare cases. Our first task is to identify and characterize these structures. The monomer reactant and SGD product will frequently be the thermodynamically most stable polymorphs on their respective landscapes, while the SSRD lies quite a bit higher in energy.

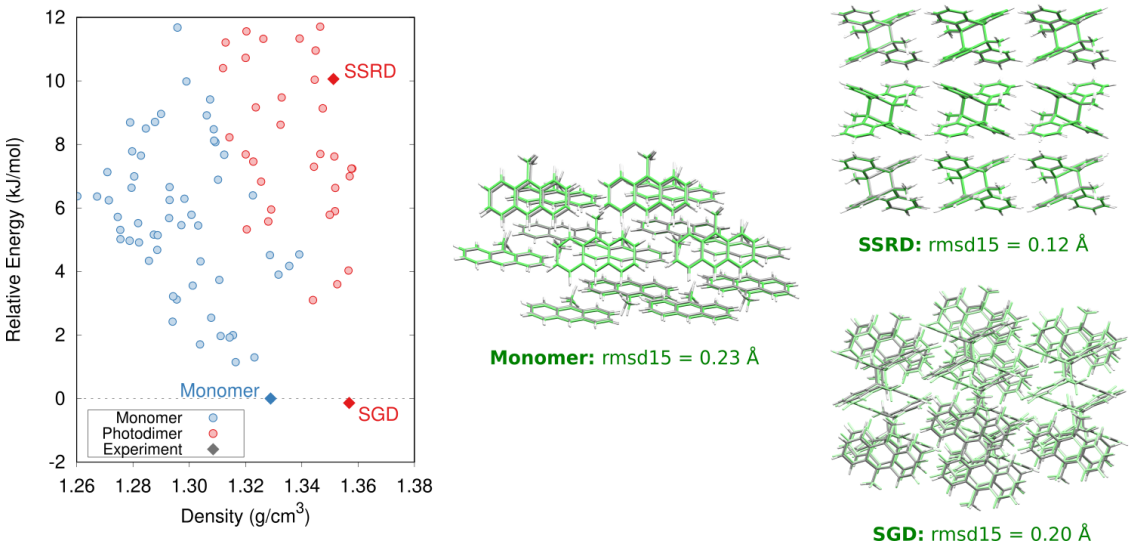

Figure 6.2: Predicted crystal energy landscape for the 9MA monomers and photodimers after DFT refinement and the single-point intramolecular SCS-MP2D energy correction. The monomer, SGD, and SSRD structures are indicated. Overlays comparing the predicted (green) and experimental (gray) monomer, SGD, and SSRD structures, along with their corresponding rmsd15 values are also shown.

A) 9MA

For 9MA, the initial force-field-level crystal structure prediction landscapes contain the experimental monomer and SGD structures, though the monomer lies ∼6 kJ/mol higher than the most stable predicted monomer crystal, while the SGD is the second-most stable form on its landscape at +0.1 kJ/mol. However, further refinement of the landscapes with increasingly accurate levels of theory shifts the 9MA monomer and SGD to become the global minimum energy structures on their respective crystal structure landscapes (**Figures 6.3** and **6.4**). After correcting for the ∼60 kJ/mol intramolecular DFT delocalization error with SCS-MP2D according to Eq 6.2, the monomer and SGD crystals become nearly isoenergetic (Figure 6.2).

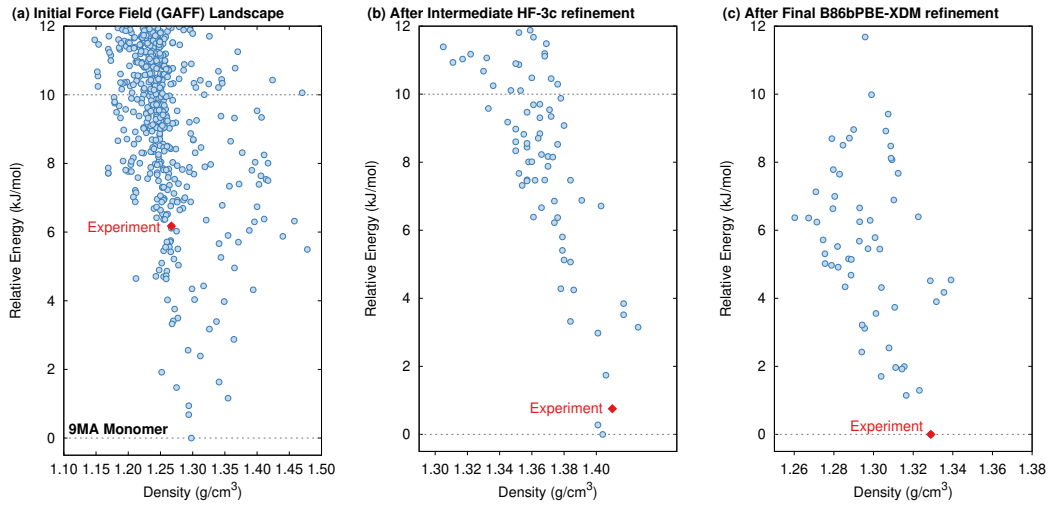

Figure 6.3: Evolution of the crystal structure prediction landscape for 9MA monomer. (a) Initial GAFF-generated landscape, (b) after refining with HF-3c, and after the final B86bPBE-XDM DFT refinement. Structures lying within 10 kJ/mol of the lowest-energy structure (gray line) were carried forward to the next stage. The experimental crystal structure is indicated in red.

The predicted monomer and SGD structures match the experimentally reported crystal structures[297] with excellent overlaps of 0.20–0.23 Å using the 15-molecule cluster root-mean-square deviation (rmsd15) metric (Figure 6.2).[298] The DFT unit cell parameters for the 9MA monomer and SGD are only 1.2% smaller than the experimental ones on average (Appendix TableA.1), which is consistent with the underestimation of unit cell volumes expected for comparing 0 K DFT calculations to room-temperature experimental structures.[113]

While the ability to predict the thermodynamically most stable polymorphs of 9MA and its photodimer correctly is important, understanding the crystal-to-crystal transformation associated with the photomechanical response also requires identifying the SSRD polymorph on the photodimer crystal energy landscape. Energetic stability alone cannot be used as a criterion for the SSRD, since the constraints of the solid-state reaction envi-

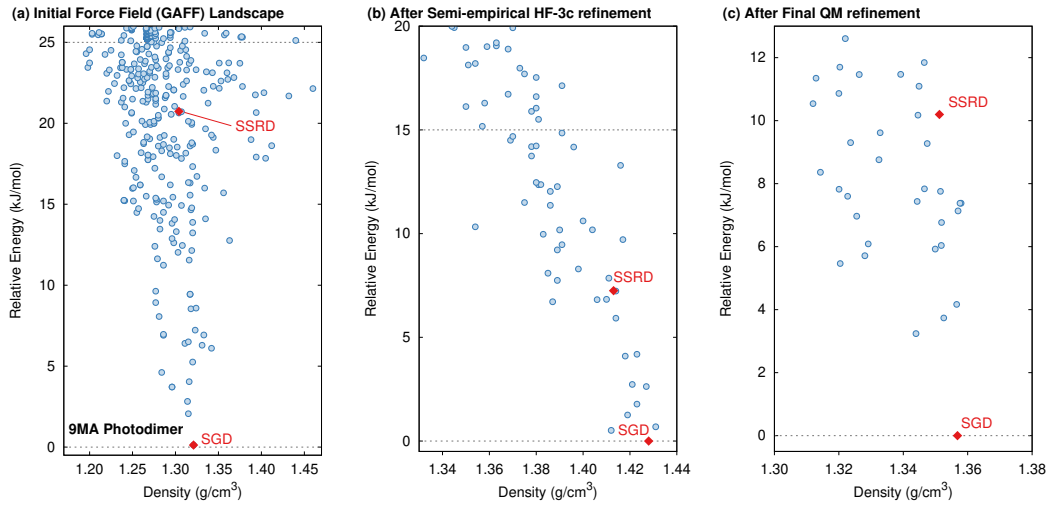

Figure 6.4: Evolution of the crystal structure prediction landscape for 9MA photodimer. (a) Initial GAFF-generated landscape, (b) after refining with HF-3c, and after the final B86bPBE-XDM DFT refinement. Structures lying within 25 kJ/mol of the lowest-energy structure (gray line) on the GAFF landscape were carried forward to the HF-3c refinement stage; structures lying within 15 kJ/mol on the HF-3c landscape were carried forward to the final DFT refinement. The experimental SGD and SSRD crystal structures are indicated in red.

ronment can produce an SSRD that is highly metastable.[42] A similar focus on high-energy structures occurs when predicting structures of porous organic materials,[291,292,295] though there it stems from the models' omission of guest/solvent molecules which stabilize the pores experimentally.

A key conceptual advance in this paper lies in extending the topochemical principle to the problem of predicting the photoproduct crystal structure, rather than just the photoproduct molecule by itself. Solid-state anthracene [4+4] photodimerization reactions only occur when the reactive carbon atoms lie within 4.2 Å and satisfy various orientational constraints.[14,299,300] Moreover, the steric constraints imposed by the crystalline lattice limit molecular reorganization after the photochemical transformation, thereby constraining the photoproduct crystal structure and inhibiting its relaxation to the lowest-energy SGD pack-

ing. Therefore, instead of relying on an energetic stability criterion, we identify the SSRD based on the crystal packing relationships that connect structures between the monomer and photodimer crystal energy landscapes.

Specifically, we predict the product of the crystal-to-crystal transformation with no experimental information by generating an initial topochemical SSRD crystal in which the reacting monomer pairs in the predicted monomer crystal are replaced by photodimer molecules having the same positions and orientations. Constrained DFT relaxation of this crystal structure with the lattice vectors held fixed at their monomer crystal values produces the proto-SSRD. Subsequent unconstrained relaxation of the proto-SSRD atoms and lattice vectors produces the final equilibrium SSRD structure. Applying this procedure to 9MA (Figure 6.5a), we find that the SSRD retains the same $P2_1/c$ space group as the reactant monomer crystal, and it matches the rank #27 structure on the DFT photodimer crystal structure prediction landscape (Figure 6.2) with an excellent rmsd15 overlap of 0.14 Å.

Determining the 9MA SSRD crystal structure experimentally is difficult, since bulk crystals fracture after about ∼30% photodimerization under ambient conditions.[40] Turowska-Tyrk and coworkers recently showed that photodimerization of single 9MA crystal can be carried to completion without fracture at elevated pressures in a diamond anvil cell.[14] The SSRD structure predicted here (at 0 GPa) is an outstanding match for the experimental X-ray crystal structures reported at 0.1 and 0.4 GPa, with rmsd15 values of only 0.12 Å (Figure 6.2).

Morimoto et al. observed that single microcrystal plates could expand by a factor of 1.07 along their c-axis while remaining intact.[301] Presumably, these crystals also

adopt the SSRD structure after conversion. To confirm this, we performed powder X-ray diffraction (PXRD) experiments on 9MA microplates after photodimerization. Figure 6.6 compares the experimental PXRD pattern with a simulated one for the predicted SSRD structure. The microplates were not powdered, so their relative peak intensities are different from those in the calculated PXRD pattern. Peak positions match within 0.2 degrees, which is reasonable given the differences in volumes between the different experimental pressures and the 0 K DFT calculations. Furthermore, the peaks with enhanced intensity at 10.6 degrees corresponds to the 001/100 Miller planes, which lie parallel to the *bc* crystal plane and thus horizontal along the substrate. The preferred orientation of the crystals should lead to enhanced intensity of this peak, as observed. Interestingly, after photoconversion the experimental PXRD pattern disappears over the course of 1 hour as the plates become mostly amorphous (Appendix FigureA.1). This rapid loss of the SSRD structure suggests that it is highly unstable. Previously, we observed that 9MA powders appeared to transform directly from monomer to the SGD photodimer structure.[274] We suspect that the sample preparation process used in that work, which involved grinding the crystals after UV irradiation, facilitated the SSRD-to-SGD transition and caused us to miss the presence of the SSRD intermediate. All these observations are consistent with the SSRD being a high-energy polymorph that can be stabilized by the application of mechanical pressure.

The 9MA monomer to SSRD structural transformation is anisotropic: the cell contracts 2.6% and 3.7% along the a and b crystallographic axes, but it expands by 5.9% along c and the monoclinic angle β increases by 3.2% (Figure 6.7a). The calculated expansions and contractions are slightly less than observed experimentally in the 9MA microplates,[301]

which may be a consequence of temperature effects since the calculations were done at 0 K. The large elongation along the c axis stems from an increase in lateral spacing between photodimers, rather than from the butterflying of the anthracene rings upon photodimerization. Energetically, the SSRD lies a rather large 10.1 kJ/mol above both the monomer and SGD crystal structures. Previous polymorphism surveys suggest that only ∼1–3% of polymorph pairs differ by 10 kJ/mol or more, and such large energy differences are even less common for rigid molecules such as 9MA and its photodimer.[42,92,93]

Overall, both crystal structure prediction and the *in silico* topochemical SSRD formation approach independently produce the same SSRD structure. The topochemical approach identifies the SSRD based on its relationship to the monomer crystal, while full predicted crystal energy landscape of the photodimer provides confirmation of that structure and its energy relative to other observed and/or predicted photodimer polymorphs. Together with the successful prediction of the monomer and SGD crystals, these results demonstrate that the important 9MA crystal structures and the solid-state photochemical transformation can be predicted entirely from first-principles.

B) 9TBAE

Next, we further validate our crystalline topochemical approach by determining the solid-state photochemical transformations in 9TBAE. For simplicity, we omit the full crystal structure prediction steps. Instead, we start from the experimentally-known monomer crystal structure, relax it with DFT, and then predict the associated topochemical SSRD structures.

Previous NMR crystallography work established the structure of the 9TBAE SSRD as an ensemble of six, closely related and dynamically interconverting structures that differ only subtly in the torsional angles of the *tert*-butyl groups.[302] Applying the topochemical approach to the 9TBAE monomer (Figure 6.5b) predicts a $P2_1/n$ SSRD structure that is similar to those six structures identified in the earlier study. Although the topochemical SSRD here retains the monoclinic symmetry of its parent monomer crystal, it overlaps with the six experimentally inferred orthorhombic structures with rmsd15 values around 0.4 Å. Further confirmation of the topochemically-predicted SSRD comes from the X-ray diffraction structure for a partially photodimerized 9TBAE crystal.[273] Extracting photodimer components from that partially-reacted experimental structure and relaxing them with DFT produces a $P2_1/n$ symmetry structure in excellent agreement with the topochemically predicted one (rmsd15 = 0.11 Å).

Structurally, solid-state photodimerization of 9TBAE induces a much larger unit cell change than 9MA (Figure 6.7). The 9TBAE unit cell expands 6.0% along the a axis, largely due to the butterflying motion of the anthracene rings. Simultaneously, the monomers sliding into register as they photodimerize leads to an 7.3% contraction along the b axis. The c and β lattice parameters change only slightly, and the net volume change is small. These structural changes are consistent with the mechanism and magnitudes of nanorod elongation observed previously.[35,44]

C) 9AC

Now consider monoclinic 9AC. Structural characterization of its SSRD has proved experimentally infeasible to-date due to the short photodimer lifetimes (seconds to min-

utes),[74,303] which makes theoretical predictions essential to understanding the transformation. Figures 6.5c and 6.7c show the topochemically-predicted crystal transformation. Whereas the photodimerizations of 9MA and 9TBAE both involve substantial elongation along a crystallographic axis, monoclinic 9AC exhibits only modest changes in the a, b, and c lattice parameters. Instead, the major transformation occurs via the 7.3% decrease in the β angle.

The one-dimensional stacking geometry in the 9AC crystal is qualitatively different from the herringbone geometry seen in 9MA and 9TBAE. This leads to a very different morphology change. The lack of extension along a major crystal axis probably explains why it has been more difficult to detect length changes for 9AC nanorods, although bending and twisting are much more readily observed.[34,303,304]

6.3.2 2. Photomechanical engine cycle

Now that the photochemical structural transformations are understood for all three systems, we need a conceptual framework to predict the work output. We establish an idealized four-step photochemical engine cycle (Figure 6.8) that enables characterization of the work that could potentially be performed by a given material:

1. The cycle begins with an "instantaneous" and complete solid-state photodimerization of the monomer species, converting the equilibrium monomer crystal to the proto-SSRD. The proto-SSRD retains the monomer unit cell parameters and is therefore highly strained.

2. The proto-SSRD relaxes to its equilibrium geometry. The associated stress release transforms the crystal structure anisotropically and produces "forward" mechanical work.

3. The photodimer dissociates to a strained proto-Monomer—the monomer packed within the SSRD lattice parameters.

4. The proto-Monomer relaxes back to the original equilibrium monomer crystal structure, producing mechanical work in the "reverse" direction.

In other words, chemical transformation creates the strained crystalline state, and relaxation of the associated stress produces work. Although the lattice parameter changes in Step 4 exactly mirror those from Step 2, the work performed in the forward and reverse directions will differ because the stress/elastic constants differ between the proto-SSRD and proto-Monomer. In practice, this means that a photomechanical engine can perform net work similar to a traditional Carnot cycle based on gas expansion/compression. In the case of a photomechanical crystal, the input photon(s) act as an effective high temperature bath.

It is important to emphasize that real-world photomechanical crystals are expected to deviate from this idealized photochemical engine cycle. First, the solid-state photodimerization process does not occur instantly. Nevertheless, Raman spectroscopy experiments in certain photomechanical crystals suggest that the photochemical reaction and resulting crystal-to-crystal transformation do largely precede the relaxation of the unit cell.[305,306]

Second, the solid-state photochemical reaction may not always reach 100% completion, whether due to positive photochromism or crystal packing reasons. For example, photodimerization within the one-dimensional monomer stacks in monoclinic 9AC occurs

stochastically and only reaches ∼75% completion, with the remaining monomers becoming isolated and unable to react.[304,307] Crystal defects, impurities, and the experimental light source can also impact the extent of reaction.

Third, many photomechanical processes are not reversible in practice. For example, the 9MA SSRD transforms to an amorphous material instead of reverting back to the monomer (Appendix FigureA.3), while the 9TBAE SSRD slowly converts to the SGD.[273] On the other hand, 9AC photodimerization is thermally reversible on the timescale of minutes.[304] In other photochromic and photomechanical crystals, the reverse reaction can be triggered via a different wavelength of light[308,309] or external pressure.[310]

Despite these caveats, the idealized photomechanical engine cycle presented here provides a useful framework for quantifying the nature and magnitude of work that could hypothetically be performed by the system and for comparing the photomechanical responses of different materials.

6.3.3 3. Photomechanical performance

Having defined the photomechanical engine cycle, we analyze the photomechanical performance of 9MA, 9TBAE, and monoclinic 9AC. There are several different energies that are involved in the photomechanical cycle. We first consider the energetics of the photochemical reaction itself. The computed solid-state photodimerization reaction energies differ significantly across 9MA, 9TBAE, and 9AC. 9MA photodimerization is the least endothermic at 10.1 kJ/mol. For 9TBAE, the photodimerization energy increases to 32.1 kJ/mol, reflecting the steric penalty of the bulky *tert*-butyl ester groups. The 9TBAE

SSRD is computed here to lie 12.0 kJ/mol above the SGD, similar to what was found previously.[42] On the other hand, the 101.2 kJ/mol photodimerization energy for monoclinic 9AC is several-times larger than the other two systems. The constraints of maintaining the hydrogen-bonded tetramer units within the 9AC lattice make this solid-state reaction energy even larger than the already endothermic 9AC gas-phase photodimerization.[74] The highly endothermic forward reaction in 9AC could imply a relatively small reverse reaction thermal barrier in accord with the Hammond postulate. This might explain why 9AC photodimerization is thermally reversible, unlike 9MA and 9TBAE. However, detailed investigation of the reaction kinetics is beyond the scope of the present study. In any case, all of these endothermic reaction energies are small relative to the 300 kJ/mol energy input provided by the 400 nm photons driving the dimerization.

In our photomechanical engine framework, the actual mechanical work is done not by the photoreaction, but by the subsequent relaxation of the crystal lattice to accommodate the newly formed photoproduct. Figure 6.9 presents the energies for each step of the cycle in each species, while Figure 6.10 plots the corresponding anisotropic work densities for the forward photodimerization (Step 2) and reverse dissociation (Step 4) portions of the engine cycle.

Consider first the forward photodimerization process in 9MA. The proto-SSRD lies 21.9 kJ/mol above the equilibrium monomer crystal. Relaxation of the proto-SSRD unit cell to its equilibrium geometry stabilizes it by 11.8 kJ/mol (for a net reaction energy of 10.1 kJ/mol). Figure 6.10a plots the computed elastic work produced by relaxation of the proto-SSRD. The maximal 25.0 MJ/m^3 work density occurs roughly along the c axis,

which is unsurprising given the large 5.4% elongation in that direction. Much less work is produced by the smaller contractions along the a and b axes.

While 9MA does not exhibit solid-state photochemical reversibility experimentally, we can examine what would happen if it completed the photomechanical engine cycle. The proto-Monomer formed via dissociation within the photodimer unit cell lattice parameters is 0.7 kJ/mol more stable than the SSRD, and it relaxes 9.4 kJ/mol back to the original monomer unit cell. So while the lattice parameter changes upon dissociation mirror those from the photodimerization, the smaller stress and relaxation energy associated with photodimer dissociation translate to a maximum elastic work density of only 12.3 MJ/m^3 for Step 4 of the engine cycle (Figure 6.10b) that is half as large as the forward (Step 2) work.

9TBAE exhibits somewhat larger energy changes than 9MA throughout the engine cycle (Figure 6.9). At the same time, the maximum forward-direction work density of 46.7 MJ/m^3 for 9TBAE (Figure 6.10c) is nearly double that of 9MA. Notably, the 6.0% expansion along the a axis produces far more work than the 8.5% contraction along the b. The a expansion reflects the bending out of the anthracene rings, while the b contraction stems from the energetically "softer" compression of the void space created as the monomer units slide into register to react.

As noted earlier, photodimerization of monoclinic 9AC is highly endothermic. The proto-SSRD lies 119.1 kJ/mol above the monomer, compared to 21.9 and 61.0 kJ/mol for 9MA and 9TBAE, respectively. However, the 17.9 kJ/mol relaxation energy of the 9AC proto-SSRD is intermediate between that of 9MA (11.8 kJ/mol) and 9TBAE (31.5 kJ/mol). Correspondingly, the maximal work density of 30.1 in the forward direction is closer to

that of 9MA than that of 9TBAE (Figure 6.10e). Whereas the maximal work density for 9MA and 9TBAE is performed along a crystallographic axis, the maximal work density in 9AC occurs in between the a and c axes—it stems largely from the 7.3% contraction of the β angle upon photodimerization. As for 9MA, the reverse work resulting from the photodimer dissociations in 9TBAE and 9AC are substantially smaller than for the forward photodimerizations (Figure 6.10d,f).

Taken together, these results reveal several important features of these photomechanical crystals: First, the model predicts photomechanical crystal work densities of $\sim 10^7$ J/m^3, which is several orders of magnitude larger than the the experimental work densities of photomechanical polymers.[270] Second, the work resulting from the photodimerization is roughly double that produced by the dissociation. This reflects how the anthracene monomer crystals deform much more readily (i.e. with less stress) than the photodimer ones. Third, the anisotropic structural changes produce work that is also highly anisotropic. This highlights the importance of crystal morphology and orientation for device performance. Fourth, the amount of the work performed by a switchable photomechanical material cannot always be inferred from the crystallographic change in lattice parameters (strain) alone; the stress component of the work also depends significantly on the molecular packing. This is evident in the disparities seen for the 9TBAE work densities along the a and b axes and in the differences between the forward and reverse directions for all three systems. Fifth, the reaction energetics are somewhat decoupled from the amount of photomechanical work performed. 9AC photodimerization is much more endothermic than the other two species, but 9TBAE can perform considerably more mechanical work. This suggests that it may be

possible to design materials that tune the reaction reversibility and the photomechanical work semi-independently.

6.3.4 Future Prospects for Rational Design

Looking forward, the techniques described here create, for the first time, the opportunity to design new photomechanical derivatives *in silico*. To do so, one might perform crystal structure prediction for a series of reactant species to identify the most stable crystal structure(s), the potential for polymorphism,[157] and to what extent the stable crystal packings satisfy topochemical constraints for the desired solid-state reactions.

Assuming that the photochemistry is not prevented by steric or excitonic effects in the crystal, the photochemical transformation and mechanical properties can be computed inexpensively from the reactant crystal structures, as demonstrated here for 9TBAE and 9AC. Anisotropic work density calculations can provide guidance on the potential performance of a material and how one should design an actuator that maximizes the work performed for a desired task. For example, to lift an object from below using a linear actuator, one might focus on forward expansion work and let gravity facilitate the reverse contraction process. On the other hand, linear contraction work could be used to lift an object from above. From Figures 6.7 and 6.10, we can see that the same crystal can be used for both types of work simply by changing its orientation with respect to the load. For the most promising species, one might obtain further insights into the viability, stability, and reversibility of the system by exploring the full crystal energy landscape of the photoproduct and assessing the reaction energetics and structural relationships among different photoproduct polymorphs (e.g. SSRD vs. SGD).[42,74]

6.4 Conclusions

This study demonstrates how solid-state photochemical transformations in organic crystals can be predicted entirely from first principles. It addresses several long-standing challenges surrounding the design of solid-state photoswitching and photomechanical systems, including the difficulties associated with determining the crystal structures of the photoproducts, with anticipating how changes to molecular structures will impact the crystal structures, and with understanding how crystal structure determines the mechanical response properties. The proposed photomechanical engine cycle provides a framework for characterizing the anisotropic photomechanical responses in these systems. It can be used to identify which crystal orientations or morphologies can best exploit the work produced by the photochemical transformation and to compare the potential for photomechanical work across different materials.

While the present study focuses on anthracene-based crystals, these same techniques can readily be applied to other solid-state photoswitching crystals, such as azobenzenes and diarylethenes. The detailed atomistic pictures generated with these techniques could also provide the foundation for multiscale models[270] that could predict photomechanical behaviors in nanoscale actuators and would facilitate the development of practical organic crystal engines.

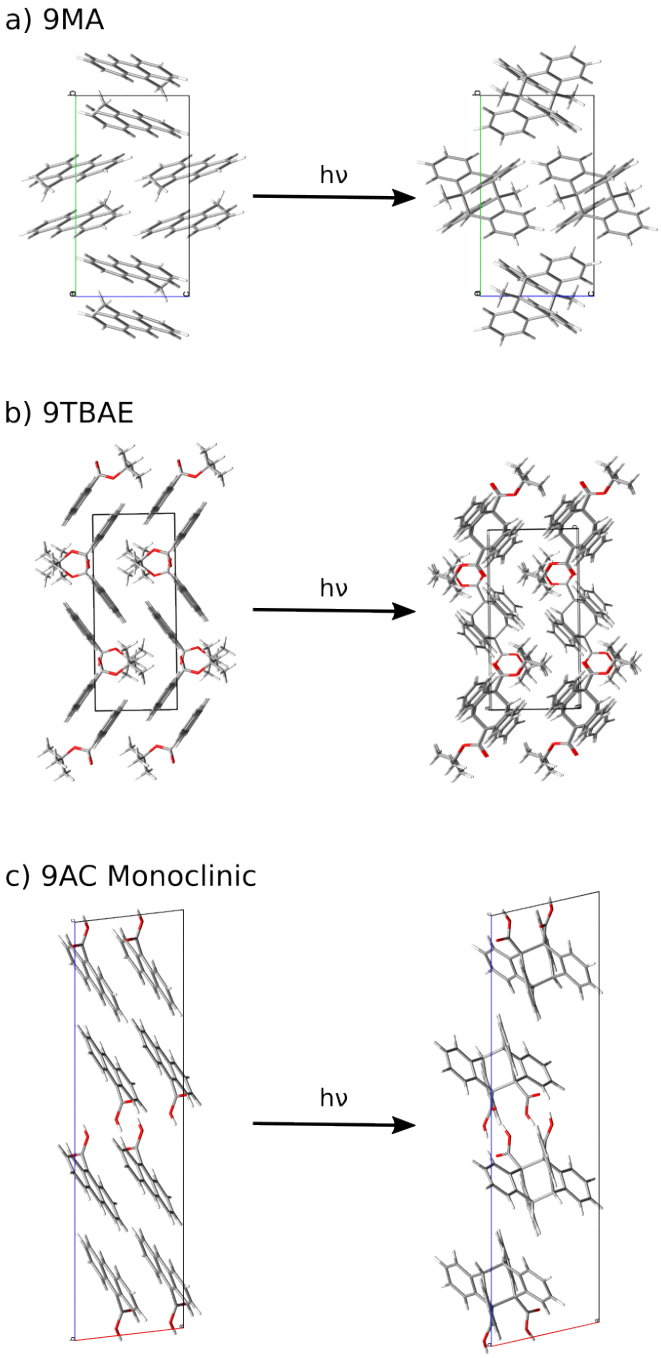

Figure 6.5: The crystalline topochemical hypothesis generates the SSRD based on the crystal packing of the monomer, as shown here for (a) 9MA, (b) 9TBAE, and (c) 9AC.

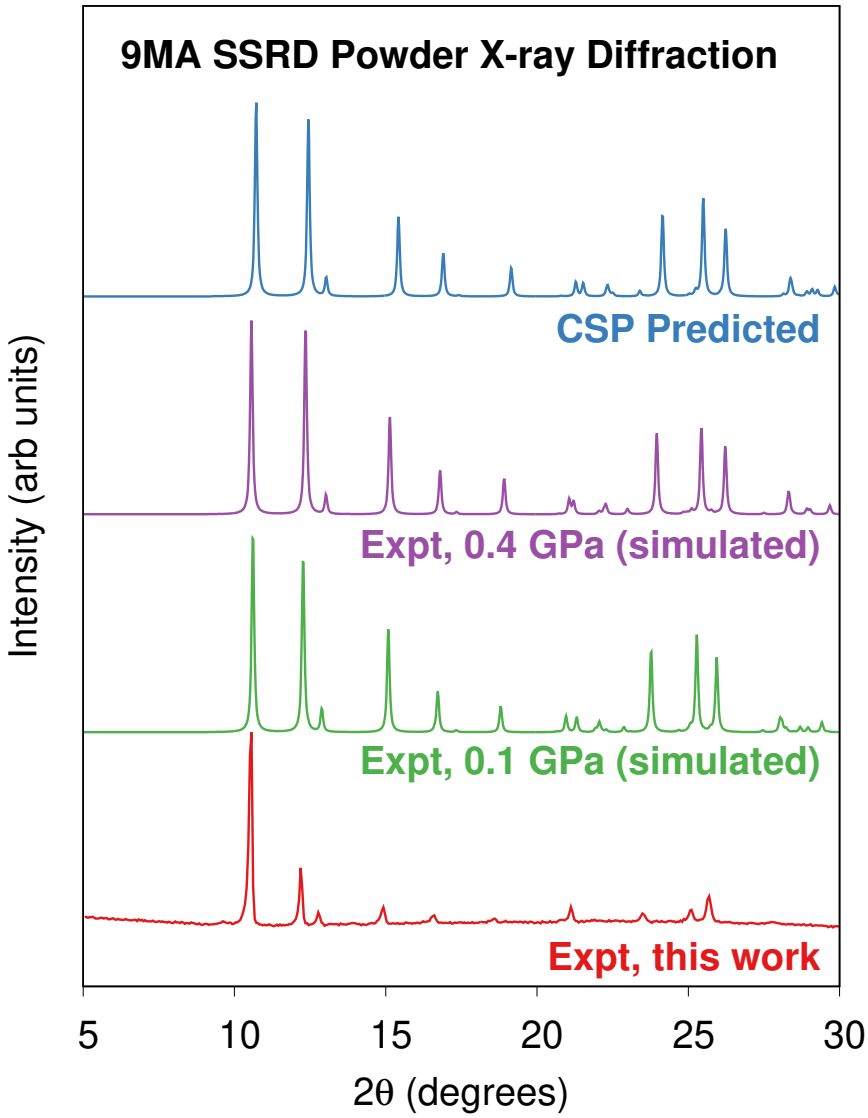

Figure 6.6: Comparison of the powder X-ray diffractograms obtained on platelets of 9MA after 40 seconds illumination against the powder diffractograms simulated using the experimentally-reported[14] SSRD crystal structures obtained at 0.1 and 0.4 GPa and the SSRD structure generated via crystal structure prediction here.

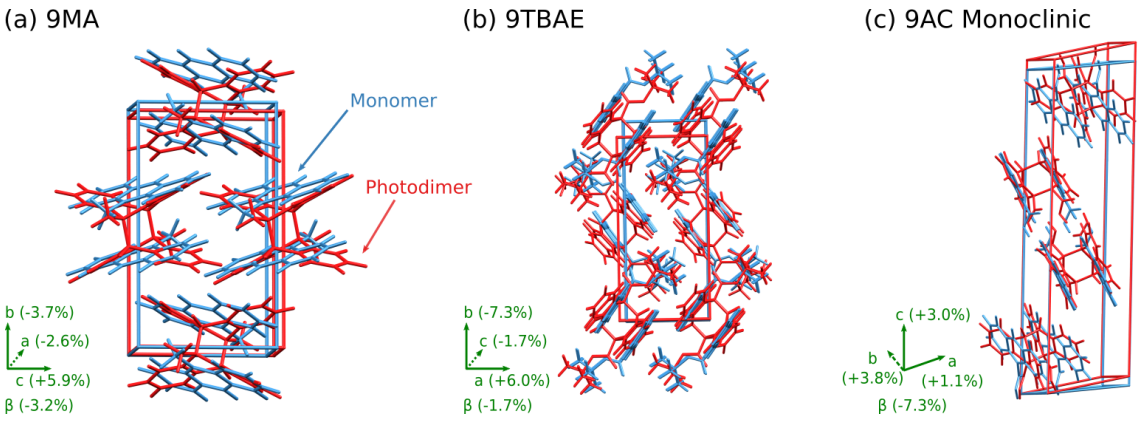

Figure 6.7: Structure overlays showing the unit cell transformation from monomer (blue) to SSRD (red) for (a) 9MA, (b) 9TBAE, and (c) monoclinic 9AC.

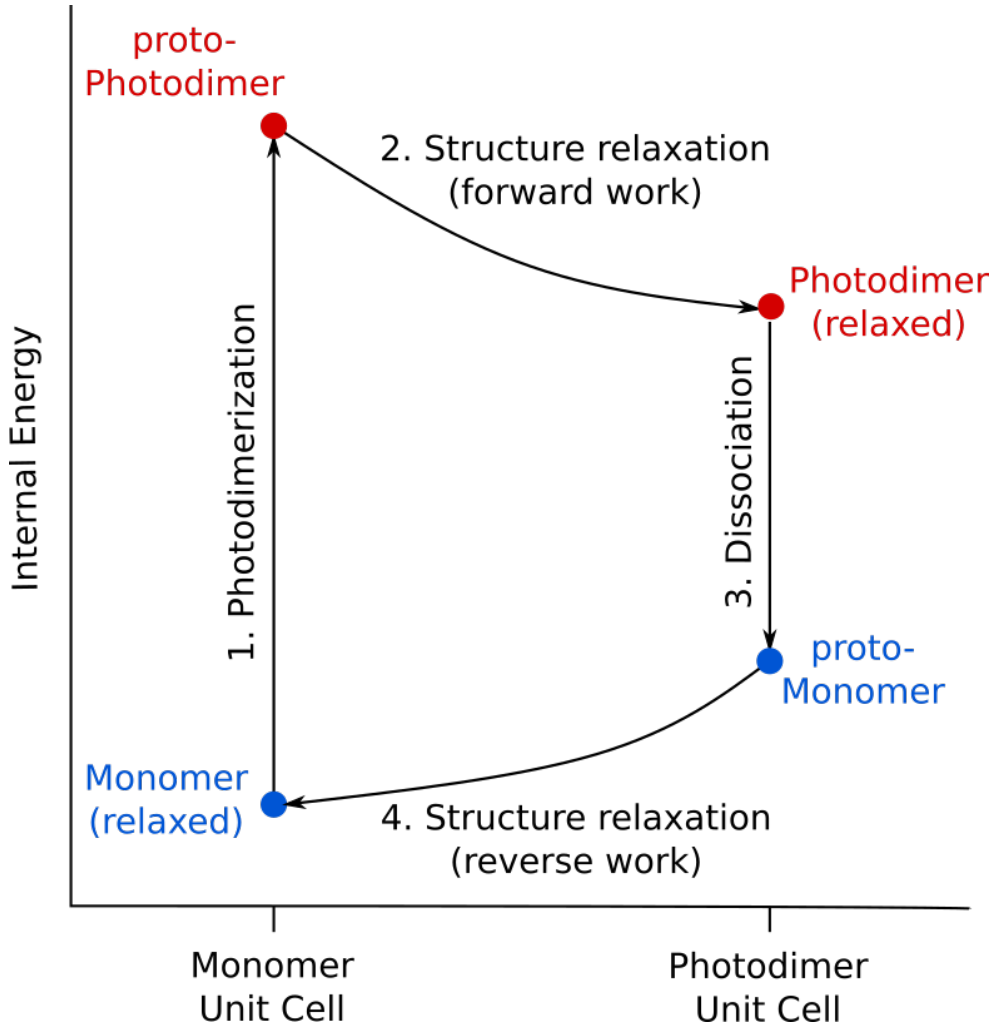

Figure 6.8: The proposed photomechanical engine cycle for anthracene systems consists of: (1) topochemical photodimerization within the monomer unit cell to form the proto-Photodimer (SSRD), (2) relaxation of the strained proto-Photodimer to perform forward work, (3) topochemical dissociation of the photodimer back to the monomer within the photodimer unit cell (proto-Monomer), and (4) reverse work generated by relaxation of the proto-Monomer back to the original equilibrium structure.

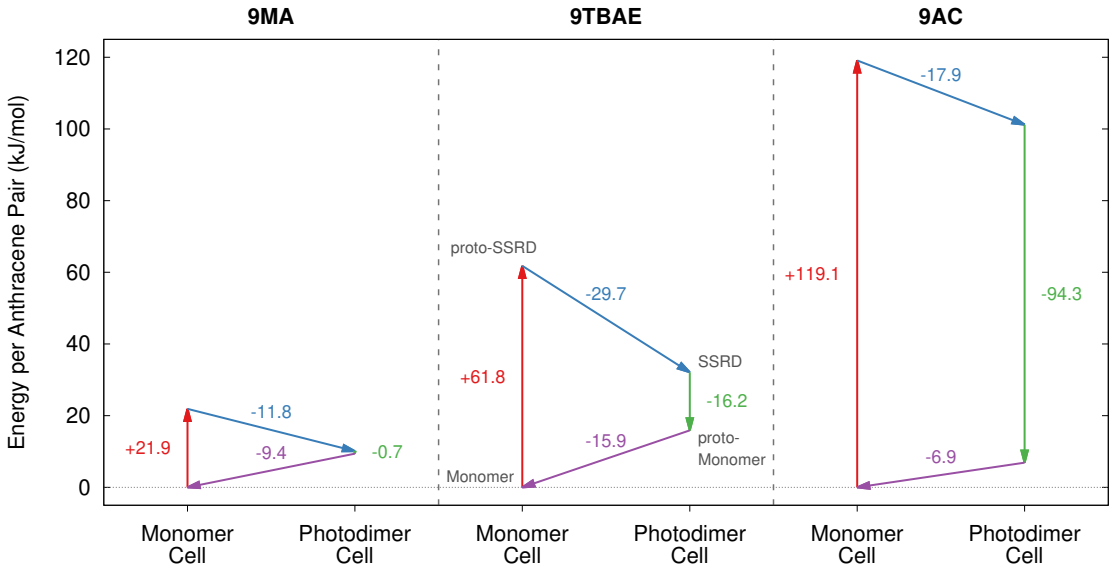

Figure 6.9: The energetics associated with the four stages of the photomechanical engine cycle differ significantly across 9MA, 9TBAE, and monoclinic 9AC.

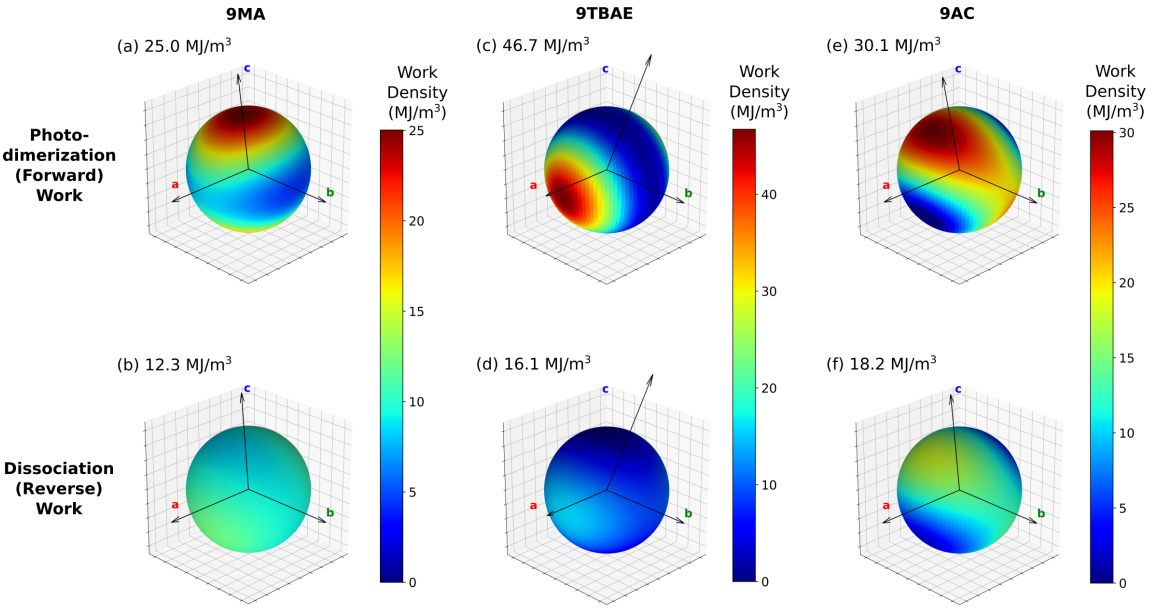

Figure 6.10: The predicted work densities for the forward photodimerization and reverse dissociation reactions of 9MA, 9TBAE, and monoclinic 9AC are highly anisotropic. Crystallographic axes shown correspond to the unit cell of the product for each reaction, and the maximal computed work density for each transformation is indicated. Absolute values of the work densities are plotted for convenience.

Chapter 7

Conclusions

A fast and reliable crystal structure prediction workflow would undoubtedly be beneficial to rational materials design. CSP itself is a multi-faceted problem requiring independent sampling and ranking efforts to accurately represent the crystal potential energy landscape. Balance between computational effort and level of accuracy is crucial, and the correct balance varies depending on the problem at hand. This thesis introduced additional tools for the energetic ranking of molecular crystals, specifically for the inclusion of finite-temperature thermodynamic effects, and showed some applications of this method to several molecular crystals. CSP was also used in the study of photomechanical crystals, allowing for an in-depth understanding of the reactant and product unit cell evolution and quantification of anisotropic work output.

A phonon normal mode matching method for vibrational free energy contributions was introduced. Crystal supercell phonon dispersion was evaluated with cheap semi-empirical quantum mechanics and up scaled to *ab initio* density functional methods via

normal mode eigenvector overlap. Thermodynamic quantities of several small molecule organic molecular crystals were determined with experimental accuracy, and the correct polymorph ranking of five oxalyl dihydrazide (ODH) forms was predicted. This can serve as an additional tool in the toolkit of crystal free energy ranking.

Affordable quasiharmonic thermal expansion was then made possible by coupling with cheaper free energy assignments via mode-matching. Temperature dependent properties for the small organic molecular crystal resorcinol such as cell volume and density of its most stable polymorphs were predicted with excellent agreement to experiment. Finite temperature unit cell volumes of the β and α forms of resorcinol were accurately determined. Additional insight into the thermodynamic properties of the solid-to-solid phase transition was also gleaned.

These methods were extended to the organic semiconducting crystals naphthalene, pentacene, and benzothieno[3,2-b][1]benzothiophene (BTBT). QHA/mode-matching was used to predict the temperature dependence of the charge transfer integral as thermal expansion drove the increase intermolecular separation. QHA expanded structures were able to qualitatively capture contraction or expansion of individual lattice parameters and had quantitative agreement with unit cell volumes as a function of temperature. This information could help further explain how intermolecular transfer integrals vary with thermal expansion of the crystal.

Finally, crystal structure prediction was employed for photomechanical systems. These crystals, whose molecular pairs undergo a [4+4] dimerization when exposed to the correct wavelength of light, expand or contract anisotropically and yield mechanical work.

CSP was used to characterize the landscape of the reactant and product of the 9-methyl anthracene (9MA) photodimerization, showing the energetic relationships between important forms and solving for their crystal lattice parameters. This allowed for determination of the magnitude and direction of the resulting work, an important quantity for designing actuators or smart materials from these types of systems. The methods introduced for 9MA were also used to determine the crystal structures and theoretical work output for two additional photomechanical crystals: 9-anthracene carboxylic acid (9AC) and 9-tert-butyl-anthracene ester (9TBAE).

Crystal structure prediction remains full of avenues for additional research. True high-throughput CSP with finite temperature effects is still largely intractable without immense computer power. The methods introduced here were certainly intended to alleviate this, however they can only realistically be applied to a few dozen polymorphs before becoming unwieldy. A "true" free energy determination would need to be applicable hundreds of potential forms of a particular molecular crystal. The general formulation for mode-matching coupled with quasiharmonic expansion can be extended to any other pairing of quantum chemical techniques not limited to DFT/DFTB. Could additional fine-tuning of other methods for pDOS corrections potentially reach an even more cost effective balance of accuracy and speed? Would this allow for "true" free energy predictions without strenuous hierarchical ranking?

Additional applications of crystal structure prediction as a whole can also be considered. In industry, CSP is typically focused on inorganic materials or pharmaceuticals design, but computational methods and computing power has evolved enough to justify

application elsewhere. Here we presented a novel CSP study for photomechanical systems, potentially streamlining the design of smart materials based off of organic molecular crystals. Where else can systematic sampling and energetic ranking procedures of complicated crystal landscapes be of use? Systems like high entropy alloys, organic semiconductors, and photoactuators are all dependent on crystal structures from high dimensional potential energy landscapes. Relying on computer aided materials design as a practical approach could introduce more efficient engineering of novel materials.

Bibliography

[1] S. Kichanov, D. Kozlenko, P. Bilski, J. Wąsicki, W. Nawrocik, A. Medek, B. Hancock, E. Lukin, C. Lathe, L. Dubrovinsky, and B. Savenko, "The polymorphic phase transformations in resorcinol at high pressure," *J. Mol. Struct.*, vol. 1006, pp. 337–343, dec 2011.

[2] F. Safari, A. Olejniczak, and A. Katrusiak, "Pressure-Dependent Crystallization Preference of Resorcinol Polymorphs," *Cryst. Growth Des.*, vol. 19, pp. 5629–5635, oct 2019.

[3] K. Drużbicki, E. Mikuli, N. Pałka, S. Zalewski, and M. D. Ossowska-Chruściel, "Polymorphism of Resorcinol Explored by Complementary Vibrational Spectroscopy (FT-RS, THz-TDS, INS) and First-Principles Solid-State Computations (Plane-Wave DFT)," *J. Phys. Chem. B*, vol. 119, pp. 1681–1695, jan 2015.

[4] S. C. Capelli, A. Albinati, S. A. Mason, and B. T. Willis, "Molecular motion in crystalline naphthalene: Analysis of multi-temperature X-ray and neutron diffraction data," *Journal of Physical Chemistry A*, vol. 110, no. 41, pp. 11695–11703, 2006.

[5] S. C. Abrahams, J. M. Robertson, and J. G. White, "The crystal and molecular structure of naphthalene. I. X-ray measurements," *Acta Crystallographica*, vol. 2, no. 4, pp. 233–238, 1949.

[6] D. W. J. Cruickshank, "A detailed refinement of the crystal and molecular structure of naphthalene," *Acta Crystallographica*, vol. 10, no. 8, pp. 504–508, 1957.

[7] J. Oddershede and S. Larsen, "Charge Density Study of Naphthalene Based on X-Ray Diffraction Data at Four Different Temperatures and Theoretical Calculations," *Journal of Physical Chemistry A*, vol. 108, no. 6, pp. 1057–1063, 2004.

[8] P. A. Banks, J. Maul, M. T. Mancini, A. C. Whalley, A. Erba, and M. T. Ruggiero, "Thermoelasticity in organic semiconductors determined with terahertz spectroscopy and quantum quasi-harmonic simulations," *J. Mater. Chem. C*, vol. 8, no. 31, pp. 10917–10925, 2020.

[9] V. S. Vyas, R. Gutzler, J. Nuss, K. Kern, and B. V. Lotsch, "Optical gap in herringbone and π-stacked crystals of [1]benzothieno[3,2-b]benzothiophene and its brominated derivative," *CrystEngComm*, vol. 16, no. 32, pp. 7389–7392, 2014.

[10] C. Niebel, Y. Kim, C. Ruzié, J. Karpinska, B. Chattopadhyay, G. Schweicher, A. Richard, V. Lemaur, Y. Olivier, J. Cornil, A. R. Kennedy, Y. Diao, W. Y. Lee, S. Mannsfeld, Z. Bao, and Y. H. Geerts, "Thienoacene dimers based on the thieno[3,2-b]thiophene moiety: Synthesis, characterization and electronic properties," *Journal of Materials Chemistry C*, vol. 3, no. 3, pp. 674–685, 2015.

[11] M. Matsumura, A. Muranaka, R. Kurihara, M. Kanai, K. Yoshida, N. Kakusawa, D. Hashizume, M. Uchiyama, and S. Yasuike, "General synthesis, structure, and optical properties of benzothiophene-fused benzoheteroles containing Group 15 and 16 elements," *Tetrahedron*, vol. 72, no. 49, pp. 8085–8090, 2016.

[12] G. Liu, S.-H. Wei, and C. Zhang, "Review of the Intermolecular Interactions in Energetic Molecular Cocrystals," *Cryst. Growth Des.*, vol. 20, pp. 7065–7079, oct 2020.

[13] M. T. Ruggiero, S. Ciuchi, S. Fratini, and G. D'Avino, "Electronic Structure, Electron-Phonon Coupling, and Charge Transport in Crystalline Rubrene Under Mechanical Strain," *The Journal of Physical Chemistry C*, vol. 123, pp. 15897–15907, jul 2019.

[14] J. Bąkowicz and I. Turowska-Tyrk, "The role of free space in photochemical reactions in crystals at high pressure - the case of 9-methylanthracene," *Acta Cryst. B*, vol. 78, pp. 223–230, apr 2022.

[15] S. R. Chemburkar, J. Bauer, K. Deming, H. Spiwek, K. Patel, J. Morris, R. Henry, S. Spanton, W. Dziki, W. Porter, J. Quick, P. Bauer, J. Donaubauer, B. A. Narayanan, M. Soldani, D. Riley, and K. Mcfarland, "Dealing with the Impact of Ritonavir Polymorphs on the Late Stages of Bulk Drug Process Development," *Org. Proc. Res. Dev.*, vol. 4, no. 5, pp. 413–417, 2000.

[16] J. Bauer, S. Spanton, R. Quick, J. Quick, W. Dziki, W. Porter, and J. Morris, "Ritonavir: An extraordinary example of conformational polymorphism," *Pharm. Res.*, vol. 18, pp. 859–866, 2001.

[17] M. A. Neumann and J. van de Streek, "How many ritonavir cases are there still out there?," *Faraday Disc.*, vol. 211, pp. 441–458, 2018.

[18] A. Pulido, L. Chen, T. Kaczorowski, D. Holden, M. A. Little, S. Y. Chong, B. J. Slater, D. P. McMahon, B. Bonillo, C. J. Stackhouse, A. Stephenson, C. M. Kane, R. Clowes, T. Hasell, A. I. Cooper, and G. M. Day, "Functional materials discovery using energy-structure-function maps," *Nature*, vol. 543, no. 7647, pp. 657–664, 2017.

[19] B. Rice, L. M. Leblanc, A. Otero-De-La-Roza, M. J. Fuchter, E. R. Johnson, J. Nelson, and K. E. Jelfs, "A computational exploration of the crystal energy and charge-carrier mobility landscapes of the chiral [6]helicene molecule," *Nanoscale*, vol. 10, no. 4, pp. 1865–1876, 2018.

[20] J. A. Schmidt, J. A. Weatherby, I. J. Sugden, A. Santana-Bonilla, F. Salerno, M. J. Fuchter, E. R. Johnson, J. Nelson, and K. E. Jelfs, "Computational Screening of Chiral Organic Semiconductors: Exploring Side-Group Functionalization and Assembly to Optimize Charge Transport," *Crystal Growth and Design*, vol. 21, no. 9, pp. 5036–5049, 2021.

[21] S. Herbertz, J. S. Sawyer, A. J. Stauber, I. Gueorguieva, K. E. Driscoll, S. T. Estrem, A. L. Cleverly, D. Desaiah, S. C. Guba, K. A. Benhadji, C. A. Slapak, and M. M. Lahn, "Clinical development of galunisertib (Ly2157299 monohydrate), a small molecule inhibitor of transforming growth factor-beta signaling pathway," *Drug Design, Development and Therapy*, vol. 9, pp. 4479–4499, 2015.

[22] R. M. Bhardwaj, J. A. McMahon, J. Nyman, L. S. Price, S. Konar, I. D. Oswald, C. R. Pulham, S. L. Price, and S. M. Reutzel-Edens, "A Prolific Solvate Former, Galunisertib, under the Pressure of Crystal Structure Prediction, Produces Ten Diverse Polymorphs," *Journal of the American Chemical Society*, vol. 141, no. 35, pp. 13887–13897, 2019.

[23] A. R. Oganov, C. J. Pickard, Q. Zhu, and R. J. Needs, "Structure prediction drives materials discovery," *Nature Reviews Materials*, vol. 4, no. 5, pp. 331–348, 2019.

[24] M. Addicoat, C. S. Adjiman, M. Arhangelskis, G. J. O. Beran, D. Bowskill, J. G. Brandenburg, D. E. Braun, V. Burger, J. Cole, A. J. Cruz-Cabeza, G. M. Day, V. L. Deringer, R. Guo, A. Hare, J. Helfferich, J. Hoja, L. Iuzzolino, S. Jobbins, N. Marom, D. McKay, J. B. O. Mitchell, S. Mohamed, M. Neumann, S. Nilsson Lill, J. Nyman, A. R. Oganov, P. Piaggi, S. L. Price, S. Reutzel-Edens, I. Rietveld, M. Ruggiero, M. R. Ryder, G. Sastre, J. C. Schön, C. Taylor, A. Tkatchenko, S. Tsuzuki, J. van den Ende, S. M. Woodley, G. Woollam, and Q. Zhu, "Crystal structure evaluation: Calculating relative stabilities and other criteria: General discussion," *Faraday Discuss.*, vol. 211, pp. 325–381, 2018.

[25] J. P. M. Lommerse, W. D. S. Motherwell, H. L. Ammon, J. D. Dunitz, A. Gavezzotti, D. W. M. Hofmann, F. J. J. Leusen, W. T. M. Mooij, S. L. Price, B. Schweizer, M. U. Schmidt, B. P. van Eijck, P. Verwer, and D. E. Williams, "A test of crystal structure prediction of small organic molecules," *Acta Cryst. B*, vol. 56, pp. 697–714, aug 2000.

[26] W. D. S. Motherwell, H. L. Ammon, J. D. Dunitz, A. Dzyabchenko, P. Erk, A. Gavezzotti, D. W. M. Hofmann, F. J. J. Leusen, J. P. M. Lommerse, W. T. M. Mooij, S. L. Price, H. A. Scheraga, B. Schweizer, M. U. Schmidt, B. P. van Eijck,

P. Verwer, and D. E. Williams, "Crystal structure prediction of small organic molecules: a second blind test," *Acta Cryst. B*, vol. 58, pp. 647–661, jul 2002.

[27] G. M. Day, W. D. S. Motherwell, H. L. Ammon, S. X. M. Boerrigter, R. G. Della Valle, E. Venuti, A. Dzyabchenko, J. D. Dunitz, B. Schweizer, B. P. van Eijck, P. Erk, J. C. Facelli, V. E. Bazterra, M. B. Ferraro, D. W. M. Hofmann, F. J. J. Leusen, C. Liang, C. C. Pantelides, P. G. Karamertzanis, S. L. Price, T. C. Lewis, H. Nowell, A. Torrisi, H. A. Scheraga, Y. A. Arnautova, M. U. Schmidt, and P. Verwer, "A third blind test of crystal structure prediction," *Acta Cryst. B*, vol. 61, pp. 511–527, 2005.

[28] G. M. Day, T. G. Cooper, A. J. Cruz-Cabeza, K. E. Hejczyk, H. L. Ammon, S. X. M. Boerrigter, J. S. Tan, R. G. Della Valle, E. Venuti, J. Jose, S. R. Gadre, G. R. Desiraju, T. S. Thakur, B. P. van Eijck, J. C. Facelli, V. E. Bazterra, M. B. Ferraro, D. W. M. Hofmann, M. A. Neumann, F. J. J. Leusen, J. Kendrick, S. L. Price, A. J. Misquitta, P. G. Karamertzanis, G. W. A. Welch, H. A. Scheraga, Y. A. Arnautova, M. U. Schmidt, J. van de Streek, A. K. Wolf, and B. Schweizer, "Significant progress in predicting the crystal structures of small organic molecules - a report on the fourth blind test," *Acta Cryst. B*, vol. 65, pp. 107–125, 2009.

[29] D. A. Bardwell, C. S. Adjiman, Y. A. Arnautova, E. Bartashevich, S. X. M. Boerrigter, D. E. Braun, A. J. Cruz-Cabeza, G. M. Day, R. G. Della Valle, G. R. Desiraju, B. P. van Eijck, J. C. Facelli, M. B. Ferraro, D. Grillo, M. Habgood, D. W. M. Hofmann, F. Hofmann, K. V. J. Jose, P. G. Karamertzanis, A. V. Kazantsev, J. Kendrick, L. N. Kuleshova, F. J. J. Leusen, A. V. Maleev, A. J. Misquitta, S. Mohamed, R. J. Needs, M. A. Neumann, D. Nikylov, A. M. Orendt, R. Pal, C. C. Pantelides, C. J. Pickard, L. S. Price, S. L. Price, H. A. Scheraga, J. van de Streek, T. S. Thakur, S. Tiwari, E. Venuti, and I. K. Zhitkov, "Towards crystal structure prediction of complex organic compounds—A report on the fifth blind test.," *Acta Cryst. B*, vol. 67, pp. 535–551, dec 2011.

[30] A. M. Reilly, R. I. Cooper, C. S. Adjiman, S. Bhattacharya, A. D. Boese, J. G. Brandenburg, P. J. Bygrave, R. Bylsma, J. E. Campbell, R. Car, D. H. Case, R. Chadha, J. C. Cole, K. Cosburn, H. M. Cuppen, F. Curtis, G. M. Day, R. A. DiStasio Jr, A. Dzyabchenko, B. P. van Eijck, D. M. Elking, J. A. van den Ende, J. C. Facelli, M. B. Ferraro, L. Fusti-Molnar, C.-A. Gatsiou, T. S. Gee, R. de Gelder, L. M. Ghiringhelli, H. Goto, S. Grimme, R. Guo, D. W. M. Hofmann, J. Hoja, R. K. Hylton, L. Iuzzolino, W. Jankiewicz, D. T. de Jong, J. Kendrick, N. J. J. de Klerk, H.-Y. Ko, L. N. Kuleshova, X. Li, S. Lohani, F. J. J. Leusen, A. M. Lund, J. Lv, Y. Ma, N. Marom, A. E. Masunov, P. McCabe, D. P. McMahon, H. Meekes, M. P. Metz, A. J. Misquitta, S. Mohamed, B. Monserrat, R. J. Needs, M. A. Neumann, J. Nyman, S. Obata, H. Oberhofer, A. R. Oganov, A. M. Orendt, G. I. Pagola, C. C. Pantelides, C. J. Pickard, R. Podeszwa, L. S. Price, S. L. Price, A. Pulido, M. G. Read, K. Reuter, E. Schneider, C. Schober, G. P. Shields, P. Singh, I. J. Sugden, K. Szalewicz, C. R. Taylor, A. Tkatchenko, M. E.

Tuckerman, F. Vacarro, M. Vasileiadis, A. Vazquez-Mayagoitia, L. Vogt, Y. Wang, R. E. Watson, G. A. de Wijs, J. Yang, Q. Zhu, and C. R. Groom, "Report on the sixth blind test of organic crystal structure prediction methods," *Acta Cryst. B*, vol. 72, pp. 439–459, aug 2016.

[31] F. Jensen, "Introduction to computational chemistry," 2007.

[32] J. Nyman and G. M. Day, "Static and lattice vibrational energy differences between polymorphs," *CrystEngComm*, vol. 17, no. 28, pp. 5154–5165, 2015.

[33] Q. Yu, B. Aguila, J. Gao, P. Xu, Q. Chen, J. Yan, D. Xing, Y. Chen, P. Cheng, Z. Zhang, and S. Ma, "Photomechanical Organic Crystals as Smart Materials for Advanced Applications," *Chem. Eur. J.*, vol. 25, no. 22, pp. 5611–5622, 2019.

[34] R. O. Al-Kaysi and C. J. Bardeen, "Reversible photoinduced shape changes of crystalline organic nanorods," *Adv. Mater.*, vol. 19, no. 9, pp. 1276–1280, 2007.

[35] R. O. Al-Kaysi, A. M. Müller, and C. J. Bardeen, "Photochemically Driven Shape Changes of Crystalline Organic Nanorods," *J. Am. Chem. Soc.*, vol. 128, pp. 15938–15939, dec 2006.

[36] X. Dong, F. Tong, K. M. Hanson, R. O. Al-Kaysi, D. Kitagawa, S. Kobatake, and C. J. Bardeen, "Hybrid Organic-Inorganic Photon-Powered Actuators Based on Aligned Diarylethene Nanocrystals," *Chemistry of Materials*, vol. 31, no. 3, pp. 1016–1022, 2019.

[37] S. Erbas-Cakmak, D. A. Leigh, C. T. McTernan, and A. L. Nussbaumer, "Artificial Molecular Machines," *Chemical Reviews*, vol. 115, no. 18, pp. 10081–10206, 2015.

[38] R. Rai, B. P. Krishnan, and K. M. Sureshan, "Chirality-controlled spontaneous twisting of crystals due to thermal topochemical reaction," *Proceedings of the National Academy of Sciences of the United States of America*, vol. 115, no. 12, pp. 2896–2901, 2018.

[39] D. Yan, Z. Wang, and Z. Zhang, "Stimuli-Responsive Crystalline Smart Materials: From Rational Design and Fabrication to Applications," *Accounts of Chemical Research*, vol. 55, no. 7, pp. 1047–1058, 2022.

[40] I. Turowska-Tyrk and E. Trzop, "Monitoring structural transformations in crystals. 6. The [4 + 4] photodimerization of 9-methyl-anthracene," *Acta Cryst. B*, vol. 59, no. 6, pp. 779–786, 2003.

[41] S. Takahashi, H. Miura, H. Kasai, S. Okada, H. Oikawa, and H. Nakanishi, "Single-Crystal-to-Single-Crystal Transformation of Diolefin Derivatives in Nanocrystals," *J. Am. Chem. Soc.*, vol. 124, pp. 10944–10945, sep 2002.

[42] G. J. O. Beran, "First-principles computations indicate that solid state photodimerization of 9-*tert*-butyl anthracene ester produces an exceptionally metastable polymorph," *CrystEngComm*, vol. 21, pp. 758–764, 2019.

[43] C. Yang, L. Zhu, R. A. Kudla, J. D. Hartman, R. O. Al-Kaysi, S. Monaco, B. Schatschneider, A. Magalhães, G. J. O. Beran, C. J. Bardeen, and L. J. Mueller, "Crystal structure of the meta-stable intermediate in the photomechanical, crystal-to-crystal reaction of 9-tert-butyl anthracene ester," *CrystEngComm*, vol. 15, no. 2006, pp. 400–414, 2016.

[44] K. R. Chalek, X. Dong, F. Tong, R. A. Kudla, L. Zhu, A. D. Gill, W. Xu, C. Yan, J. D. Hartman, A. Magalhaes, R. O. Al-Kaysi, R. C. Hayward, R. J. Hooley, G. J. O. Beran, C. J. Bardeen, and L. J. Mueller, "Bridging photochemistry and photomechanics with NMR crystallography: the molecular basis for the macroscopic expansion of an anthracene ester nanorod," *Chem. Sci.*, vol. 12, pp. 453–463, 2021.

[45] M. Dove, "Introduction to the theory of lattice dynamics," *Collection SFN*, vol. 12, pp. 123–159, jun 2011.

[46] G. M. Day, "Lattice Dynamical Studies of Molecular Crystals with Application to Polymorphism and Strucutre Prediction," *PhD Thesis*, 2003.

[47] M. Musgrave, "Crystal acoustics," 1970.

[48] N. L. Allan, G. D. Barrera, T. H. K. Barron, and M. B. Taylor, "Evaluation of Thermodynamic Properties of Solids by Quasiharmonic Lattice Dynamics," *Int. J. Thermophys.*, vol. 22, no. 2, pp. 535–546, 2001.

[49] R. P. Stoffel, C. Wessel, M.-W. Lumey, and R. Dronskowski, "Ab Initio Thermochemistry of Solid-State Materials," *Angew. Chem. Int. Ed.*, vol. 49, pp. 5242–5266, jun 2010.

[50] C. Červinka and G. J. O. Beran, "Ab initio thermodynamic properties and their uncertainties for crystalline α-methanol," *Phys. Chem. Chem. Phys.*, vol. 19, pp. 29940–29953, 2017.

[51] C. Červinka and G. J. O. Beran, "Improved electrostatic embedding for fragment-based chemical shift calculations in molecular crystals," *Chem. Sci.*, vol. 9, pp. 4622–4629, 2018.

[52] F. D. Murnaghan, "The compressibility of media under extreme pressures," *Proc. Nat. Acad. Sci.*, vol. 30, pp. 244–247, 1944.

[53] E. F. Valeev, V. Coropceanu, D. A. Da Silva Filho, S. Salman, and J. L. Brédas, "Effect of electronic polarization on charge-transport parameters in molecular organic semiconductors," *Journal of the American Chemical Society*, vol. 128, no. 30, pp. 9882–9886, 2006.

[54] J. J. Kwiatkowski, "From molecules to mobilities : semiconductors," *Solid State Physics*, no. December, 2008.

[55] V. Coropceanu, J. Cornil, D. A. da Silva Filho, Y. Olivier, R. Silbey, and J. L. Brédas, "Charge transport in organic-file:///home/cameron/Documents/GradSchool/malibu_backup/Literature/OSC_phonons/1-s2.0-S2352492820325204-main.pdf semiconductors," *Chemical Reviews*, vol. 107, no. 4, pp. 926–952, 2007.

[56] E. Rice, "Computational Modelling of Electronic States, Charge Transfer and Charge Transport in Organic Semiconductors," *Imperial College London*, 2018.

[57] J. Kirkpatrick, "An Approximate Method for Calculating Transfer Integrals Based on the ZINDO Hamiltonian," *International Journal of Quantum Chemistry*, vol. 108, pp. 51 – 56, 2007.

[58] S. Grimme, C. Diedrich, and M. Korth, "The Importance of Inter- and Intramolecular van der Waals Interactions in Organic Reactions: the Dimerization of Anthracene Revisited," *Angew. Chem. Int. Ed.*, vol. 45, pp. 625–629, jan 2006.

[59] J. Řezáč, C. Greenwell, and G. J. O. Beran, "Accurate non-covalent interactions via dispersion-corrected second-order Møller-Plesset perturbation theory," *J. Chem. Theory Comput.*, vol. 14, pp. 4711–4721, 2018.

[60] C. Greenwell, J. Řezáč, and G. J. O. Beran, "Spin-component-scaled and dispersion-corrected second-order Møller-Plesset perturbation theory: An alternative path toward chemical accuracy," *Phys. Chem. Chem. Phys.*, vol. 24, pp. 3695–3712, 2022.

[61] A. J. Cohen, P. Mori-Sanchez, and W. Yang, "Challenges for Density Functional Theory.," *Chem. Rev.*, vol. 112, pp. 289–320, dec 2012.

[62] L. M. LeBlanc, S. G. Dale, C. R. Taylor, A. D. Becke, G. M. Day, and E. R. Johnson, "Pervasive Delocalisation Error Causes Spurious Proton Transfer in Organic Acid-Base Co-Crystals," *Angew. Chem. Int. Ed.*, vol. 57, pp. 14906–14910, nov 2018.

[63] S. R. Whittleton, A. Otero-de-la Roza, and E. R. Johnson, "Exchange-Hole Dipole Dispersion Model for Accurate Energy Ranking in Molecular Crystal Structure Prediction II: Nonplanar Molecules," *J. Chem. Theory Comput.*, vol. 13, pp. 5332–5342, nov 2017.

[64] A. Otero-de-la Roza, L. M. LeBlanc, and E. R. Johnson, "Dispersion XDM with Hybrid Functionals: Delocalization Error and Halogen Bonding in Molecular Crystals," *J. Chem. Theory Comput.*, vol. 15, pp. 4933–4944, 2019.

[65] C. Greenwell, J. L. McKinley, P. Zhang, Q. Zeng, G. Sun, B. Li, S. Wen, and G. J. O. Beran, "Overcoming the difficulties of predicting conformational polymorph energetics in molecular crystals via correlated wavefunction methods," *Chem. Sci.*, vol. 11, pp. 2200–2214, 2020.

[66] C. Greenwell and G. J. O. Beran, "Inaccurate conformational energies still hinder crystal structure prediction in flexible organic molecules," *Cryst. Growth Des.*, vol. 20, pp. 4875–4881, 2020.

[67] C. Greenwell and G. J. O. Beran, "Rubrene untwisted: common density functional theory calculations overestimate its deviant tendencies," *J. Mater. Chem. C*, vol. 9, pp. 2848–2857, 2021.

[68] G. J. O. Beran, I. J. Sugden, C. Greenwell, D. H. Bowskill, C. C. Pantelides, and C. S. Adjiman, "How many more polymorphs of ROY remain undiscovered?," *Chem. Sci.*, vol. 13, pp. 1288–1297, 2022.

[69] G. J. O. Beran, S. E. Wright, C. Greenwell, and A. J. Cruz-Cabeza, "The interplay of intra- and intermolecular errors in modeling conformational polymorphs," *J. Chem. Phys.*, vol. 156, p. 104112, 2022.

[70] R. Sure and S. Grimme, "Corrected small basis set Hartree-Fock method for large systems," *J. Comp. Chem.*, vol. 34, pp. 1672–1685, jul 2013.

[71] P. Naumov, S. Chizhik, M. K. Panda, N. K. Nath, and E. Boldyreva, "Mechanically Responsive Molecular Crystals," *Chem. Rev.*, vol. 115, no. 22, pp. 12440–12490, 2015.

[72] T. Taniguchi, K. Ishizaki, D. Takagi, K. Nishimura, H. Shigemune, M. Kuramochi, Y. C. Sasaki, H. Koshima, and T. Asahi, "Superelasticity of a photo-actuating chiral salicylideneamine crystal," *Communications Chemistry*, vol. 5, no. 1, pp. 4–12, 2022.

[73] H. Kim, J.-m. Choi, and W. A. Goddard, "Universal Correction of Density Functional Theory to Include London Dispersion (up to Lr, Element 103)," *J. Phys. Chem. Lett.*, vol. 3, pp. 360–363, 2012.

[74] T. J. Gately, W. Sontising, C. J. Easley, I. Islam, R. O. Al-Kaysi, G. J. O. Beran, and C. J. Bardeen, "Effect of halogen substitution on energies and dynamics of reversible photomechanical crystals based on 9-anthracenecarboxylic acid," *CrystEngComm*, vol. 23, pp. 5931–5943, 2021.

[75] L. Zhu, A. Agarwal, J. Lai, R. O. Al-Kaysi, F. S. Tham, T. Ghaddar, L. Mueller, and C. J. Bardeen, "Solid-state photochemical and photomechanical properties of molecular crystal nanorods composed of anthracene ester derivatives," *Journal of Materials Chemistry*, vol. 21, no. 17, pp. 6258–6268, 2011.

[76] P. Giannozzi, S. Baroni, N. Bonini, M. Calandra, R. Car, C. Cavazzoni, D. Ceresoli, G. L. Chiarotti, M. Cococcioni, I. Dabo, A. Dal Corso, S. de Gironcoli, S. Fabris, G. Fratesi, R. Gebauer, U. Gerstmann, C. Gougoussis, A. Kokalj, M. Lazzeri, L. Martin-Samos, N. Marzari, F. Mauri, R. Mazzarello, S. Paolini, A. Pasquarello,

L. Paulatto, C. Sbraccia, S. Scandolo, G. Sclauzero, A. P. Seitsonen, A. Smogunov, P. Umari, and R. M. Wentzcovitch, "QUANTUM ESPRESSO: a modular and open-source software project for quantum simulations of materials," *J. Phys. Condens. Mat.*, vol. 21, no. 39, p. 395502, 2009.

[77] A. Otero-de-la Roza and E. R. Johnson, "Van der Waals interactions in solids using the exchange-hole dipole moment model.," *J. Chem. Phys.*, vol. 136, no. 17, p. 174109, 2012.

[78] J. P. Perdew, K. Burke, and M. Ernzerhof, "Generalized gradient approximation made simple.," *Phys. Rev. Lett.*, vol. 77, p. 3865, 1996.

[79] S. Grimme, J. Antony, S. Ehrlich, and H. Krieg, "A consistent and accurate ab initio parametrization of density functional dispersion correction (DFT-D) for the 94 elements H-Pu," *J. Chem. Phys.*, vol. 132, p. 154104, apr 2010.

[80] B. Aradi, B. Hourahine, and T. Frauenheim, "DFTB+, a sparse matrix-based implementation of the DFTB method," *Journal of Physical Chemistry A*, vol. 111, no. 26, pp. 5678–5684, 2007.

[81] B. Hourahine, B. Aradi, V. Blum, F. Bonafé, A. Buccheri, C. Camacho, C. Cevallos, M. Y. Deshaye, T. Dumitrică, A. Dominguez, S. Ehlert, M. Elstner, T. van der Heide, J. Hermann, S. Irle, J. J. Kranz, C. Köhler, T. Kowalczyk, T. Kubař, I. S. Lee, V. Lutsker, R. J. Maurer, S. K. Min, I. Mitchell, C. Negre, T. A. Niehaus, A. M. N. Niklasson, A. J. Page, A. Pecchia, G. Penazzi, M. P. Persson, J. Řezáč, C. G. Sánchez, M. Sternberg, M. Stöhr, F. Stuckenberg, A. Tkatchenko, V. W. Yu, and T. Frauenheim, "DFTB+, a software package for efficient approximate density functional theory based atomistic simulations," *J. Chem. Phys.*, vol. 152, p. 124101, mar 2020.

[82] A. Togo and I. Tanaka, "First principles phonon calculations in materials science," *Scripta Materialia*, vol. 108, pp. 1–5, 2015.

[83] R. Dovesi, A. Erba, R. Orlando, C. M. Zicovich-Wilson, B. Civalleri, L. Maschio, M. Rérat, S. Casassa, J. Baima, S. Salustro, and B. Kirtman, "Quantum-mechanical condensed matter simulations with CRYSTAL," *WIREs Comput. Mol. Sci.*, vol. 8, p. e1360, jul 2018.

[84] S. Fredericks, K. Parrish, D. Sayre, and Q. Zhu, "PyXtal: A Python library for crystal structure generation and symmetry analysis," *Comput. Phys. Comm.*, vol. 261, p. 107810, apr 2021.

[85] J. Wang, R. M. Wolf, J. W. Caldwell, P. A. Kollman, and D. A. Case, "Development and testing of a general amber force field," *J. Comp. Chem.*, vol. 25, pp. 1157–1174, jul 2004.

[86] B. R. Brooks, C. L. Brooks, A. D. Mackerell, L. Nilsson, R. J. Petrella, B. Roux, Y. Won, G. Archontis, C. Bartels, S. Boresch, A. Caflisch, L. Caves, Q. Cui, A. R. Dinner, M. Feig, S. Fischer, J. Gao, M. Hodoscek, W. Im, K. Kuczera, T. Lazaridis, J. Ma, V. Ovchinnikov, E. Paci, R. W. Pastor, C. B. Post, J. Z. Pu, M. Schaefer, B. Tidor, R. M. Venable, H. L. Woodcock, X. Wu, W. Yang, D. M. York, and M. Karplus, "CHARMM: The biomolecular simulation program," *J. Comp. Chem.*, vol. 30, pp. 1545–1614, jul 2009.

[87] T. H. Dunning, "Gaussian basis sets for use in correlated molecular calculations. I. The atoms boron through neon and hydrogen," *J. Chem. Phys.*, vol. 90, pp. 1007–1023, 1989.

[88] T. Helgaker, W. Klopper, H. Koch, and J. Noga, "Basis-set convergence of correlated calculations on water," *J. Chem. Phys.*, vol. 106, pp. 9639–9646, 1997.

[89] J. M. Turney, A. C. Simmonett, R. M. Parrish, E. G. Hohenstein, F. A. Evangelista, J. T. Fermann, B. J. Mintz, L. A. Burns, J. J. Wilke, M. L. Abrams, N. J. Russ, M. L. Leininger, C. L. Janssen, E. T. Seidl, W. D. Allen, H. F. Schaefer, R. A. King, E. F. Valeev, C. D. Sherrill, and T. D. Crawford, "Psi4: an open-source ab initio electronic structure program," *WIREs: Comput. Mol. Sci.*, vol. 2, no. 4, pp. 556–565, 2012.

[90] C. Greenwell, J. Řezáč, and G. J. O. Beran, "Spin-component-scaled and dispersion-corrected second-order Møller-Plesset perturbation theory: An alternative path toward chemical accuracy," *submitted*, 2020.

[91] The MP2D software can be downloaded at `https://github.com/Chandemonium/MP2D`.

[92] J. Nyman and G. M. Day, "Static and lattice vibrational energy differences between polymorphs," *CrystEngComm*, vol. 17, no. 28, pp. 5154–5165, 2015.

[93] A. J. Cruz-Cabeza, S. M. Reutzel-Edens, and J. Bernstein, "Facts and Fictions About Polymorphism," *Chem. Soc. Rev.*, vol. 44, pp. 8619–8635, 2015.

[94] A. Burger and R. Ramberger, "On the polymorphism of pharmaceuticals and other molecular crystals. II," *Mikrochim. Acta*, vol. 72, pp. 273–316, may 1979.

[95] G. J. O. Beran, J. D. Hartman, and Y. N. Heit, "Predicting molecular crystal properties from first principles: Finite-temperature thermochemistry to NMR crystallography," *Acc. Chem. Res.*, vol. 49, pp. 2501–2508, 2016.

[96] G. J. O. Beran, "Modeling polymorphic molecular crystals with electronic structure theory," *Chem. Rev.*, vol. 116, pp. 5567–5613, 2016.

[97] S. R. Whittleton, A. Otero-de-la Roza, and E. R. Johnson, "Exchange-Hole Dipole Dispersion Model for Accurate Energy Ranking in Molecular Crystal Structure Prediction," *J. Chem. Theory Comput.*, vol. 13, pp. 441–450, feb 2017.

[98] J. Hoja, H.-Y. Ko, M. A. Neumann, R. Car, R. A. DiStasio, and A. Tkatchenko, "Reliable and practical computational description of molecular crystal polymorphs," *Science Adv.*, vol. 5, p. eaau3338, jan 2019.

[99] A. Gavezzotti and G. Filippini, "Polymorphic Forms of Organic Crystals at Room Conditions: Thermodynamic and Structural Implications," *Journal of the American Chemical Society*, vol. 117, no. 49, pp. 12299–12305, 1995.

[100] S. L. Price, "Predicting crystal structures of organic compounds.," *Chem. Soc. Rev.*, vol. 43, pp. 2098–111, apr 2014.

[101] J. Nyman and G. M. Day, "Modelling temperature-dependent properties of polymorphic organic molecular crystals," *Phys. Chem. Chem. Phys.*, vol. 18, no. 45, pp. 31132–31143, 2016.

[102] A. M. Reilly and A. Tkatchenko, "Role of Dispersion Interactions in the Polymorphism and Entropic Stabilization of the Aspirin Crystal," *Phys. Rev. Lett.*, vol. 113, p. 055701, jul 2014.

[103] A. Erba, J. Maul, and B. Civalleri, "Thermal properties of molecular crystals through dispersion-corrected quasi-harmonic ab initio calculations: the case of urea," *Chem. Commun.*, vol. 52, no. 9, pp. 1820–1823, 2016.

[104] Y. N. Heit and G. J. O. Beran, "How important is thermal expansion for predicting molecular crystal structures and thermochemistry at finite temperatures?," *Acta Cryst. B*, vol. 72, pp. 514–529, 2016.

[105] J. Hoja, A. M. Reilly, and A. Tkatchenko, "First-principles modeling of molecular crystals: structures and stabilities, temperature and pressure," *WIREs Comput. Mol. Sci.*, vol. 7, p. e1294, jan 2017.

[106] C. Červinka, M. Fulem, R. P. Stoffel, and R. Dronskowski, "Thermodynamic Properties of Molecular Crystals Calculated within the Quasi-Harmonic Approximation," *J. Phys. Chem. A*, vol. 120, no. 12, pp. 2022–2034, 2016.

[107] C. Červinka and M. Fulem, "State-of-The-Art Calculations of Sublimation Enthalpies for Selected Molecular Crystals and Their Computational Uncertainty," *J. Chem. Theory Comput.*, vol. 13, no. 6, pp. 2840–2850, 2017.

[108] C. Červinka and G. J. O. Beran, "Towards reliable ab initio sublimation pressures for organic molecular crystals—Are we there yet?," *Phys. Chem. Chem. Phys.*, vol. 21, pp. 14799–14810, 2019.

[109] Y. N. Heit, K. D. Nanda, and G. J. O. Beran, "Predicting finite-temperature properties of crystalline carbon dioxide from first principles with quantitative accuracy," *Chem. Sci.*, vol. 7, pp. 246–255, 2016.

[110] M. A. Salim, S. Y. Willow, and S. Hirata, "Ice Ih anomalies: Thermal contraction, anomalous volume isotope effect, and pressure-induced amorphization," *J. Chem. Phys.*, vol. 144, p. 204503, may 2016.

[111] M. T. Ruggiero, J. A. Zeitler, and A. Erba, "Intermolecular anharmonicity in molecular crystals: interplay between experimental low-frequency dynamics and quantum quasi-harmonic simulations of solid purine," *Chemical Communications*, vol. 53, no. 26, pp. 3781–3784, 2017.

[112] W. Sontising, Y. N. Heit, J. L. McKinley, and G. J. O. Beran, "Theoretical predictions suggest carbon dioxide phases III and VII are identical," *Chem. Sci.*, vol. 8, pp. 7374–7382, 2017.

[113] J. L. McKinley and G. J. O. Beran, "Improving predicted nuclear magnetic resonance chemical shifts using the quasi-harmonic approximation," *J. Chem. Theory Comput.*, vol. 15, pp. 5259–5274, 2019.

[114] E. C. Dybeck, N. S. Abraham, N. P. Schieber, and M. R. Shirts, "Capturing Entropic Contributions to Temperature-Mediated Polymorphic Transformations Through Molecular Modeling," *Cryst. Growth Des.*, vol. 17, no. 4, pp. 1775–1787, 2017.

[115] N. P. Schieber, E. C. Dybeck, and M. R. Shirts, "Using reweighting and free energy surface interpolation to predict solid-solid phase diagrams," *J. Chem. Phys.*, vol. 148, p. 144104, apr 2018.

[116] E. C. Dybeck, D. P. McMahon, G. M. Day, and M. R. Shirts, "Exploring the Multiminima Behavior of Small Molecule Crystal Polymorphs at Finite Temperature," *Cryst. Growth Des.*, vol. 19, pp. 5568–5580, oct 2019.

[117] N. S. Abraham and M. R. Shirts, "Adding Anisotropy to the Standard Quasi-Harmonic Approximation Still Fails in Several Ways to Capture Organic Crystal Thermodynamics," *Cryst. Growth Des.*, vol. 19, pp. 6911–6924, dec 2019.

[118] M. Born and K. Huang, *Dynamical Theory of Crystal Lattices*. Clarendon Press, 1954.

[119] A. M. Reilly and A. Tkatchenko, "Understanding the role of vibrations, exact exchange, and many-body van der Waals interactions in the cohesive properties of molecular crystals.," *J. Chem. Phys.*, vol. 139, p. 024705, jul 2013.

[120] J. Hoja and A. Tkatchenko, "First-principles stability ranking of molecular crystal polymorphs with the DFT+MBD approach," *Faraday Disc.*, vol. 211, pp. 253–274, 2018.

[121] S. Baroni, S. de Gironcoli, A. Dal Corso, and P. Giannozzi, "Phonons and related crystal properties from density functional perturbation theory," *Rev. Mod. Phys.*, vol. 73, pp. 516–562, 2001.

[122] J. L. McKinley and G. J. O. Beran, "Identifying pragmatic quasi-harmonic electronic structure approaches for modeling molecular crystal thermal expansion," *Faraday Disc.*, vol. 211, pp. 181–207, 2018.

[123] M. Elstner and G. Seifert, "Density functional tight binding," *Philos. Trans. Roy. Soc. A*, vol. 372, no. 2011, pp. 20120483–20120483, 2014.

[124] A. S. Christensen, T. Kubař, Q. Cui, and M. Elstner, "Semiempirical Quantum Mechanical Methods for Noncovalent Interactions for Chemical and Biochemical Applications," *Chem. Rev.*, vol. 116, pp. 5301–5337, may 2016.

[125] M. Gaus, Q. Cui, and M. Elstner, "DFTB3: Extension of the self-consistent-charge density-functional tight-binding method (SCC-DFTB)," *J. Chem. Theory Comput.*, vol. 7, no. 4, pp. 931–948, 2011.

[126] J. Řezáč, "Empirical Self-Consistent Correction for the Description of Hydrogen Bonds in DFTB3," *J. Chem. Theory Comput.*, vol. 13, pp. 4804–4817, oct 2017.

[127] M. Mortazavi, J. G. Brandenburg, R. J. Maurer, and A. Tkatchenko, "Structure and Stability of Molecular Crystals with Many-Body Dispersion-Inclusive Density Functional Tight Binding," *J. Phys. Chem. Lett.*, vol. 9, pp. 399–405, jan 2018.

[128] J. G. Brandenburg, J. Potticary, H. A. Sparkes, S. L. Price, and S. R. Hall, "Thermal Expansion of Carbamazepine: Systematic Crystallographic Measurements Challenge Quantum Chemical Calculations," *J. Phys. Chem. Lett.*, vol. 8, no. 17, pp. 4319–4324, 2017.

[129] L. Iuzzolino, P. McCabe, S. L. Price, and J. G. Brandenburg, "Crystal structure prediction of flexible pharmaceutical-like molecules: density functional tight-binding as an intermediate optimisation method and for free energy estimation," *Faraday Discussions*, vol. 211, pp. 275–296, 2018.

[130] G. A. Dolgonos, O. A. Loboda, and A. D. Boese, "Development of Embedded and Performance of Density Functional Methods for Molecular Crystals," *J. Phys. Chem. A*, vol. 122, no. 2, pp. 708–713, 2018.

[131] J. G. Brandenburg, M. Hochheim, T. Bredow, and S. Grimme, "Low-Cost Quantum Chemical Methods for Noncovalent Interactions," *J. Phys. Chem. Lett.*, vol. 5, pp. 4275–4284, dec 2014.

[132] J. G. Brandenburg and S. Grimme, "Accurate Modeling of Organic Molecular Crystals by Dispersion-Corrected Density Functional Tight Binding (DFTB)," *J. Phys. Chem. Lett.*, vol. 5, pp. 1785–1789, jun 2014.

[133] J. G. Brandenburg, T. Maas, and S. Grimme, "Benchmarking DFT and semiempirical methods on structures and lattice energies for ten ice polymorphs," *The Journal of Chemical Physics*, vol. 142, p. 124104, mar 2015.

[134] J. G. Brandenburg and S. Grimme, "Organic crystal polymorphism: A benchmark for dispersion-corrected mean-field electronic structure methods," *Acta Cryst. B*, vol. 72, no. 4, pp. 502–513, 2016.

[135] D. Alfe, "PHON: A program to calculate phonons using the small displacement method," *Comput. Phys. Comm.*, vol. 180, pp. 2622–2633, dec 2009.

[136] M. Gaus, A. Goez, and M. Elstner, "Parametrization and Benchmark of DFTB3 for Organic Molecules," *J. Chem. Theory Comput.*, vol. 9, pp. 338–354, jan 2013.

[137] J. Reissland, "The physics of phonons," 1973.

[138] W. H. Keesom and J. W. Köhler, "The lattice constant and expansion coefficient of solid carbon dioxide," *Physica*, vol. 1, no. 7-12, pp. 655–658, 1934.

[139] I. Nahringbauer, "Hydrogen bond studies. 39. Reinvestigation of the crystal structure of acetic acid (at +5 degrees C and -190 degrees C)," *Acta Chem. Scand. A*, vol. 24, pp. 453–462, 1970.

[140] R. K. McMullan, J. Epstein, J. R. Ruble, and B. M. Craven, "The crystal structure of imidazole at 103 K by neutron diffraction," *Acta Cryst. B*, vol. 35, pp. 688–691, mar 1979.

[141] M. Haisa, S. Kashino, R. Kawai, and H. Maeda, "The Monoclinic Form of *p*-Hydroxyacetanilide," *Acta Cryst. B*, vol. 32, pp. 1283–1285, 1976.

[142] S. Ahn, F. Guo, B. M. Kariuki, and K. D. M. Harris, "Abundant polymorphism in a system with multiple hydrogen-bonding opportunities: oxalyl dihydrazide.," *J. Am. Chem. Soc.*, vol. 128, pp. 8441–52, jul 2006.

[143] A. Otero-De-La-Roza, B. H. Cao, I. K. Price, J. E. Hein, and E. R. Johnson, "Predicting the relative solubilities of racemic and enantiopure crystals by density-functional theory," *Angew. Chem. Int. Ed.*, vol. 53, no. 30, pp. 7879–7882, 2014.

[144] W. Setyawan and S. Curtarolo, "High-throughput electronic band structure calculations: Challenges and tools," *Comput. Mater. Sci.*, vol. 49, no. 2, pp. 299–312, 2010.

[145] D. Corso, Thermo_pw, `https://dalcorso.github.io/thermo_pw`.

[146] X. Tan, K. Wang, T. Yan, X. Li, J. Liu, K. Yang, B. Liu, G. Zou, and B. Zou, "Discovery of High-Pressure Polymorphs for a Typical Polymorphic System: Oxalyl Dihydrazide," *J. Phys. Chem. C*, vol. 119, pp. 10178–10188, may 2015.

[147] P. G. Karamertzanis, G. M. Day, G. W. A. Welch, J. Kendrick, F. J. J. Leusen, M. A. Neumann, and S. L. Price, "Modeling the interplay of inter- and intramolecular hydrogen bonding in conformational polymorphs.," *J. Chem. Phys.*, vol. 128, p. 244708, jun 2008.

[148] S. Wen and G. J. O. Beran, "Crystal polymorphism in oxalyl dihydrazide: Is empirical DFT-D accurate enough?," *J. Chem. Theory Comput.*, vol. 8, pp. 2698–2705, 2012.

[149] D. Presti, A. Pedone, M. C. Menziani, B. Civalleri, and L. Maschio, "Oxalyl dihydrazide polymorphism: a periodic dispersion-corrected DFT and MP2 investigation," *CrystEngComm*, vol. 16, no. 1, pp. 102–109, 2014.

[150] S. Grimme, C. Bannwarth, and P. Shushkov, "A Robust and Accurate Tight-Binding Quantum Chemical Method for Structures, Vibrational Frequencies, and Noncovalent Interactions of Large Molecular Systems Parametrized for All spd-Block Elements (Z = 1-86)," *J. Chem. Theory Comput.*, vol. 13, pp. 1989–2009, may 2017.

[151] J. G. Brandenburg, C. Bannwarth, A. Hansen, and S. Grimme, "B97-3c: A revised low-cost variant of the B97-D density functional method," *J. Chem. Phys.*, vol. 148, p. 064104, feb 2018.

[152] L. M. LeBlanc and E. R. Johnson, "Crystal-energy landscapes of active pharmaceutical ingredients using composite approaches," *CrystEngComm*, vol. 21, no. 40, pp. 5995–6009, 2019.

[153] G. M. Day, T. G. Cooper, A. J. Cruz-Cabeza, K. E. Hejczyk, H. L. Ammon, S. X. M. Boerrigter, J. S. Tan, R. G. Della Valle, E. Venuti, J. Jose, S. R. Gadre, G. R. Desiraju, T. S. Thakur, B. P. van Eijck, J. C. Facelli, V. E. Bazterra, M. B. Ferraro, D. W. M. Hofmann, M. A. Neumann, F. J. J. Leusen, J. Kendrick, S. L. Price, A. J. Misquitta, P. G. Karamertzanis, G. W. A. Welch, H. A. Scheraga, Y. A. Arnautova, M. U. Schmidt, J. van de Streek, A. K. Wolf, and B. Schweizer, "Significant progress in predicting the crystal structures of small organic molecules—A report on the fourth blind test.," *Acta Cryst. B*, vol. 65, pp. 107–125, apr 2009.

[154] M. A. Neumann, F. J. J. Leusen, and J. Kendrick, "A major advance in crystal structure prediction," *Angew. Chem. Int. Ed.*, vol. 47, no. 13, pp. 2427–2430, 2008.

[155] A. Asmadi, M. A. Neumann, J. Kendrick, P. Girard, M. A. Perrin, and F. J. J. Leusen, "Revisiting the blind tests in crystal structure prediction: Accurate energy ranking of molecular crystals," *J. Phys. Chem. B*, vol. 113, no. 51, pp. 16303–16313, 2009.

[156] S. L. Price and S. M. Reutzel-Edens, "The potential of computed crystal energy landscapes to aid solid-form development," *Drug Disc. Today*, vol. 21, pp. 912–923, jun 2016.

[157] S. L. Price, D. E. Braun, and S. M. Reutzel-Edens, "Can computed crystal energy landscapes help understand pharmaceutical solids?," *Chem. Commun.*, vol. 52, no. 2012, pp. 7065–7077, 2016.

[158] D. E. Braun, J. A. McMahon, L. H. Koztecki, S. L. Price, and S. M. Reutzel-Edens, "Contrasting Polymorphism of Related Small Molecule Drugs Correlated and Guided by the Computed Crystal Energy Landscape," *Cryst. Growth Des.*, vol. 14, pp. 2056–2072, apr 2014.

[159] M. A. Neumann, J. van de Streek, F. P. A. Fabbiani, P. Hidber, and O. Grassmann, "Combined crystal structure prediction and high-pressure crystallization in rational pharmaceutical polymorph screening," *Nature Commun.*, vol. 6, no. May, p. 7793, 2015.

[160] D. E. Braun, S. R. Lingireddy, M. D. Beidelschies, R. Guo, P. Müller, S. L. Price, and S. M. Reutzel-Edens, "Unraveling complexity in the solid form screening of a pharmaceutical salt: Why so many forms? Why so few?," *Cryst. Growth Des.*, vol. 17, no. 10, pp. 5349–5365, 2017.

[161] G. R. Woollam, M. A. Neumann, T. Wagner, and R. J. Davey, "The importance of configurational disorder in crystal structure prediction: the case of loratadine," *Faraday Disc.*, vol. 211, pp. 209–234, 2018.

[162] R. M. Bhardwaj, J. A. McMahon, J. Nyman, L. S. Price, S. Konar, I. D. H. Oswald, C. R. Pulham, S. L. Price, and S. M. Reutzel-Edens, "A Prolific Solvate Former, Galunisertib, under the Pressure of Crystal Structure Prediction, Produces Ten Diverse Polymorphs," *J. Am. Chem. Soc.*, vol. 141, pp. 13887–13897, sep 2019.

[163] M. Mortazavi, J. Hoja, L. Aerts, L. Quéré, J. van de Streek, M. A. Neumann, and A. Tkatchenko, "Computational polymorph screening reveals late-appearing and poorly-soluble form of rotigotine," *Commun. Chem.*, vol. 2, p. 80, dec 2019.

[164] S. Askin, J. K. Cockcroft, L. S. Price, A. D. Gonçalves, M. Zhao, D. A. Tocher, G. R. Williams, S. Gaisford, and D. Q. Craig, "Olanzapine Form IV: Discovery of a New Polymorphic Form Enabled by Computed Crystal Energy Landscapes," *Cryst. Growth Des.*, vol. 19, no. 5, pp. 2751–2757, 2019.

[165] S. L. Price, "Why don't we find more polymorphs?," *Acta Cryst. B*, vol. 69, no. Pt 4, pp. 313–28, 2013.

[166] W. C. McCrone, vol. 2, pp. 725–767. New York: Wiley Interscience, 1965.

[167] M. Vasileiadis, A. V. Kazantsev, P. G. Karamertzanis, C. S. Adjiman, and C. C. Pantelides, "The polymorphs of ROY: application of a systematic crystal structure prediction technique," *Acta Cryst. B*, vol. 68, pp. 677–685, dec 2012.

[168] J. Nyman, L. Yu, and S. M. Reutzel-Edens, "Accuracy and reproducibility in crystal structure prediction: the curious case of ROY," *CrystEngComm*, vol. 21, no. 13, pp. 2080–2088, 2019.

[169] M. Vasileiadis, C. C. Pantelides, and C. S. Adjiman, "Prediction of the crystal structures of axitinib, a polymorphic pharmaceutical molecule," *Chem. Eng. Sci.*, vol. 121, pp. 60–76, jan 2015.

[170] A. R. Tyler, R. Ragbirsingh, C. J. McMonagle, P. G. Waddell, S. E. Heaps, J. W. Steed, P. Thaw, M. J. Hall, and M. R. Probert, "Encapsulated Nanodroplet Crystallization of Organic-Soluble Small Molecules," *Chem*, vol. 6, no. 7, pp. 1755–1765, 2020.

[171] X. Li, X. Ou, H. Rong, S. Huang, J. Nyman, L. Yu, and M. Lu, "The Twelfth Solved Structure of ROY: Single Crystals of Y04 Grown from Melt Microdroplets," *Cryst. Growth Des.*, vol. 20, pp. 7093–7097, nov 2020.

[172] S. L. Price, "Is zeroth order crystal structure prediction (CSP_0) coming to maturity? What should we aim for in an ideal crystal structure prediction code?," *Faraday Disc.*, vol. 211, pp. 9–30, 2018.

[173] P. Raiteri, R. Martonák, and M. Parrinello, "Exploring polymorphism: the case of benzene.," *Angew. Chem. Int. Ed.*, vol. 44, pp. 3769–73, jun 2005.

[174] N. F. Francia, L. S. Price, J. Nyman, S. L. Price, and M. Salvalaglio, "Systematic Finite-Temperature Reduction of Crystal Energy Landscapes," *Cryst. Growth Des.*, vol. 20, pp. 6847–6862, oct 2020.

[175] N. S. Abraham and M. R. Shirts, "Thermal Gradient Approach for the Quasi-harmonic Approximation and Its Application to Improved Treatment of Anisotropic Expansion," *J. Chem. Theory Comput.*, vol. 14, pp. 5904–5919, nov 2018.

[176] T.-Q. Yu and M. Tuckerman, "Temperature-Accelerated Method for Exploring Polymorphism in Molecular Crystals Based on Free Energy," *Phys. Rev. Lett.*, vol. 107, p. 015701, jun 2011.

[177] E. Schneider, L. Vogt, and M. E. Tuckerman, "Exploring polymorphism of benzene and naphthalene with free energy based enhanced molecular dynamics," *Acta Cryst. B*, vol. 72, pp. 542–550, aug 2016.

[178] M. Rossi, P. Gasparotto, and M. Ceriotti, "Anharmonic and Quantum Fluctuations in Molecular Crystals: A First-Principles Study of the Stability of Paracetamol," *Physical Review Letters*, vol. 117, no. 11, pp. 1–6, 2016.

[179] N. Raimbault, V. Athavale, and M. Rossi, "Anharmonic effects in the low-frequency vibrational modes of aspirin and paracetamol crystals," *Physical Review Materials*, vol. 3, no. 5, pp. 1–11, 2019.

[180] H. Y. Ko, R. A. Distasio, B. Santra, and R. Car, "Thermal expansion in dispersion-bound molecular crystals," *Phys. Rev. Mater.*, vol. 2, no. 5, pp. 1–7, 2018.

[181] B. Cheng, E. A. Engel, J. Behler, C. Dellago, and M. Ceriotti, "Ab initio thermodynamics of liquid and solid water," *Proceedings of the National Academy of Sciences of the United States of America*, vol. 116, no. 4, pp. 1110–1115, 2019.

[182] Y. Abramov, G. Sun, Y. Zhou, M. Yang, Q. Zeng, and Z. Shen, "Solid-Form Transition Temperature Prediction from a Virtual Polymorph Screening: A Reality Check," *Cryst. Growth Des.*, vol. 19, pp. 7132–7137, dec 2019.

[183] S. A. Bonev, F. Gygi, T. Ogitsu, and G. Galli, "High-Pressure Molecular Phases of Solid Carbon Dioxide," *Phys. Rev. Lett.*, vol. 91, p. 065501, aug 2003.

[184] J. Li, O. Sode, G. A. Voth, and S. Hirata, "A solid-solid phase transition in carbon dioxide at high pressures and intermediate temperatures.," *Nature Commun.*, vol. 4, p. 2647, jan 2013.

[185] Y. Han, J. Liu, L. Huang, X. He, and J. Li, "Predicting the phase diagram of solid carbon dioxide at high pressure from first principles," *npj Quantum Materials*, vol. 4, p. 10, dec 2019.

[186] Y. Han, J. Liu, and J. Li, "Molecular structure determination of solid carbon dioxide phase IV at high pressures and temperatures based on Møller-Plesset perturbation theory," *Int. J. Quant. Chem.*, vol. 120, no. 23, pp. 1–9, 2020.

[187] L. Huang, Y. Han, X. He, and J. Li, "Ab initio-enabled phase transition prediction of solid carbon dioxide at ultra-high temperatures," *RSC Advances*, vol. 10, no. 1, pp. 236–243, 2020.

[188] Y. Han, Z. Wang, and J. Li, "Neural Networks Accelerate the Ab Initio Prediction of Solid-Solid Phase Transitions at High Pressures," *J. Phys. Chem. Lett.*, pp. 132–137, dec 2021.

[189] Q. Lu, I. Ali, and J. Li, "Prediction of properties from first principles with quantitative accuracy: Six representative ice phases," *New J. Chem.*, vol. 44, no. 48, pp. 21012–21020, 2020.

[190] J. Xu, J. Liu, J. Liu, W. Hu, X. He, and J. Li, "Phase transition of ice at high pressures and low temperatures," *Molecules*, vol. 25, no. 3, pp. 1–14, 2020.

[191] J. Kotakoski and K. Albe, "First-principles calculations on solid nitrogen: A comparative study of high-pressure phases," *Phys. Rev. B*, vol. 77, p. 144109, apr 2008.

[192] C. J. Pickard and R. J. Needs, "High-Pressure Phases of Nitrogen," *Phys. Rev. Lett.*, vol. 102, no. 12, p. 125702, 2009.

[193] A. Erba, L. Maschio, C. Pisani, and S. Casassa, "Pressure-induced transitions in solid nitrogen: Role of dispersive interactions," *Phys. Rev. B*, vol. 84, p. 012101, jul 2011.

[194] A. Erba, L. Maschio, S. Salustro, and S. Casassa, "A post-Hartree-Fock study of pressure-induced phase transitions in solid nitrogen: The case of the α, γ, and ϵ low-pressure phases," *J. Chem. Phys.*, vol. 134, no. 7, p. 074502, 2011.

[195] D. Plašienka and R. Martonák, "Transformation pathways in high-pressure solid nitrogen: From molecular N_2 to polymeric cg-N," *J. Chem. Phys.*, vol. 142, p. 094505, 2015.

[196] W. Sontising and G. J. O. Beran, "Theoretical assessment of the structure and stability of the λ phase of nitrogen," *Phys. Rev. Mater.*, vol. 3, p. 095002, 2019.

[197] X.-D. Wen, R. Hoffmann, and N. W. Ashcroft, "Benzene under High Pressure: a Story of Molecular Crystals Transforming to Saturated Networks, with a Possible Intermediate Metallic Phase," *J. Am. Chem. Soc.*, vol. 133, pp. 9023–9035, 2011.

[198] C. Cook and G. J. O. Beran, "Reduced-cost supercell approach for computing accurate phonon density of states in organic crystals," *J. Chem. Phys.*, p. accepted, 2020.

[199] H. K. Buchholz, R. K. Hylton, J. G. Brandenburg, A. Seidel-Morgenstern, H. Lorenz, M. Stein, and S. L. Price, "Thermochemistry of Racemic and Enantiopure Organic Crystals for Predicting Enantiomer Separation," *Cryst. Growth Des.*, vol. 17, pp. 4676–4686, sep 2017.

[200] E. H. Lee, "A practical guide to pharmaceutical polymorph screening & selection," *Asian J. Pharm. Sci.*, vol. 9, pp. 163–175, aug 2014.

[201] Y. Ebisuzaki, L. H. Askari, A. M. Bryan, and M. F. Nicol, "Phase transitions in resorcinal," *J. Chem. Phys.*, vol. 87, pp. 6659–6664, dec 1987.

[202] S. K. Deb, M. A. Rekha, A. P. Roy, V. Vijayakumar, S. Meenakshi, and B. K. Godwal, "Raman-scattering study of high-pressure phase transition and amorphization of resorcinol," *Phys. Rev. B*, vol. 47, pp. 11491–11494, may 1993.

[203] R. Rao, T. Sakuntala, and B. K. Godwal, "Evidence for high-pressure polymorphism in resorcinol," *Phys. Rev. B*, vol. 65, no. 5, pp. 1–8, 2002.

[204] Q. Zhu, A. G. Shtukenberg, D. J. Carter, T.-Q. Yu, J. Yang, M. Chen, P. Raiteri, A. R. Oganov, B. Pokroy, I. Polishchuk, P. J. Bygrave, G. M. Day, A. L. Rohl, M. E. Tuckerman, and B. Kahr, "Resorcinol Crystallization from the Melt: A New Ambient Phase and New "Riddles"," *J. Am. Chem. Soc.*, vol. 138, pp. 4881–4889, apr 2016.

[205] A. Erba, "On combining temperature and pressure effects on structural properties of crystals with standard ab initio techniques," *J. Chem. Phys.*, vol. 141, no. 12, 2014.

[206] J. Nyman, O. Sheehan Pundyke, and G. M. Day, "Accurate force fields and methods for modelling organic molecular crystals at finite temperatures," *Phys. Chem. Chem. Phys.*, vol. 18, pp. 15828–15837, 2016.

[207] L. Monacelli, I. Errea, M. Calandra, and F. Mauri, "Pressure and stress tensor of complex anharmonic crystals within the stochastic self-consistent harmonic approximation," *Phys. Rev. B*, vol. 98, p. 024106, jul 2018.

[208] F.R.Fronczek, "Ccdc 168981: Experimental crystal structure determination," 2001.

[209] G. E. Bacon and E. J. Lisher, "A neutron powder diffraction study of deuterated α- and β-resorcinol," *Acta Crystallographica Section B Structural Crystallography and Crystal Chemistry*, vol. 36, no. 8, pp. 1908–1916, 1980.

[210] P. Giannozzi, O. Andreussi, T. Brumme, O. Bunau, M. Buongiorno Nardelli, M. Calandra, R. Car, C. Cavazzoni, D. Ceresoli, M. Cococcioni, N. Colonna, I. Carnimeo, A. Dal Corso, S. de Gironcoli, P. Delugas, R. A. DiStasio, A. Ferretti, A. Floris, G. Fratesi, G. Fugallo, R. Gebauer, U. Gerstmann, F. Giustino, T. Gorni, J. Jia, M. Kawamura, H.-Y. Ko, A. Kokalj, E. Küçükbenli, M. Lazzeri, M. Marsili, N. Marzari, F. Mauri, N. L. Nguyen, H.-V. Nguyen, A. Otero-de-la Roza, L. Paulatto, S. Poncé, D. Rocca, R. Sabatini, B. Santra, M. Schlipf, A. P. Seitsonen, A. Smogunov, I. Timrov, T. Thonhauser, P. Umari, N. Vast, X. Wu, and S. Baroni, "Advanced capabilities for materials modelling with Quantum ESPRESSO," *J. Phys. Condens. Mat.*, vol. 29, p. 465901, nov 2017.

[211] A. D. Becke, "On the large-gradient behavior of the density functional exchange energy," *J. Chem. Phys.*, vol. 38, pp. 7184–7187, 1986.

[212] H. J. Monkhorst and J. D. Pack, "Special points for Brillouin-zone integrations," *Phys. Rev. B*, vol. 13, pp. 5188–5192, 1976.

[213] Y. Q. Cheng, L. L. Daemen, A. I. Kolesnikov, and A. J. Ramirez-Cuesta, "Simulation of Inelastic Neutron Scattering Spectra Using OCLIMAX," *Journal of Chemical Theory and Computation*, vol. 15, no. 3, pp. 1974–1982, 2019.

[214] N. S. Abraham and M. R. Shirts, "Thermal Gradient Approach for the Quasi-harmonic Approximation and Its Application to Improved Treatment of Anisotropic Expansion," *Journal of Chemical Theory and Computation*, vol. 14, no. 11, pp. 5904–5919, 2018.

[215] A. Otero-de-la Roza and E. R. Johnson, "A benchmark for non-covalent interactions in solids," *J. Chem. Phys.*, vol. 137, no. 5, p. 054103, 2012.

[216] J. George, R. Wang, U. Englert, and R. Dronskowski, "Lattice thermal expansion and anisotropic displacements in urea, bromomalonic aldehyde, pentachloropyridine, and naphthalene," *Journal of Chemical Physics*, vol. 147, no. 7, 2017.

[217] H. Lautz, "," *Z. Phys. Chem.*, vol. 84, p. 611, 1913.

[218] J. M. Robertson and A. R. Ubbelohde, "A new form of resorcinol. II. Thermodynamic properties in relation to structure," *Proc. R. Soc. Lond. A*, vol. 167, pp. 136–147, 1938.

[219] P. Bret-Dibat and A. Lichanot, "Proprietes thermodynamiques des isomeres de position de benzenes disubstitues en phase condensee," *Thermochimica Acta*, vol. 147, pp. 261–271, jul 1989.

[220] K. L. Wolf and H. G. Trieschmann, "Über Sublimationswärmen organischer Moleküle," *Z. Phys. Chem. B*, vol. 27, pp. 376–380, 1934.

[221] H. Hoyer and W. Peperle, "," *Z. Electrochem.*, vol. 62, pp. 61–66, 1958.

[222] R. Bender, V. Bieling, and G. Maurer, "The vapour pressures of solids: Anthracene, hydroquinone, and resorcinol," *J. Chem. Thermo.*, vol. 15, pp. 585–594, 1983.

[223] R. Sabbah and E. N. L. E. Buluku, "Étude thermodynamique des trois isomres du dihydroxybenzne," *Can. J. Chem.*, vol. 69, pp. 481–488, 1991.

[224] V. I. Smirnov, G. L. Perlovich, and A. Y. Fridman, "," *Zh. Fiz. Kim.*, vol. 66, pp. 615–619, 1992.

[225] S. P. Verevkin and S. A. Kozlova, "Di-hydroxybenzenes: Catechol, resorcinol, and hydroquinone. Enthalpies of phase transitions revisited," *Thermochimica Acta*, vol. 471, no. 1-2, pp. 33–42, 2008.

[226] W. Acree and J. S. Chickos, "Phase Transition Enthalpy Measurements of Organic and Organometallic Compounds. Sublimation, Vaporization and Fusion Enthalpies From 1880 to 2010," *J. Phys. Chem. Ref. Data*, vol. 39, no. 4, p. 043101, 2010.

[227] E. M. Gonçalves, F. Agapito, T. S. Almeida, and J. A. Martinho Simões, "Enthalpies of formation of dihydroxybenzenes revisited: Combining experimental and high-level ab initio data," *J. Chem. Thermo.*, vol. 73, pp. 90–96, 2014.

[228] J. H. Lloyd-Williams and B. Monserrat, "Lattice dynamics and electron-phonon coupling calculations using nondiagonal supercells," *Physical Review B - Condensed Matter and Materials Physics*, vol. 92, no. 18, pp. 1–9, 2015.

[229] PAYWALL., "Organic semiconductor market research report, by type (polyethylene, poly aromatic ring and copolymer) application (system component, organic photovoltaic (opv), oled lighting, printed batteries, organic rfid tags and display applications) region (north america, europe, asia-pacific, middle east and africa, central and south america)—forecast till 2027," 2021.

[230] M. Klues and G. Witte, "Crystalline packing in pentacene-like organic semiconductors," *CrystEngComm*, vol. 20, no. 1, pp. 63–74, 2018.

[231] S. Fratini, M. Nikolka, A. Salleo, G. Schweicher, and H. Sirringhaus, "Charge transport in high-mobility conjugated polymers and molecular semiconductors," *Nature Materials*, vol. 19, no. 5, pp. 491–502, 2020.

[232] N. E. Lee, J. J. Zhou, L. A. Agapito, and M. Bernardi, "Charge transport in organic molecular semiconductors from first principles: The bandlike hole mobility in a naphthalene crystal," *Physical Review B*, vol. 97, no. 11, pp. 1–8, 2018.

[233] H. Oberhofer, K. Reuter, and J. Blumberger, "Charge Transport in Molecular Materials: An Assessment of Computational Methods," *Chemical Reviews*, vol. 117, no. 15, pp. 10319–10357, 2017.

[234] R. Oshi, S. Abdalla, and M. Springborg, "Study of the influence of functionalization on the reorganization energy of naphthalene using DFT," *Computational and Theoretical Chemistry*, vol. 1099, pp. 209–215, 2017.

[235] J. L. Brédas, J. P. Calbert, D. A. Da Silva Filho, and J. Cornil, "Organic semiconductors: A theoretical characterization of the basic parameters governing charge transport," *Proceedings of the National Academy of Sciences of the United States of America*, vol. 99, no. 9, pp. 5804–5809, 2002.

[236] G. Schweicher, G. D'Avino, M. T. Ruggiero, D. J. Harkin, K. Broch, D. Venkateshvaran, G. Liu, A. Richard, C. Ruzié, J. Armstrong, A. R. Kennedy, K. Shankland, K. Takimiya, Y. H. Geerts, J. A. Zeitler, S. Fratini, and H. Sirringhaus, "Chasing the "Killer" Phonon Mode for the Rational Design of Low-Disorder, High-Mobility Molecular Semiconductors," *Adv. Mater.*, vol. 31, p. 1902407, oct 2019.

[237] T. Nematiaram, S. Ciuchi, X. Xie, S. Fratini, and A. Troisi, "Practical Computation of the Charge Mobility in Molecular Semiconductors Using Transient Localization Theory," *Journal of Physical Chemistry C*, vol. 123, no. 12, pp. 6989–6997, 2019.

[238] R. G. Della Valle, E. Venuti, L. Farina, A. Brillante, M. Masino, and A. Girlando, "Intramolecular and Low-Frequency Intermolecular Vibrations of Pentacene Polymorphs as a Function of Temperature," *Journal of Physical Chemistry B*, vol. 108, no. 6, pp. 1822–1826, 2004.

[239] S. Fratini, S. Ciuchi, D. Mayou, G. T. De Laissardière, and A. Troisi, "A map of high-mobility molecular semiconductors," *Nature Materials*, vol. 16, no. 10, pp. 998–1002, 2017.

[240] A. Troisi and G. Orlandi, "Band structure of the four pentacene polymorphs and effect on the hole mobility at low temperature.," *J. Phys. Chem. B*, vol. 109, pp. 1849–56, feb 2005.

[241] T. F. Harrelson, V. Dantanarayana, X. Xie, C. Koshnick, D. Nai, R. Fair, S. A. Nuñez, A. K. Thomas, T. L. Murrey, M. A. Hickner, J. K. Grey, J. E. Anthony,

E. D. Gomez, A. Troisi, R. Faller, and A. J. Moulé, "Direct probe of the nuclear modes limiting charge mobility in molecular semiconductors," *Materials Horizons*, vol. 6, no. 1, pp. 182–191, 2019.

[242] W. Shi, Z. M. Wong, T. Deng, G. Wu, and S. W. Yang, "Unravelling the Molecular Origin of Organic Semiconductors with High-Performance Thermoelectric Response," *Advanced Functional Materials*, vol. 31, no. 9, pp. 1–11, 2021.

[243] D. Käfer, M. El Helou, C. Gemel, and G. Witte, "Packing of planar organic molecules: Interplay of van der waals and electrostatic interaction," *Crystal Growth and Design*, vol. 8, no. 8, pp. 3053–3057, 2008.

[244] P. A. Banks, J. Maul, M. T. Mancini, A. C. Whalley, A. Erba, and M. T. Ruggiero, "Thermoelasticity in organic semiconductors determined with terahertz spectroscopy and quantum quasi-harmonic simulations," *Journal of Materials Chemistry C*, vol. 8, no. 31, pp. 10917–10925, 2020.

[245] C. Cook, J. L. McKinley, and G. J. O. Beran, "Modeling the α- and β-resorcinol phase boundary via combination of density functional theory and density functional tight-binding," *J. Chem. Phys.*, vol. 154, p. 134109, 2021.

[246] A. Erba, J. Maul, R. Demichelis, and R. Dovesi, "Assessing thermochemical properties of materials through ab initio quantum-mechanical methods: The case of α-Al2O3," *Physical Chemistry Chemical Physics*, vol. 17, no. 17, pp. 11670–11677, 2015.

[247] J. L. Mckinley and G. J. O. Beran, "Faraday Discussions Identifying pragmatic quasi-harmonic electronic struc- ture approaches for modeling molecular crystal ther- mal expansion," 2018.

[248] C. C. Mattheus, A. B. Dros, J. Baas, A. Meetsma, J. L. De Boer, and T. T. Palstra, "Polymorphism in pentacene," *Acta Crystallographica Section C: Crystal Structure Communications*, vol. 57, no. 8, pp. 939–941, 2001.

[249] T. Siegrist, C. Besnard, S. Haas, M. Schiltz, P. Pattison, D. Chernyshov, B. Batlogg, and C. Kloc, "A polymorph lost and found: The high-temperature crystal structure of pentacene," *Advanced Materials*, vol. 19, no. 16, pp. 2079–2082, 2007.

[250] K. Choudhary and F. Tavazza, "Convergence and machine learning predictions of Monkhorst-Pack k-points and plane-wave cut-off in high-throughput DFT calculations," *Computational Materials Science*, vol. 161, no. January, pp. 300–308, 2019.

[251] P. Giannozzi, S. Baroni, N. Bonini, M. Calandra, R. Car, C. Cavazzoni, D. Ceresoli, G. L. Chiarotti, M. Cococcioni, I. Dabo, A. Dal Corso, S. De Gironcoli, S. Fabris, G. Fratesi, R. Gebauer, U. Gerstmann, C. Gougoussis, A. Kokalj, M. Lazzeri, L. Martin-Samos, N. Marzari, F. Mauri, R. Mazzarello, S. Paolini, A. Pasquarello,

L. Paulatto, C. Sbraccia, S. Scandolo, G. Sclauzero, A. P. Seitsonen, A. Smogunov, P. Umari, and R. M. Wentzcovitch, "QUANTUM ESPRESSO: A modular and open-source software project for quantum simulations of materials," *Journal of Physics Condensed Matter*, vol. 21, no. 39, 2009.

[252] A. Togo and I. Tanaka, "First principles phonon calculations in materials science," *Scripta Materialia*, vol. 108, pp. 1–5, 2015.

[253] W. Setyawan and S. Curtarolo, "High-throughput electronic band structure calculations: Challenges and tools," *Computational Materials Science*, vol. 49, no. 2, pp. 299–312, 2010.

[254] B. Rice, L. M. Leblanc, A. Otero-De-La-Roza, M. J. Fuchter, E. R. Johnson, J. Nelson, and K. E. Jelfs, "A computational exploration of the crystal energy and charge-carrier mobility landscapes of the chiral [6]helicene molecule," *Nanoscale*, vol. 10, no. 4, pp. 1865–1876, 2018.

[255] M. J. Frisch, G. W. Trucks, H. B. Schlegel, G. E. Scuseria, M. A. Robb, J. R. Cheeseman, G. Scalmani, V. Barone, B. Mennucci, G. A. Petersson, H. Nakatsuji, M. Caricato, X. Li, H. P. Hratchian, A. F. Izmaylov, J. Bloino, G. Zheng, J. L. Sonnenberg, M. Hada, M. Ehara, K. Toyota, R. Fukuda, J. Hasegawa, M. Ishida, T. Nakajima, Y. Honda, O. Kitao, H. Nakai, T. Vreven, J. A. Montgomery, Jr., J. E. Peralta, F. Ogliaro, M. Bearpark, J. J. Heyd, E. Brothers, K. N. Kudin, V. N. Staroverov, R. Kobayashi, J. Normand, K. Raghavachari, A. Rendell, J. C. Burant, S. S. Iyengar, J. Tomasi, M. Cossi, N. Rega, J. M. Millam, M. Klene, J. E. Knox, J. B. Cross, V. Bakken, C. Adamo, J. Jaramillo, R. Gomperts, R. E. Stratmann, O. Yazyev, A. J. Austin, R. Cammi, C. Pomelli, J. W. Ochterski, R. L. Martin, K. Morokuma, V. G. Zakrzewski, G. A. Voth, P. Salvador, J. J. Dannenberg, S. Dapprich, A. D. Daniels, Ö. Farkas, J. B. Foresman, J. V. Ortiz, J. Cioslowski, and D. J. Fox, "Gaussian 09 Revision E.01," 2009. Gaussian Inc. Wallingford CT.

[256] J. Brown, "Charge transport integral package (catnip)," 2019.

[257] C. P. Brock and J. D. Dunitz, "Towards a grammar of crystal packing," *Chem. Mater.*, vol. 6, pp. 1118–1127, 1994.

[258] S. C. Capelli, A. Albinati, S. A. Mason, and B. T. Willis, "Molecular motion in crystalline naphthalene: Analysis of multi-temperature X-ray and neutron diffraction data," *Journal of Physical Chemistry A*, vol. 110, no. 41, pp. 11695–11703, 2006.

[259] D. Holmes, "On the Nature of Nonplanarity in the [N]Phenylenes," *Chemistry a European Journal*, vol. 5, pp. 3399–3412, 1999.

[260] P. Naumov, D. P. Karothu, E. Ahmed, L. Catalano, P. Commins, J. Mahmoud Halabi, M. B. Al-Handawi, and L. Li, "The Rise of the Dynamic Crystals," *J. Am. Chem. Soc.*, vol. 142, pp. 13256–13272, aug 2020.

[261] T. Kim, L. Zhu, R. O. Al-Kaysi, and C. J. Bardeen, "Organic Photomechanical Materials," *ChemPhysChem*, vol. 15, pp. 400–414, feb 2014.

[262] T. J. White, ed., *Photomechanical Materials, Composites, and Systems*. Chichester, UK: Wiley, jul 2017.

[263] H. Koshima, ed., *Mechanically Responsive Materials for Soft Robotics*. Wiley, jan 2020.

[264] S. Kobatake, S. Takami, H. Muto, T. Ishikawa, and M. Irie, "Rapid and reversible shape changes of molecular crystals on photoirradiation," *Nature*, vol. 446, pp. 778–781, apr 2007.

[265] M. Morimoto and M. Irie, "A Diarylethene Cocrystal that Converts Light into Mechanical Work," *J. Am. Chem. Soc.*, vol. 132, pp. 14172–14178, oct 2010.

[266] H. Koshima, N. Ojima, and H. Uchimoto, "Mechanical Motion of Azobenzene Crystals upon Photoirradiation," *J. Am. Chem. Soc.*, vol. 131, pp. 6890–6891, may 2009.

[267] O. S. Bushuyev, A. Tomberg, T. Friščić, and C. J. Barrett, "Shaping Crystals with Light: Crystal-to-Crystal Isomerization and Photomechanical Effect in Fluorinated Azobenzenes," *J. Am. Chem. Soc.*, vol. 135, pp. 12556–12559, aug 2013.

[268] H. Wang, P. Chen, Z. Wu, J. Zhao, J. Sun, and R. Lu, "Bending, Curling, Rolling, and Salient Behavior of Molecular Crystals Driven by [2+2] Cycloaddition of a Styrylbenzoxazole Derivative," *Angew. Chem. Int. Ed.*, vol. 56, pp. 9463–9467, aug 2017.

[269] P. Naumov, J. Kowalik, K. M. Solntsev, A. Baldridge, J.-S. Moon, C. Kranz, and L. M. Tolbert, "Topochemistry and Photomechanical Effects in Crystals of Green Fluorescent Protein-like Chromophores: Effects of Hydrogen Bonding and Crystal Packing," *J. Am. Chem. Soc.*, vol. 132, pp. 5845–5857, apr 2010.

[270] J. M. Halabi, E. Ahmed, S. Sofela, and P. Naumov, "Performance of molecular crystals in conversion of light to mechanical work," *Proc. Nat. Acad. Sci.*, vol. 118, no. 5, pp. 1–7, 2021.

[271] D. Kitagawa, H. Tsujioka, F. Tong, X. Dong, C. J. Bardeen, and S. Kobatake, "Control of Photomechanical Crystal Twisting by Illumination Direction," *J. Am. Chem. Soc.*, vol. 140, no. 12, pp. 4208–4212, 2018.

[272] D.-K. Bučar and L. R. MacGillivray, "Preparation and Reactivity of Nanocrystalline Cocrystals Formed via Sonocrystallization," *J. Am. Chem. Soc.*, vol. 129, pp. 32–33, jan 2007.

[273] L. Zhu, A. Agarwal, J. Lai, R. O. Al-Kaysi, F. S. Tham, T. Ghaddar, L. Mueller, and C. J. Bardeen, "Solid-state photochemical and photomechanical properties of

molecular crystal nanorods composed of anthracene ester derivatives," *J. Mater. Chem.*, vol. 21, no. 17, pp. 6258–6268, 2011.

[274] T. Kim, L. Zhu, L. J. Mueller, and C. J. Bardeen, "Mechanism of photoinduced bending and twisting in crystalline microneedles and microribbons composed of 9-methylanthracene," *J. Am. Chem. Soc.*, vol. 136, no. 18, pp. 6617–6625, 2014.

[275] D. Kitagawa and S. Kobatake, "Crystal Thickness Dependence of Photoinduced Crystal Bending of 1,2-Bis(2-methyl-5-(4-(1-naphthoyloxymethyl)phenyl)-3-thienyl)perfluorocyclopentene," *J. Phys. Chem. C*, vol. 117, pp. 20887–20892, oct 2013.

[276] N. K. Nath, L. Pejov, S. M. Nichols, C. Hu, N. Saleh, B. Kahr, and P. Naumov, "Model for photoinduced bending of slender molecular crystals," *Journal of the American Chemical Society*, vol. 136, no. 7, pp. 2757–2766, 2014.

[277] S. Grimme, A. Hansen, J. G. Brandenburg, and C. Bannwarth, "Dispersion-Corrected Mean-Field Electronic Structure Methods," *Chem. Rev.*, vol. 116, no. 9, pp. 5105–5154, 2016.

[278] J. Hermann, R. A. DiStasio, and A. Tkatchenko, "First-Principles Models for van der Waals Interactions in Molecules and Materials: Concepts, Theory, and Applications," *Chem. Rev.*, vol. 117, no. 6, pp. 4714–4758, 2017.

[279] D. E. Braun, J. A. McMahon, R. M. Bhardwaj, J. Nyman, M. A. Neumann, J. Van De Streek, and S. M. Reutzel-Edens, "Inconvenient Truths about Solid Form Landscapes Revealed in the Polymorphs and Hydrates of Gandotinib," *Cryst. Growth Des.*, vol. 19, no. 5, pp. 2947–2962, 2019.

[280] D. H. Case, V. K. Srirambhatla, R. Guo, R. E. Watson, L. S. Price, H. Polyzois, J. K. Cockcroft, A. J. Florence, D. A. Tocher, and S. L. Price, "Successful Computationally Directed Templating of Metastable Pharmaceutical Polymorphs," *Cryst. Growth Des.*, vol. 18, no. 9, pp. 5322–5331, 2018.

[281] E. Schur, J. Bernstein, L. S. Price, R. Guo, S. L. Price, S. H. Lapidus, and P. W. Stephens, "The (Current) Acridine Solid Form Landscape: Eight Polymorphs and a Hydrate," *Cryst. Growth Des.*, vol. 19, no. 8, pp. 4884–4893, 2019.

[282] M.-A. Perrin, M. A. Neumann, H. Elmaleh, and L. Zaske, "Crystal structure determination of the elusive paracetamol Form III.," *Chem. Commun.*, pp. 3181–3, jun 2009.

[283] A. D. Bond, K. A. Solanko, J. van de Streek, and M. A. Neumann, "Experimental verification of a subtle low-temperature phase transition suggested by DFT-D energy minimisation," *CrystEngComm*, vol. 13, no. 6, p. 1768, 2011.

[284] G. Sun, X. Liu, Y. A. Abramov, S. O. Nilsson Lill, C. Chang, V. Burger, and A. Broo, "Current State-of-the-art In-house and Cloud-Based Applications of Virtual Polymorph Screening of Pharmaceutical Compounds: A Challenging Case of AZD1305," *Cryst. Growth Des.*, vol. 21, pp. 1972–1983, apr 2021.

[285] A. G. Shtukenberg, C. T. Hu, Q. Zhu, M. U. Schmidt, W. Xu, M. Tan, and B. Kahr, "The Third Ambient Aspirin Polymorph," *Cryst. Growth Des.*, vol. 17, no. 6, pp. 3562–3566, 2017.

[286] A. G. Shtukenberg, M. Tan, L. Vogt-Maranto, E. J. Chan, W. Xu, J. Yang, M. E. Tuckerman, C. T. Hu, and B. Kahr, "Melt Crystallization for Paracetamol Polymorphism," *Cryst. Growth Des.*, vol. 19, no. 7, pp. 4070–4080, 2019.

[287] E. L. Stevenson, R. W. Lancaster, A. B. M. Buanz, L. S. Price, D. A. Tocher, and S. L. Price, "The solid state forms of the sex hormone 17-β-estradiol," *CrystEngComm*, vol. 1875324, 2019.

[288] A. N. Sokolov, S. Atahan-Evrenk, R. Mondal, H. B. Akkerman, R. S. Sánchez-Carrera, S. Granados-Focil, J. Schrier, S. C. Mannsfeld, A. P. Zoombelt, Z. Bao, and A. Aspuru-Guzik, "From computational discovery to experimental characterization of a high hole mobility organic crystal," *Nature Commun.*, vol. 2, p. 437, sep 2011.

[289] E. O. Pyzer-Knapp, H. P. G. Thompson, F. Schiffmann, K. E. Jelfs, S. Y. Chong, M. A. Little, A. I. Cooper, and G. M. Day, "Predicted crystal energy landscapes of porous organic cages," *Chem. Sci.*, vol. 5, no. 6, pp. 2235–2245, 2014.

[290] E. Wolpert and K. Jelfs, "Coarse-grained modelling to predict the packing of porous organic cages," *chemRxiv*, 2022.

[291] A. Pulido, L. Chen, T. Kaczorowski, D. Holden, M. A. Little, S. Y. Chong, B. J. Slater, D. P. McMahon, B. Bonillo, C. J. Stackhouse, A. Stephenson, C. M. Kane, R. Clowes, T. Hasell, A. I. Cooper, and G. M. Day, "Functional materials discovery using energy-structure-function maps," *Nature*, vol. 543, pp. 657–664, mar 2017.

[292] P. Cui, D. P. McMahon, P. R. Spackman, B. M. Alston, M. A. Little, G. M. Day, and A. I. Cooper, "Mining predicted crystal structure landscapes with high throughput crystallisation: old molecules, new insights," *Chem. Sci.*, vol. 10, no. 43, pp. 9988–9997, 2019.

[293] R. L. Greenaway, V. Santolini, A. Pulido, M. A. Little, B. M. Alston, M. E. Briggs, G. M. Day, A. I. Cooper, and K. E. Jelfs, "From Concept to Crystals via Prediction: Multi-Component Organic Cage Pots by Social Self-Sorting," *Angew. Chem. Int. Ed.*, vol. 58, pp. 16275–16281, nov 2019.

[294] C. Y. Cheng, J. E. Campbell, and G. M. Day, "Evolutionary chemical space exploration for functional materials: computational organic semiconductor discovery," *Chem. Sci.*, vol. 11, no. 19, pp. 4922–4933, 2020.

[295] Q. Zhu, J. Johal, D. E. Widdowson, Z. Pang, B. Li, C. M. Kane, V. Kurlin, G. M. Day, M. A. Little, and A. I. Cooper, "Analogy Powered by Prediction and Structural Invariants: Computationally Led Discovery of a Mesoporous Hydrogen-Bonded Organic Cage Crystal," *J. Am. Chem. Soc.*, vol. 144, pp. 9893–9901, jun 2022.

[296] P. J. Stephens, F. J. Devlin, C. F. Chabalowski, and M. J. Frisch, "Ab initio calculation of vibrational absorption and circular dichroism spectra using density functional force fields," *J. Phys. Chem.*, vol. 98, pp. 11623–11627, 1994.

[297] A. F. Mabied, M. Müller, R. E. Dinnebier, S. Nozawa, M. Hoshino, A. Tomita, T. Sato, and S. I. Adachi, "A time-resolved powder diffraction study of in-situ photodimerization kinetics of 9-methylanthracene using a CCD area detector and parametric Rietveld refinement," *Acta Crystallographica Section B: Structural Science*, vol. 68, no. 4, pp. 424–430, 2012.

[298] J. A. Chisholm and W. D. S. Motherwell, "COMPACK: A program for identifying crystal structure similarity using distances," *J. Appl. Crystall.*, vol. 38, pp. 228–231, jan 2005.

[299] H. Ihmels, D. Leusser, M. Pfeiffer, and D. Stalke, "Solid-State Photolysis of Anthracene-Linked Ammonium Salts: The Search for Topochemical Anthracene Photodimerizations," *Tetrahedron*, vol. 56, pp. 6867–6875, sep 2000.

[300] W. N. Wang and W. Jones, "The Solid-State Chemistry of Acridizinium and 9-Methylacridizinium Salts," *Mol. Cryst. Liq. Cryst. Sci. Technol. A*, vol. 242, pp. 227–240, mar 1994.

[301] K. Morimoto, D. Kitagawa, F. Tong, K. Chalek, L. J. Mueller, C. J. Bardeen, and S. Kobatake, "Correlating Reaction Dynamics and Size Change during the Photomechanical Transformation of 9-Methylanthracene Single Crystals," *Angew. Chem. Int. Ed.*, vol. 61, no. 2, 2022.

[302] C. Yang, L. Zhu, R. A. Kudla, J. D. Hartman, R. O. Al-Kaysi, S. Monaco, B. Schatschneider, A. Magalhaes, G. J. O. Beran, C. J. Bardeen, and L. J. Mueller, "Crystal structure of the meta-stable intermediate in the photomechanical, crystal-to-crystal reaction of 9-tertbutyl anthracene ester," *CrystEngComm*, vol. 18, pp. 7319–7329, 2016.

[303] L. Zhu, F. Tong, C. Salinas, M. K. Al-Muhanna, F. S. Tham, D. Kisailus, R. O. Al-Kaysi, and C. J. Bardeen, "Improved Solid-State Photomechanical Materials by Fluorine Substitution of 9-Anthracene Carboxylic Acid," *Chem. Mater.*, vol. 26, pp. 6007–6015, oct 2014.

[304] L. Zhu, R. O. Al-Kaysi, and C. J. Bardeen, "Reversible Photoinduced Twisting of Molecular Crystal Microribbons," *J. Am. Chem. Soc.*, vol. 133, pp. 12569–12575, aug 2011.

[305] T. Salzillo and A. Brillante, "Commenting on the photoreactions of anthracene derivatives in the solid state," *CrystEngComm*, vol. 21, no. 20, pp. 3127–3136, 2019.

[306] T. Salzillo, I. Bilotti, R. G. Della Valle, E. Venuti, and A. Brillante, "Crystal-to-crystal photoinduced reaction of dinitroanthracene to anthraquinone," *J. Am. Chem. Soc.*, vol. 134, pp. 17671–17679, oct 2012.

[307] R. Moré, G. Busse, J. Hallmann, C. Paulmann, M. Scholz, and S. Techert, "Photodimerization of Crystalline 9-Anthracenecarboxylic Acid: A Nontopotactic Autocatalytic Transformation," *J. Phys. Chem. C*, vol. 114, pp. 4142–4148, mar 2010.

[308] M. Irie, T. Fukaminato, K. Matsuda, and S. Kobatake, "Photochromism of Diarylethene Molecules and Crystals: Memories, Switches, and Actuators," *Chem. Rev.*, vol. 114, pp. 12174–12277, dec 2014.

[309] O. Sato, "Dynamic molecular crystals with switchable physical properties," *Nature Chemistry*, vol. 8, pp. 644–656, jul 2016.

[310] S. R. Jezowski, L. Zhu, Y. Wang, A. P. Rice, G. W. Scott, C. J. Bardeen, and E. L. Chronister, "Pressure Catalyzed Bond Dissociation in an Anthracene Cyclophane Photodimer," *J. Am. Chem. Soc.*, vol. 134, pp. 7459–7466, may 2012.

Appendix A

Experimental and Computational Details for 9-methylanthracene Crystal Structure

Table A.1: Comparison of 0 K DFT-predicted lattice parameters computed with the B86bPBE-XDM functional against the experimentally-reported room-temperature crystal structures.

Structure	Source	Space group	a (Å)	b (Å)	c (Å)	α (°)	β (°)	γ (°)
9-methyl anthracene (9MA)								
Monomer	MANTHR15	$P2_1/c$	8.679	14.402	8.026	90	96.95	90
	DFT	$P2_1/c$	8.568	14.033	8.002	90	95.23	90
SGD	QQQFES04	$P2_1/c$	9.851	13.285	8.130	90	115.14	90
	DFT	$P2_1/c$	9.639	13.308	8.025	90	114.06	90
SSRD	QQQFES05[a]	$P2_1/c$	8.444	13.728	8.584	90	99.37	90
	QQQFES06[b]	$P2_1/c$	8.48	13.582	8.538	90	99.20	90
	DFT	$P2_1/c$	8.347	13.513	8.477	90	97.95	90
9-tert-butyl anthracene ester (9TBAE)								
Monomer	NUKMIP01	$P2_1/n$	9.168	17.265	9.503	90	99.50	90
	DFT[c]	$P2_1/n$	9.126	16.925	9.4084	90	100.21	90
SGD	ANODAJ[d]	$P\bar{1}$	9.161	9.692	10.218	67.19	85.40	62.23
	DFT[c]	$P\bar{1}$	9.116	9.555	10.237	64.95	82.88	60.89
SSRD	Ref 302	$Pccn$	15.871	12.065	15.759	90	90	90
	DFT	$P2_1/n$	9.671	15.683	9.744	90	106.01	90
PRD	Ref 273	$P2_1/n$	9.142	17.540	9.753	90	99.82	90
	DFT[c]	$P2_1/n$	9.630	15.691	9.810	90	105.76	90
9-anthracene carboxylic acid (9AC), Monoclinic								
Monomer	QQQFDJ01	$P2_1/n$	3.897	9.355	28.980	90	90.79	90
	DFT[c]	$P2_1/n$	3.751	9.242	28.525	90	90.89	90
SSRD	DFT	$P2_1/c$	7.582	9.591	29.565	90	102.70	90

[a] Structure determined at 0.1 GPa [b] Structure determined at 0.4 GPa

[c] DFT optimization started from experimental structure.

[d] Structure determined at 100 K.

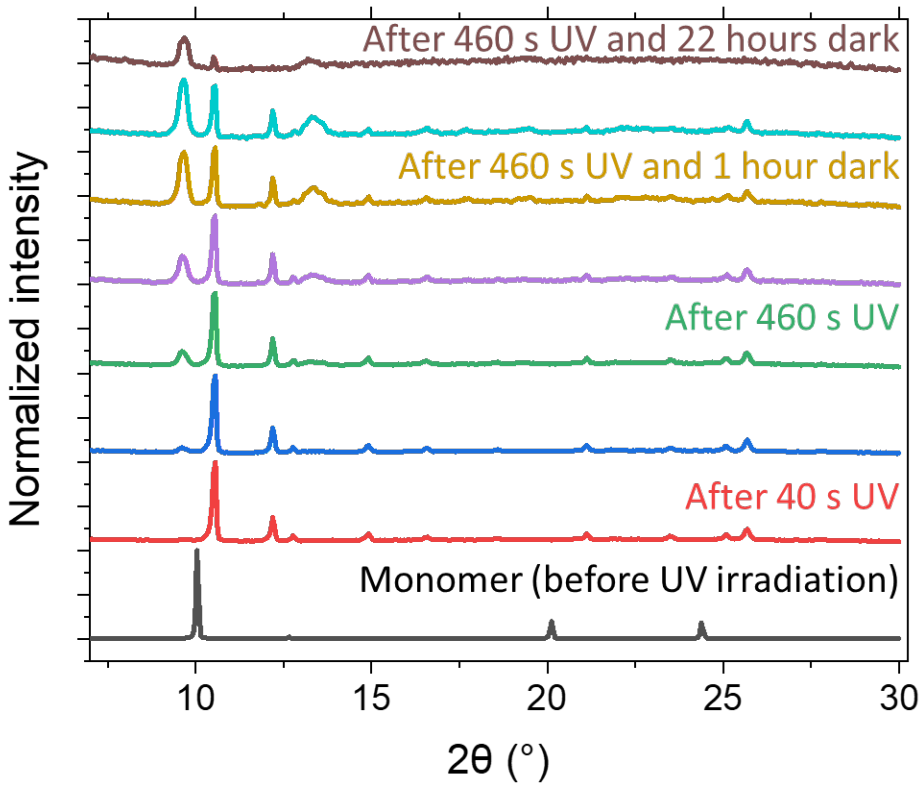

Figure A.1: Time evolution of PXRD 9MA crystals after UV irradiation. The initial monomer pattern is shown in black. After 40 s of 365 nm UV irradiation, the photodimer SSRD forms (red). The sample was further exposed to UV for an additional 420 s (green). Subsequent scans were taken of the sample while left in the dark and the SSRD peaks disappear, leaving only the amorphous phase after a period of 22 hours (brown). The very broad diffraction peaks at around 9.5° and 13° may reflect the presence of some SGD crystal that is formed at longer times.

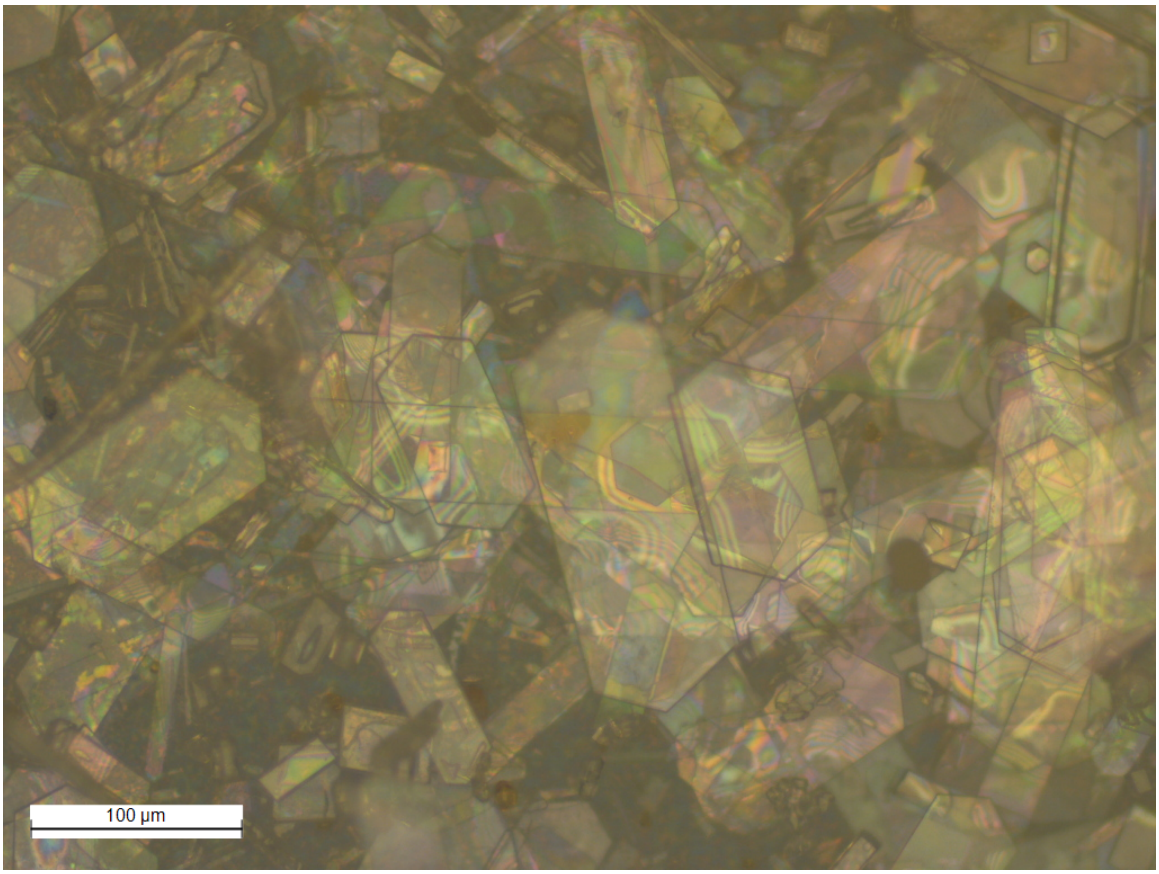

Figure A.2: Microscopy images of the as prepared filtered 9MA crystals. The predominant orientation of the crystals are lying flat and upwards, showcasing the hexagonal facets.

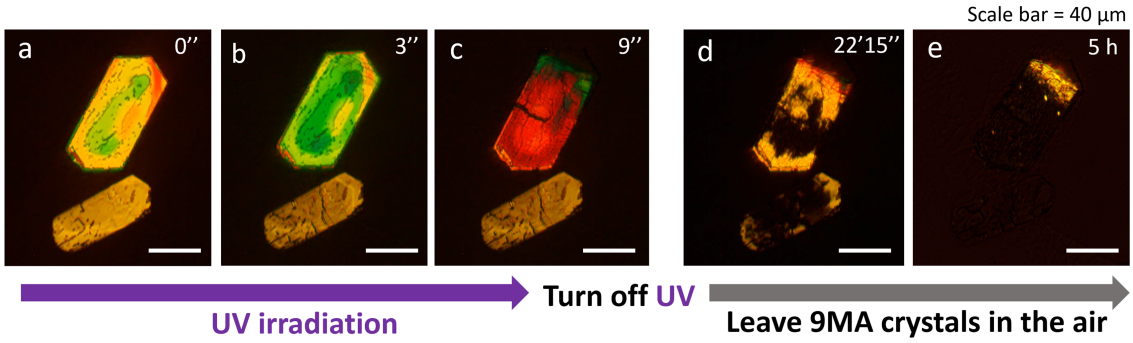

Figure A.3: Birefringence tracking of 9MA crystals during the a-c) photodimerization and d,e) amorphization in the air at room temperature. a-c) Over 9 minutes of 365 nm light exposure, the photodimerization process shifts the birefringence color of crystals. d-e) After turning off UV and leaving the crystals in the air for 5 hours, the 9MA photodimer crystals gradually lose crystallinity and turn amorphous as judged from the loss of birefringence.